Dual-Wavelength Scanning Near-Field Optical Microscopy

Philip R. LeBlanc

Center for the Physics of Materials
Department of Physics, McGill University
Montréal, Canada

A Thesis submitted to the
Faculty of Graduate Studies and Research
in partial fulfillment of the requirements for the degree of
Doctor of Philosophy

Your file Votre référence
ISBN: 0-612-88507-0
Our file Notre référence
ISBN: 0-612-88507-0

Table of Contents

Abstract

A dual-wavelength Scanning Near-Field Optical Microscope was developed in order to investigate near-field contrast mechanisms as well as biological samples in air. Using a helium-cadmium laser, light of wavelengths 442 and 325 nanometers is coupled into a single mode optical fiber. The end of the probe is tapered to a sub-wavelength aperture, typically 50 nanometers, and positioned in the near-field of the sample. Light from the aperture is transmitted through the sample and detected in a confocal arrangement by two photomultiplier tubes. The microscope has a lateral topographic resolution of 10 nanometers, a vertical resolution of 0.1 nanometer and an optical resolution of 30 nanometers. Two alternate methods of producing the fiber probes, heating and pulling, or acid etching, are compared and the metal coating layer defining the aperture is discussed. So-called "shear-force" interactions between the tip and sample are used as the feedback mechanism during raster scanning of the sample. An optical and topographic sample standard was developed to calibrate the microscope and extract the ultimate resolution of the instrument. The novel use of two wavelengths enables the authentication of true near-field images, as predicted by various models, as well as the identification of scanning artifacts and the deconvolution of often highly complicated relationships between the topographical and optical images. Most importantly, the use of two wavelengths provides information on the chemical composition of the sample. Areas of a polystyrene film are detected by a significant change in the relative transmission of the two wavelengths with a resolution of 30 nanometers. As a biological application, a preliminary investigation of the composition of Black Spruce wood cell fibers was performed. Comparisons of the two optical channels reveal the expected lignin distributions in the cell wall.

Résumé

Un microscope optique en champs proche qui opère à deux longueurs d'ondes a été developpé afin d'investiguer des échantillons biologiques. Un faisceau laser de longeur d'onde 442 et 325 nanomètres est couplé à une fibre optique mono-mode. Le bout de la fibre est effilé jusqu'à obtenir une sonde d'un trou source de diamètre typique de 50 nanomètres et est maintenu au champ proche de l'échantillon. La lumière qui s'échappe du trou source passe à travers de l'échantillon et est détectée par deux tubes photomultiplicateurs. Les deux méthodes pour effiler les fibres optiques (soit par attaque chimique, soit mécaniquement) sont comparées et la métallisation à l'aluminium est discutée. La sonde est collée à l'une des branches d'un diapason en quartz et est oscillée en parallele à la surface de l'échantillon. Les interactions atomiques (appelé "shear-force") entre la sonde et l'échantillon se manifestent sous forme de changement d'amplitude de l'oscillation. Ces interactions sont gardées constantes par rétroaction durant le balayage de l'échantillon. Un échantillon standard pour calibrer l'intrument a été développé et sert à determiner la résolution ultime du microscope: 10 nanomètres de résolution topographique latérale, 0.1 nanomètres de résolution verticale et 30 nanomètres de résolution optique. La comparaison des deux longueurs d'ondes permet l'identification d'artefacts dû au balayage et la déconvolution de la relation, parfois très compliquée, entre l'image topographique et l'image optique. Encore plus important, la présence de deux longueurs d'ondes peut identifier la composition chimique de l'échantillon. Comme application biologique, une investigation sur la composition de cellule d'épinette noir est présentée. Un changement relatif de la transmission aux deux longueurs d'ondes sert à identifier les diverses composantes chimiques.

Acknowledgements

I would like to thank a number of people without whom this work would not have been possible, nor my time at McGill as rewarding.

My parents, Denyse and Robert LeBlanc deserve all the credit. Their support has meant more to me than I can say. Their encouragement, as well as my brother's, Alex LeBlanc, has inspired me throughout. Barbara McLean has been my best reason to reach for this goal – I love you very much. This work is dedicated to my whole family.

A great deal of thanks goes to Peter Grütter who introduced me to this field and has guided me from the beginning. Thank you Peter for your wisdom, your support and your patience. My appreciation also goes to Zaven Altounian, Dik Harris, Robert Moore and the other professors in the Physics Department at McGill for their insight and counsel.

Through collaborations and assistance, Derek Gray, Shaune Hanley, Jean-François Rivol, Helen Campbell, Robert Gagnon, Michel Beauchamp, Saverio Biunno, Steve Godbout, Mario Della Neve, Steve Kecani, Michel Champagne, John Egyed, Eddie Del Campo, Leo Nikkinen and Frank Van Gils have been of immeasurable help as have Paula Domingues, Diane Koziol, Joanne Longo, Linda Corkum, and Cynthia MacDonald.

I have also learned a great deal in discussions with my colleagues. Mark Roseman, Yanzhang Liu, Minming Gu, Graham Cross, Andre Schirmeisen, Mike Godin, Xiaobin Zhu, Vincent Tabard-Cossa, Alex Wlasenko, Bret Ellman, Valentin Yakimov, Eric Dufresne, Kaifeng Liang, Benjamin Smith, Sun Yan, Ali Alousi, Peter Varfalvy and Yi-Ting Huang have been invaluable as have Paul Mercure and Juan Gallego.

Finally, I wish to thank my friends for their, well, friendship. Chris Roderick, Wendy Pollard, Rebecca Mann, Anne-Marie Bisang, Sarah Bass, Alex Marini and Judy-Anne Craig, Stéphane and Julie Legault, Parick Monast, Sean and Bonnie Punch, Lysa Wolley,

Denis Michaud and Réjean Ducharme have been fantastic. I wish them all the happiness they have brought me.

Statement of Originality

The author claims the following aspects of this work to be original contributions to the field of Scanning Near-Field Optical Microscopy.

- The design, construction and characterization of a transmission Scanning Near-Field Optical Microscope operating at 442 and 325 nanometers simultaneously. The modularity of the instrument enables a variety of scanning modes to be implemented and a range of samples to be analyzed. The instrument is the first of its kind to operate in the ultraviolet and the only one to acquire two wavelengths simultaneously.
- The design and construction of a physical vapor deposition evaporator designed specifically for rapid mounting and coating of SNOM probes. The chamber features an *in situ* fiber rotation stage, is capable of simultaneous or co-evaporation of two sources with a deposition rate of greater than 150 nanometers per second, and is equipped with two thermocouples and a heating stage. A fiber carousel was also designed to provide a single mount for etching, coating, storing and SEM evaluation of the fiber probes.
- A credible method of authenticating true near-field images by the presence of distinct contrast between the two wavelength channels. The distinct contrast is predicted in various near-field models. Proper authentication of images still remains a major challenge in the SNOM field, as often high optical resolution is a result of topographical cross-talk.
- A study of polystyrene islands where chemical contrast is revealed with a resolution of 30 nanometers.
- A study of Black Spruce wood cells exhibiting chemical contrast at the cell walls attributed to changes in the lignin concentration and contrast in the lumen region attributed to the embedding resin.

Chapter 1

Introduction

In 1590 Dutch spectacle-maker Zacharias Janssen built the first compound microscope and changed the way we look at the world forever. His device, perfected by Galileo in 1610, opened up an incredible new world where microscopic creatures lived and the mysteries of matter could be investigated. The properties of light have been exploited over the past four hundred years to produce such varied instruments of discovery as the Phase Contrast Microscope, the Confocal Microscope, the Fluorescence Microscope and others. While accomplished tools of science, these all suffer from the same shortcoming: they are all diffraction-limited.

The classical optical microscopy resolution limit, formulated by Abbe in 1873[1] has been an insurmountable hurdle, restricting features detectable by optical microscopy to about one-half the wavelength of light. Non-optical methods, such as electron microscopy and tunneling microscopy, have been invaluable in our understanding of the world on a smaller scale, but these suffer from their own limitations and can't benefit from the centuries of studies using light.

In 1928, as a series of discussions with Albert Einstein, Edward Synge proposed an optical microscope design that could overcome the Abbe barrier[2]. His remarkable instrument included a glass needle probe with a sub-wavelength aperture, evaporated coatings to confine the light field, piezoelectric motion control and raster-scanned images. Due to the limited instrumental techniques of his time, Synge's vision would have to wait for over fifty years.

With techniques developed for the Scanning Tunneling Microscope (STM)[3], Dieter Pohl *et al.* developed the Scanning Near-Field Optical Microscope (SNOM or NSOM)[4] in

1984 whose resolution goes well beyond the Abbe barrier. Present-day SNOM designs closely resemble Synge's original idea as hundreds of research groups throughout the world use SNOM's combination of optical characterization with nanometer spatial resolution to investigate a wide range of surfaces, see figure 1-1.

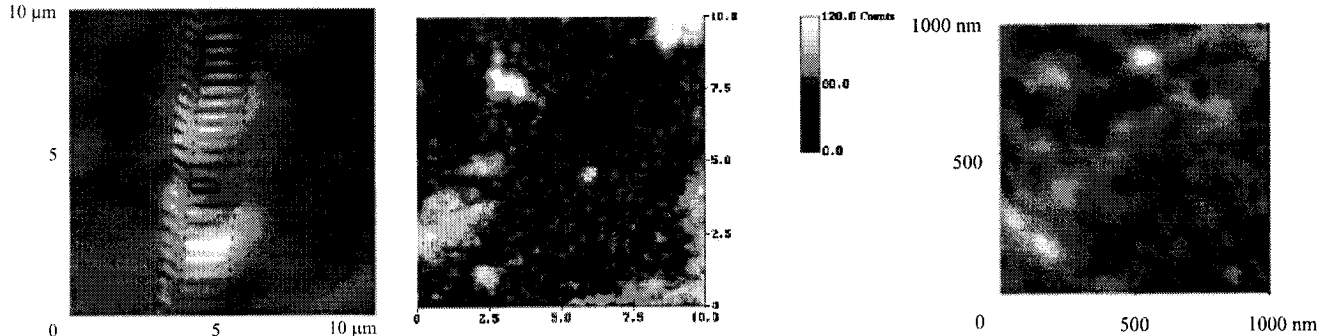

Figure 1-1. SNOM as a versatile surface science tool. (a) Collection SNOM image (λ=1.55μm) of the evanescent field above an InP/InGaAsP semiconductor waveguide. The limits of the guide are marked by dotted lines[5]. (b) Single-molecule fluorescence SNOM image of monolayer consisting of L-a-dipalmitoylphosphatidyl-choline (DPPC-σ) doped with $1x10^{-6}$ mol % fluorescent 1, 1'-dioctadecyl-3,3,3',3'-tetramethylindocarbocyanine perchlorate[6]. (c) Transmission SNOM image of percolation gold-glass film (λ=780nm)[7].

The versatility of SNOM techniques is impressive, however, applications have been challenging owing to the difficulties in understanding the acquired images. Notably, SNOM signals are significantly influenced not only by the optical parameters and structure of the sample, but also on the detection conditions. Some modeling work has been done in understanding how SNOM contrast depends on wavelength.

In standard SNOM, light of only one wavelength is used to image the sample surface. Although this technique has proved successful, it is lacking in two areas: the identification of scanning artifacts and the resolution of different chemical species in the sample. This work presents the development of a dual-wavelength SNOM, operating in the visible and the ultraviolet simultaneously, which provides complementary information to permit the proper interpretation of the optical and topographical data. The contrasting of the two wavelength channels provides an effective means of recognizing

scanning artifacts and of performing optical absorption spectroscopy on length scales previously unachievable.

Outline

This thesis is divided into three main sections.

In the first section, the fundamentals of near-field optics will be presented. An overview of the principles behind SNOM, current contrast models and the motivations for using two optical data channels will be explored.

The second section will deal with the design and characteristics of the SNOM. In particular the challenge of using two wavelengths simultaneously, of precise distance control, and of the manufacturing of the delicate sensor probes will be covered.

The final section will present the resolution and chemical contrast capabilities of the microscope as well as the challenges to proper image analysis. A study of wood cells is presented to demonstrate the potential of the instrument.

The objective of this thesis is to contribute to the field of Scanning Near-Field Optical Microscopy by demonstrating the promise of using complementary optical channels to provide a complete and accurate interpretation and analysis of surfaces on a sub-wavelength scale.

Chapter 2

Scanning Near-Field Optical Microscopy

2.1 Evanescent Waves and Optical Resolution

In the case of propagation in a vacuum ($\mu = \mu_0$, $\varepsilon = \varepsilon_0$ and $\sigma = 0$) or in a dielectric ($\sigma = 0$), Maxwell's equations describe plane harmonic waves

$$\mathbf{E} = \mathbf{E}_0 e^{i(\mathbf{k}\cdot\mathbf{r}-\omega t)} \quad \text{and} \quad \mathbf{H} = \mathbf{H}_0 e^{i(\mathbf{k}\cdot\mathbf{r}-\omega t)}$$

traveling in direction **k** with frequency ω and speed $v = 1/\sqrt{\mu\varepsilon}$. Consider such a wave incident upon an interface as in Figure 2-1.

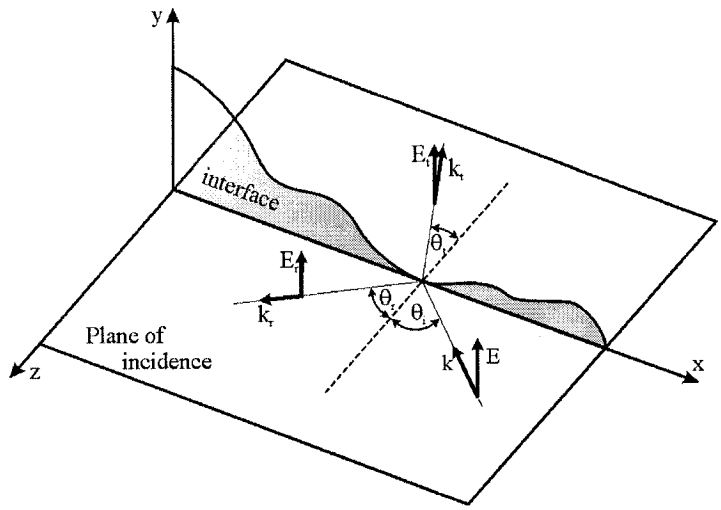

Figure 2-1. Linearly polarized electric field wave **E** incident upon an interface in the X-Y plane as a TE (transverse electric) mode. (Adapted from *Introduction to Optics*, by Pedrotti and Pedrotti, 2nd ed., Prentice Hall, 1993)

Let us examine the electric field (the magnetic field is completely analogous). The reflected and transmitted waves can be expressed as $\mathbf{E}_r = \mathbf{E}_{0r} e^{i(\mathbf{k}_r \cdot \mathbf{r} - \omega_r t)}$ and $\mathbf{E}_t = \mathbf{E}_{0t} e^{i(\mathbf{k}_t \cdot \mathbf{r} - \omega_t t)}$ respectively. Boundary conditions at the interface give us the law of reflection $(\theta = \theta_r)$ and Snell's law of refraction $(n \sin\theta = n_t \sin\theta_t)$. When $\cos\theta_t \equiv \sqrt{1 - \sin^2\theta_t} = \sqrt{1 - \frac{\sin^2\theta}{n^2}}$ becomes purely imaginary, for angles greater than the critical angle $(\sin\theta > n)$, total internal reflection (TIR) occurs. Writing $\cos\theta_t = i\sqrt{\frac{\sin^2\theta}{n^2} - 1}$, we obtain

$$\mathbf{k}_t \cdot \mathbf{r} = k_t(\sin\theta_t, \cos\theta_t, 0) \cdot (x, y, 0) = k_t x \frac{\sin\theta}{n} + i k_t y \sqrt{\frac{\sin^2\theta}{n^2} - 1}\,.$$

Defining the real, positive number $\alpha = k_t \sqrt{\frac{\sin^2\theta}{n^2}}$, the transmitted wave may be expressed as

$$\mathbf{E}_t = E_{0t} e^{-i\omega t} e^{i x k_t \sin\theta / n} e^{-\alpha y}. \tag{2.1}$$

This is an example of an *evanescent wave*, characterized by an exponentially decaying amplitude, $\mathbf{I}_t = (\mathbf{E}_t)^2 \propto e^{-2\alpha y}$. The number α is related to the *skin depth* by

$$\delta = \frac{1}{\alpha} = \frac{\lambda}{2\pi\sqrt{\frac{\sin^2\theta}{n^2} - 1}}. \tag{2.2}$$

A typical value of the skin depth in the visible spectrum is 10 nanometers, see (Figure 2-2). Whereas plane waves dominate in the Far-Field (FF), evanescent waves play a crucial role in Near-Field (NF) optics as the principal optical imaging mechanism. The term *near-field* used in this context refers to the region where the evanescent waves still contribute and should not be confused with the classical (Fresnel) near-field[8] which is at least a wavelength further away.

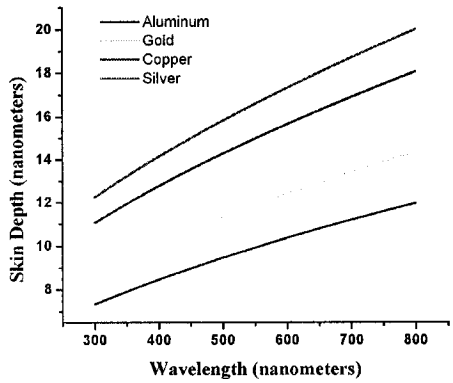

Figure 2-2. Skin depth of aluminum and other good conductors, for near-ultraviolet and visible spectrum calculated from $\delta = \sqrt{2/\mu\omega\sigma}$ (see, for example, *Classical Electrodynamics*, by J. D. Jackson, John Wiley & Sons, 2nd ed., 1975)

Far-Field effects, such as diffraction, play a dominant role in classical optical microscopy. Consider a light source placed behind a circular aperture of diameter *D*. The image observed a "large distance" away (at a spacing $Z > D^2/\lambda$, that is, much greater than both the aperture and the wavelength) is the familiar Bessel function diffraction pattern[9] (see Figure 2-3).

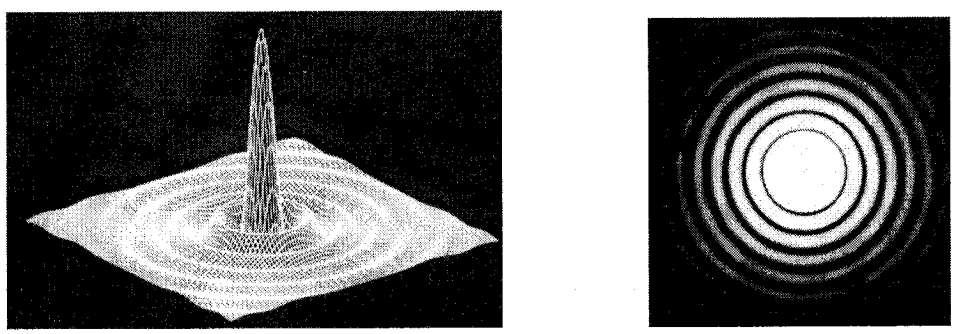

(a) (b)

Figure 2-3. (a) Electric field created by far-field, or Fraunhofer, diffraction by a circular aperture of diameter *D*. (b) Airy rings showing intensity distribution of diffraction pattern varying as $\left[\frac{2\,J_1(k\frac{D}{2}\sin\phi)}{k\frac{D}{2}\sin\phi}\right]^2$ where ϕ is the angle from the center of the aperture to a point on the pattern, k is the wave number and $J_1(\rho)$ is the Bessel function of the first kind. (From *Optics*, by E. Hecht, Addison Wesley, 2nd ed., 1987)

In regards to the ultimate resolution of a microscope, consider two such patterns placed close together. The Rayleigh criterion for *just-resolvable* images requires that the center of one pattern's Airy disk (the bright central disk) lie no closer than the first minimum of the second pattern. Under incoherent illumination, this corresponds to an angular separation of

$$\theta_{\min} = \frac{1.22\lambda}{D}. \tag{2.3}$$

If one considers a geometry where a lens is used instead of an aperture as above, the fundamental, diffraction-limited, resolution limit – the Abbe barrier – is found to be[10]

$$\Delta x_{\min} = \frac{1.22\lambda}{2n\sin\phi} \tag{2.4}$$

where n is the index of refraction of the medium between the object and the lens. This expression is often written in terms of the numerical aperture (*N.A.*) of the lens,

$$\Delta x_{\min} = \frac{0.61\lambda}{N.A.}. \tag{2.5}$$

Using Fourier optics[11], we may show that this is not a fundamental limit, rather it arises due to the imaging element (i.e. the lens) being many wavelengths away from the sample. High spatial frequency components decay rapidly with distance from the object and so in the far-field regime, only low-frequency components remain, limiting resolution. In classical optical microscopy, resolution even slightly beyond the wavelength of light is difficult to achieve and requires great effort. The limitation of the resolution to hundreds of nanometers was the driving force behind the move to the near-field and the development of SNOM.

Under a completely general formalism, we may express any two-dimensional electromagnetic field distribution, $\mathbf{E}(k_x, k_y, z) = \mathbf{E}_1 e^{ik_z z} + \mathbf{E}_2 e^{-ik_z z}$, as an infinite number of incoming and outgoing plane and evanescent waves. The evolution of the Fourier components, $\mathbf{E}_1$ and $\mathbf{E}_2$, determines the field distribution during propagation in the reference plane, z = constant. Using a suitable source (or detector), we may create (or probe) evanescent modes and are thus no longer limited by the constraints of propagating

(far-field) waves. The essence of Near-Field Microscopy is to create such sub-wavelength probes, forgo the effects of diffraction, and investigate high spatial frequency modes of the sample surface.

That resolution is limited to the dimensions of the detector may also be thought of in terms of signal processing[12]. Assume a sample consisting of cosinusoidally-varying features of spatial frequency α (that is, $g(x) = 1 + \cos(2\pi\alpha x)$). We may model the near-field probe as a rectangular detector of aperture d and response function S. Assume a relative motion between the detector and the sample with velocity v (this represents the scanning process and converts spatial frequencies to temporal ones, in particular, $f = \alpha v$) and the detector signal is given by[13]

$$h(t) = S\int_{-\infty}^{\infty} g(x)\,rect(\frac{x}{d})\,dx = S\int_{-d/2}^{d/2}[1+\mathrm{Re}\{e^{2\pi i}(ft-\alpha x)\}]\,dx = Sd + \frac{S}{\pi\alpha}\sin(\pi\alpha d)\cos(2\pi ft).$$

It is clear that to maximize the detector signal at high spatial frequencies, we must have $d = 1/2\alpha$ and that this represents the minimum detectable resolution. Note that this assumes the detector is close enough (that is, in the near-field) to the sample to probe the high spatial frequencies. The limiting resolution of a SNOM is then the greater of the sample features or the probe size, neither of which is restricted by considerations of wavelength (see figure 2-4 below).

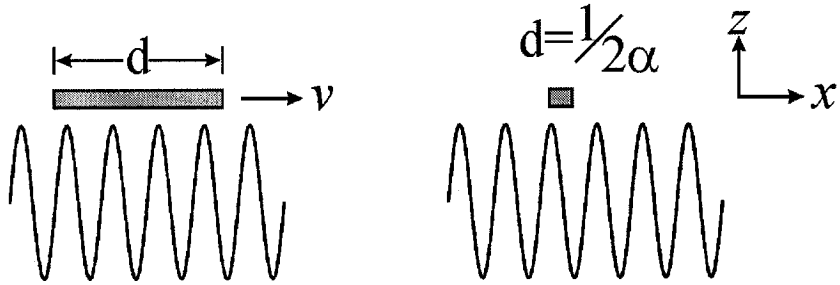

Figure 2-4. A rectangular detector of aperture d scans over the high frequency features $g(x) = 1 + \cos(2\pi\alpha x)$ of the sample at a velocity v. The minimum detectable resolution occurs for $d = 1/2\alpha$.

2.2 SNOM Modeling

Analytic approaches based on rigorous diffraction theory have so far focused on the ideal case where the aperture is modeled as a hole in a perfectly conducting infinite plane. Among these approaches, Bethe's theory provides useful insights for experiments[14]. The method associates the aperture with effective dipole moments and shows that its far-field radiation is identical to that of a radiating magnetic dipole located at the center of the aperture. When a p-polarized plane wave is incident on the aperture, an additional electric dipole is induced normal to the plane. If the aperture is sufficiently small, compared to both the wavelength of the incident plane wave, it can be approximated by its lowest order multipole moment.

Whereas far-field diffraction becomes simpler to treat as the size of the aperture decreases, near-field diffraction becomes more and more complicated due to the increasing dependence on the material properties of the aperture[15]. A combined Bethe/Boukamp model predicts the aperture transmission coefficient should scale as d^6, where d is the aperture diameter[16]. A *parabolic* sheet with a hole would more closely resemble an actual SNOM tip. Unfortunately, electromagnetic field modes are exceedingly difficult to solve for under complex boundary conditions. In fact, the parabolic-shaped aperture model for a SNOM tip cannot be solved analytically[17].

Numerical modeling efforts of SNOM optical contrast have concentrated on two approaches: theories based on matching boundary conditions and those based on scattering.

2.2.1 Matching Boundary Conditions

2.2.1.1 Diffracted Fields

Nearly all applications of near-field microscopy use CW laser light sources which restricts our description of electromagnetic fields to ones which depend harmonically with time. The response of matter to exciting electromagnetic fields may be summarized in the dielectric function $\varepsilon(\mathbf{r},\omega)$ as the macroscopic behavior of a large number of atoms. For visible light, this suggests it is physically meaningful to consider such an approach in a range of around 10 nanometers or larger[18]. We start with the totally reflected electromagnetic wave $\boldsymbol{E}_0(\mathbf{r},\omega)$ incident on a glass-air plane interface at $z = 0$. The field $\boldsymbol{E}_d(\mathbf{r},\omega)$ diffracted by features on the surface is expressed using the Rayleigh hypothesis (that field scattered from a rough boundary beyond the excursions of the roughness can be represented in the form of a superposition of plane outgoing waves) by assuming a plane wave expansion of the form,

$$\boldsymbol{E}_d(\mathbf{r},\omega) = \iint dk_x\, dk_y\, \boldsymbol{F}_d(\boldsymbol{k},\omega) e^{i\boldsymbol{k}\cdot\mathbf{r}} \tag{2.6}$$

where $\boldsymbol{k} = (k_x, k_y, k_z)$ represents the field diffracted by the surface, $k^2 = k_x^2 + k_y^2 + k_z^2 = \frac{\omega^2}{c^2}\varepsilon$ and $\boldsymbol{r} = (x, y, z)$. The diffracted field contains both radiative and evanescent waves, however, for a sample featuring sub-wavelength elements, the majority of components are evanescent. The resulting diffracted field is then confined around the surface corrugations.

The field amplitudes $\boldsymbol{F}_d(\boldsymbol{k},\omega)$ are difficult to evaluate. One must introduce the Fourier transform of the surface profile,

$$\Gamma(x,y) = \iint dk_x\, dk_y\, \gamma(k_x, k_y) e^{i(k_x x + k_y y)}. \tag{2.7}$$

The application boundary conditions at the surface leads to a complex relation between the incident and the diffracted fields. One solution is to work within a perturbative

approximation consisting of expanding the exponential term in (2.6) as a power series of $k_z\Gamma(x,y)$:

$$e^{i(k_x x+k_y y+k_z\Gamma(x,y))}=e^{i(k_x x+k_y y)}[1+ik_z\Gamma(x,y)+\cdots]. \tag{2.8}$$

In the limit of weak surface corrugations, this expansion may be limited to first order. The diffracted amplitudes are then proportional to $\gamma(k_x,k_y)$, the Fourier transform of the surface profile, and are linearly dependent on the zeroth-order field $\boldsymbol{E}_0(\mathbf{r},\omega)$:

$$\boldsymbol{F}_d(k_x,k_y,\omega)\approx i(\varepsilon'-\varepsilon)\gamma(k_x-q_x,k_y-q_y)A(k_x,k_y)\cdot\boldsymbol{E}_0(\mathbf{r},\omega) \tag{2.9}$$

where q_x and q_y are the incident wave vector and $A(k_x,k_y)=\frac{\omega^2/c^2}{k_z+k_z'}\mathbf{1}-\frac{1}{k_z'+\varepsilon' k_z}\begin{pmatrix}k_x^2 & k_xk_y & k_xk_z\\ k_yk_x & k_y^2 & k_yk_z\\ k_z'k_x & k_z'k_y & k_z'k_z\end{pmatrix}$ is a 3x3 transfer matrix. Here **1** is the identity matrix, k_z' is a z component of the wave vector diffracted inside the sample characterized by the dielectric function ε': $k_z'^2=\frac{\omega^2}{c^2}\varepsilon'-k_x^2-k_y^2$. The total optical field present at the surface features is then expressed as a correction to the result associated with a perfectly flat surface:

$$\mathbf{E}(\mathbf{r},\omega)\approx\mathbf{E}_0(\mathbf{r},\omega)+i(\varepsilon'-\varepsilon)\iint dk_x\,dk_y\,e^{i\mathbf{k}\cdot\mathbf{r}}\gamma(k_x-q_x,k_y-q_y)A(k_x,k_y)\cdot\boldsymbol{E}_0(\mathbf{r},\omega). \tag{2.10}$$

In this form, the field can be solved by using Fast Fourier Transform (FFT) algorithms. The accuracy of the result, as is typical when using FFTs, depends on the number of spatial harmonics considered.

The diffractive fields method enjoyed early success in modeling SNOM images as it exhibited polarization dependence observed in experiments[19]. However, the method's validity is limited to surfaces with corrugations varying weakly over the range of incident wavelengths.

2.2.1.2 Multipoles

Based on a formulation for antenna design at long wavelengths[20], Novotny *et al* developed a formalism where expansions of multipolar eigenfunctions are used as the basis in the study of near-field contrast. The eigenfunctions $\boldsymbol{F}_n(\boldsymbol{r},\omega)$ satisfy the vector wave equation for the eigenvalues q_n: $-\nabla\times\nabla\times\boldsymbol{F}_n(\boldsymbol{r},\omega)+q_n^2\boldsymbol{F}_n(\boldsymbol{r},\omega)=0$. We begin by constructing an electromagnetic field from the eigenfunctions $\Psi_n(\boldsymbol{r},\omega)$ of the scalar Helmholtz equation: $\nabla^2\Psi_n(\boldsymbol{r},\omega)+q_n^2\Psi_n(\boldsymbol{r},\omega)=0$.

Given that $\int\Psi_v^*(\boldsymbol{r},\omega)\Psi_{n'}(\boldsymbol{r},\omega)d\boldsymbol{r}=\delta_{n,n'}$, these eigenfunctions form an orthogonal basis set in Hilbert space. Three families of eigenfunctions can be generated by applying the following operators to the scalar function:

$$\boldsymbol{L}_n(\boldsymbol{r},\omega)=C\nabla\Psi_n(\boldsymbol{r},\omega),$$

$$\boldsymbol{M}_n(\boldsymbol{r},\omega)=C\nabla\times\Psi_n(\boldsymbol{r},\omega)\boldsymbol{a}, \text{ and}$$

$$\boldsymbol{N}_n(\boldsymbol{r},\omega)=\frac{C}{k}\nabla\times\nabla\times\Psi_n(\boldsymbol{r},\omega)\boldsymbol{a}$$

where C is a normalization factor (which depends on the coordinate system) and $\boldsymbol{a}$, is a constant vector of unit length called the "piloting vector". Due to the properties of the piloting vector and the orthonormalization of the scalar eigenfunctions, the three families are mutually orthogonal and are sufficient to form the completeness relationship:

$$\sum_n\left[\boldsymbol{L}_n(\boldsymbol{r},\omega)\boldsymbol{L}_n^*(\boldsymbol{r}',\omega)+\boldsymbol{M}_n(\boldsymbol{r},\omega)\boldsymbol{M}_n^*(\boldsymbol{r}',\omega)+\boldsymbol{N}_n(\boldsymbol{r},\omega)\boldsymbol{N}_n^*(\boldsymbol{r}',\omega)\right]=\mathbf{1}\delta(\boldsymbol{r}-\boldsymbol{r}'). \quad (2.11)$$

The first set of families, $\boldsymbol{L}_n(\boldsymbol{r},\omega)$, are physical solutions of the wave equation only if $k=\varepsilon=0$, arising at longitudinal optical frequencies in polar materials or at the plasma frequency in metals. We may therefore partition the space into subdomains, α, where the index of refraction is constant, into which we expand the electric field on the sets of transverse eigenfunctions $\boldsymbol{M}_n(\boldsymbol{r},\omega)$ and $\boldsymbol{N}_n(\boldsymbol{r},\omega)$:

$$E^{\alpha}(r,\omega)=\sum_{n}\left[a_n^{\alpha}M_n(r,\omega)+b_n^{\alpha}N_n(r,\omega)\right]. \tag{2.12}$$

In practice, the expansion is performed using multiple origins r_j, in order to account for poor convergence of the series. The multipole expansion is then expressed as:

$$E^{\alpha}(r,\omega)=\sum_{j}\sum_{n}\left[a_{n,j}^{\alpha}M_n(r-r_j,\omega)+b_{n,j}^{\alpha}N_n(r-r_j,\omega)\right]. \tag{2.13}$$

The coefficients are determined by matching boundary conditions between the subdomains. Due to the multiple subdomains and origins r_j, the completeness and orthonormalization conditions are no longer satisfied. Instead, semi-empirical rules are used to set the spacing of the origins.

The multipole expansion exhibits short range interactions, only over close subdomains, which makes this technique more suitable to real surface features than a plane wave expansion. Waveguide structures, such as the SNOM tip itself, have been modeled with some success using numerical simulations based on multipole expansions[21].

2.2.2 Scattering Theory

The approach of scattering theory is to present a completely general analytical solution to the inhomogeneous wave equation characterized by using a Green's function as the kernel. The challenge of using such a method in Near-Field Optics, where the result in the source region itself is desired, is that the Green dyadic turns up to be divergent in the source region. This behavior has been related to depolarization effects and an explicit renormalization procedure has been developed[22,23].

The complete Green dyadic method expansion is covered fully elsewhere[24-26]. An abbreviated derivation outlining the main result is presented here. We begin with the vector wave expression

$$-\nabla\times\nabla\times\boldsymbol{E}(\boldsymbol{r},\omega)+q^2\boldsymbol{E}(\boldsymbol{r},\omega)=\boldsymbol{V}(\boldsymbol{r},\omega)\boldsymbol{E}(\boldsymbol{r},\omega) \text{ where } q^2=\frac{\omega^2}{c^2}\varepsilon_{ref}. \quad (2.14)$$

Considerations for the anisotropy of the system are bundled into a departure from the reference system ε_{ref}:

$$\boldsymbol{V}(\boldsymbol{r},\omega)=\frac{\omega^2}{c^2}\left(1\varepsilon_{ref}-\varepsilon(\boldsymbol{r},\omega)\right) \quad (2.15)$$

The solution to the wave equation above may be derived from the implicit Lippmann-Schwinger equation,

$$\boldsymbol{E}(\boldsymbol{r},\omega)=\boldsymbol{E}_0(\boldsymbol{r},\omega)+\int_D d\boldsymbol{r}'\boldsymbol{G}(\boldsymbol{r},\boldsymbol{r}',\omega)\boldsymbol{V}(\boldsymbol{r}',\omega)\boldsymbol{E}(\boldsymbol{r}',\omega) \quad (2.16)$$

as the combination of an incident field plus a scattering term. The source region D is taken relative to the reference system. The solution is based on evaluating the analytical solution for the incident field: $-\nabla\times\nabla\times\boldsymbol{E}_0(\boldsymbol{r},\omega)+q^2\boldsymbol{E}_0(\boldsymbol{r},\omega)=0$ and the Green dyadic given by $-\nabla\times\nabla\times\boldsymbol{G}_0(\boldsymbol{r},\boldsymbol{r}',\omega)+q^2\boldsymbol{G}_0(\boldsymbol{r},\boldsymbol{r}',\omega)=1\delta(\boldsymbol{r}-\boldsymbol{r}')$. In cartesian coordinates we obtain a solution[27] of the form

$$\boldsymbol{G}_0(\boldsymbol{r},\boldsymbol{r}',\omega)=\int d\boldsymbol{k}\left[1-\frac{1}{q^2}\boldsymbol{kk}\right]\frac{e^{i\boldsymbol{k}\cdot(\boldsymbol{r}-\boldsymbol{r}')}}{8\pi^3(q^2-k^2)}=\left[1-\frac{1}{q^2}\nabla\nabla\right]g(\boldsymbol{r},\boldsymbol{r}',\omega) \quad (2.17)$$

where $g(\boldsymbol{r},\boldsymbol{r}',\omega)=\frac{e^{iq(|\boldsymbol{r}-\boldsymbol{r}'|)}}{4\pi|\boldsymbol{r}-\boldsymbol{r}'|}$ is the Green function associated with the scalar Helmholtz equation and given by a spherical wave emitted at $\boldsymbol{r}'$.

While none of these modeling methods have been able to quantitatively explain the full range of contrast mechanisms demonstrated in SNOM experiments, they do yield some insight into the complex interactions between the tip and the surface. Given the nature of the field's dependence on the wave vector (equations 2.10 and 2.17) and the wave frequency (equation 2.13), we note that though not *limited* by the wavelength of light, the optical contrast in the near-field is nevertheless *dependent* on the frequency of the electromagnetic field. The different optical contrasts observed at two separate wavelengths is part of the focus of this experimental work. We note also that

electromagnetic interactions between the probe tip and the sample are a function of the probe aperture shape, the local dielectric function, and the polarization state of the incident light.

The theory behind SNOM contrast is much more intricate than simple evanescent waves; the interactions outlined in this section involve complicated boundary value problems in three dimensions. In many cases, the SNOM images are convolutions of several different processes which are themselves highly sensitive. Furthermore, since the probes are not perfectly identical, image contrast is likely to vary between experiments. More sophisticated models and experiments are needed to better understand the contrast and consequently the potential of SNOM techniques. For example, numerical calculations[28,29] and experiments[29-31] show a sensitive dependence on the polarization states of near-field signals. Feature size[32], tip-sample distance[30,33], and aperture shape[34] also contribute strongly to resolution and contrast in SNOM. As an example of these effects, consider the simulation in figure 2-5.

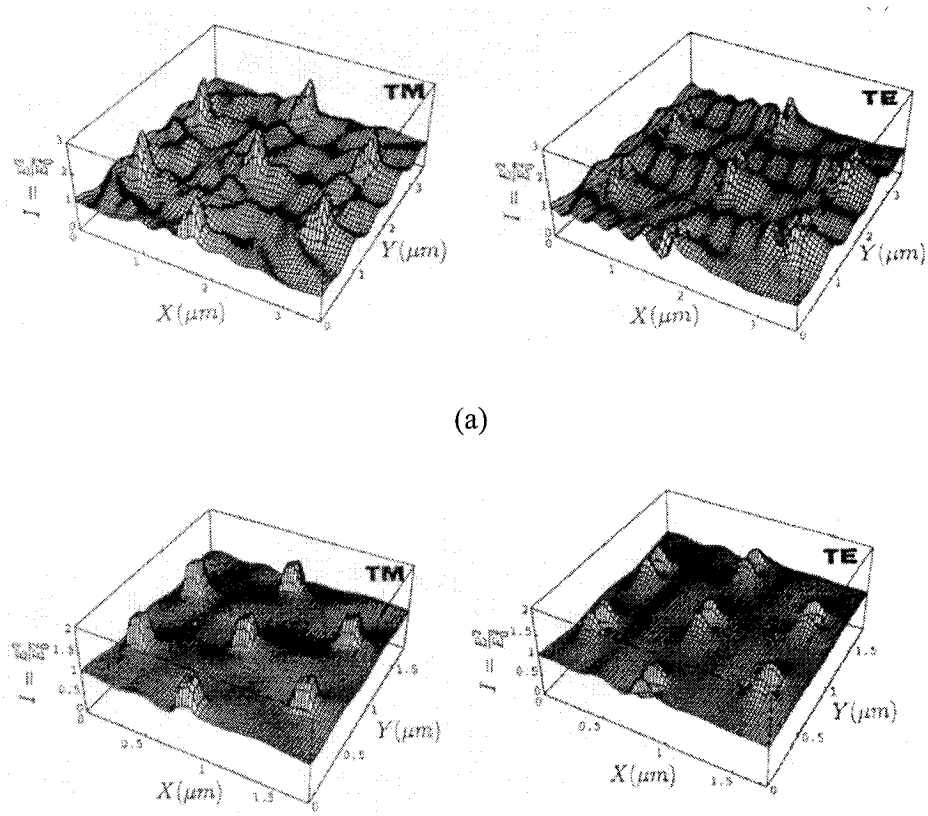

(a)

(b)

Figure 2-5. Numerical simulation of intensity, $I = |E|^2 / |E_0|^2$, around a pattern of 7 square glass islands on a glass substrate. The islands are located on the corners of a regular hexagon, plus the one in the center. Illumination is due to 620 nm light coupled to a SNOM probe located above the sample and positioned over each grid point. In (a), the islands are 250 nm on a side, 100 nm tall, the sides of the hexagon are 1,750 nm and the tip has an aperture of 135 nm which is also the tip's height above the sample. In (b), all dimensions have been reduced by a factor of 2. (From reference 28).

Here, the contrast varies considerably given the different polarization modes as well as sample and tip dimensions. In fact, on some samples it is possible for the contrast to be completely reversed between the different polarization modes[35-37]. It is also evident that the concept of feature resolution must be reconsidered in the near-field – we will revisit this in section 4.1.2. In the end, we must resort to an operational definition of resolution for SNOM images until sufficiently sophisticated near-field models reproduce

experimental results. It is of value to note that conventional optical microscopy also uses an operational definition for resolution in the Rayleigh Criterion.

2.3 General Setup

The microscope designed and built for this work is an aperture type transmission-illumination mode SNOM. Here, a quasi point-like source of light is brought into the near-field of a thin sample. The light is then collected using a lens after propagating through the sample. The remainder of the thesis will focus on this setup, though the operation of other types of SNOMs is very similar. The basic components of a transmission mode SNOM are shown in Figure 2-6.

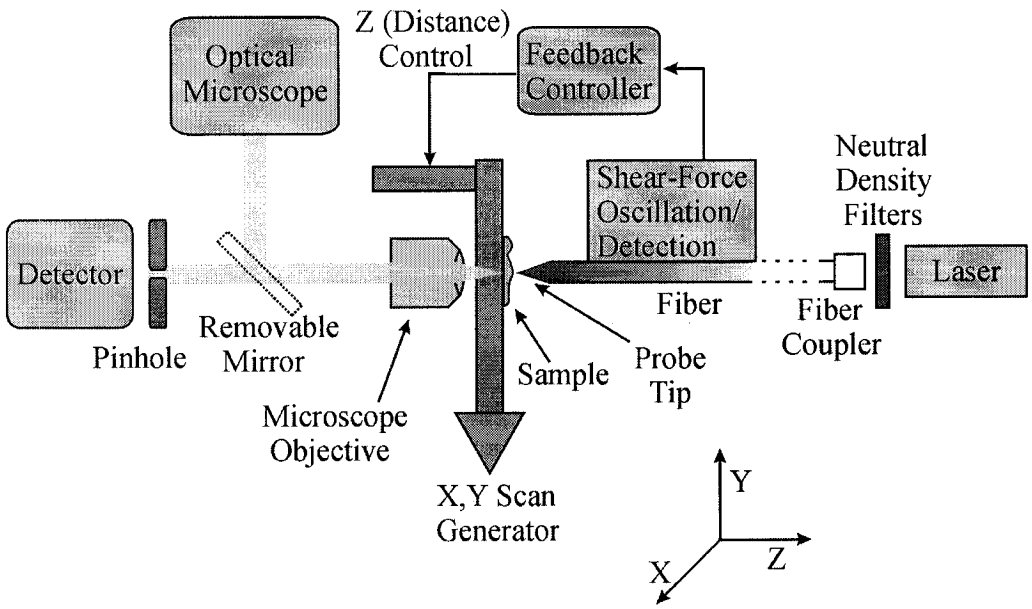

Figure 2-6. Transmission mode SNOM schematic.

SNOM shares much of its design with other Scanning Probe Microscopy (SPM) members, such as the Atomic Force Microscope (AFM) and the Scanning Tunneling Microscope (STM). The fiber tip is scanned over the sample while monitoring its interaction with the surface. By keeping this interaction constant (most SNOMs monitor the "shear-force"[38,39] between the tip and the sample – see section 2.6) one attempts to

maintain a constant tip-sample distance. Laser light is coupled into the free end of the optical fiber after being attenuated by neutral density filters. Light emanating from the tip passes through the sample and is focused by a microscope objective through a small pinhole and onto a sensitive detector. Images are created by raster scanning in X and Y, maintaining a constant shear-force and acquiring the intensity of transmitted light. A computer records the Z-position of the sample and the transmitted light intensity as a function of position to generate the topography and optical images respectively. A removable mirror and an optical microscope are frequently used to align the optics before scanning begins.

2.4 Fiber Optics and the Fiber Probe

The crucial part in every SPM is the tip. In Scanning Near-Field Optical Microscopy, this is no different. Optical fibers play the central role in defining the scanning probe. Fibers are tapered to a fine point at one end, forming the tip and used to guide light in order to form the optical image. A typical optical fiber used in SNOM is made up of a 4-5 micron diameter glass *core* (of index of refraction n_1 – typically around 1.490) surrounded by a 125 micron diameter glass or plastic *cladding* (of index of refraction n_2 – typically around 1.485). The differences in index of refraction is due to the presence of dopants, primarily GeO_2, in the core. The fiber is then encased in a 250 micron diameter plastic *jacket*. Light propagates down the fiber by total internal reflection but certain rays entering the fiber interfere destructively upon the many reflections. Only certain ray directions, or *modes*, may propagate constructively down the fiber. The number of such modes is given by[40]

$$m = \frac{1}{2.44}\left(\frac{\pi d}{\lambda} N.A.\right) \tag{2.6}$$

where d is the diameter of the core and $N.A. = \sqrt{n_1^2 - n_2^2}$. In *single-mode* fibers, small diameter cores succeed in letting only the axial mode propagate. This is the preferred type of fiber for SNOM probes. As the probe diameter lessens towards the aperture, even

the axial mode can no longer propagate constructively down the fiber. At this point, at a fiber diameter of about 160 nanometers[41], the light intensity begins to decay exponentially and only an evanescent wave remains to escape from the probe's narrow aperture.

The transmission coefficient, the ratio of the fiber output power to the input power, is an important characteristic of the fiber probes. Too small a ratio and noise may swamp the signal, however, a large ratio usually signifies a damaged or enlarged aperture and an accompanying loss in resolution. Since transmission intensity from the probe depends so strongly on aperture size, exceptionally small apertures (below 50 nanometers) generate small signal-to-noise ratios and so are difficult to use. Coupling more light into the fiber is not an option since probe tips' small heat capacity (due to their small volume) and low thermal conductivity causes them to tend to melt at high incident powers. Most SNOM studies use 80-100 nanometer diameter probes as a trade-off between resolution and signal strength[42].

Creating SNOM probes is a delicate technique involving two steps. First, the fiber taper is created. A short, large angle taper is desired to cut down on transmission losses and to improve mechanical stability at the tip. In the second step the tips are coated with aluminum in order to properly define the light source at the apex and thus create the aperture. This coating absorbs light that would otherwise leak out of the fiber taper, negating our efforts to create a small light aperture. A smooth, even coating is desired to reduce imaging artifacts such as those due to pinholes (see section 5).

The fiber probe is tapered using one of two methods: heating and pulling, or acid etching. The tip geometry is crucial since it determines the lateral resolution of the SNOM probe as well as its transmission efficiency and mechanical properties. The first widely-used method for creating narrow apertures was adopted from the physiologist's process of creating micropipettes. In fact, many SNOM groups use the same instrument as the physiologist's, the Sutter Instrument Company pipette puller. The procedure is simple, easy to setup and reasonably effective[43]. It involves heating a small spot of an optical

fiber while it is held under tension. As the fiber is heated, it becomes viscous and is drawn out (much like hot cheese on a pizza) forming a narrow neck and ultimately separating into two tapered tips with small apertures. Once separated, the fiber is cooled rapidly until viscous flow is negligible.

The formation of the apex radius is a result of two competing phenomena: the narrowing of the fiber due to the applied tension, and the intrinsic tendency of the fiber to divide into several pieces with smaller total surface area, due to the surface tension. Considering only the fiber thinning, one would expect[44] a radius that smoothly decays with time according to $r = r_0 \exp\left[-t/\tau_t\right]$ where the time constant, $\tau_t = \upsilon/T$ is the viscosity over the tension. Similarly[45], we may derive a time constant for the capillary instability caused by surface tension σ, $\tau_c = (\upsilon/\sigma)\, r$. As long as the tension remains below the glass fracture limit, the fiber continues thinning to a radius where both characteristic times meet. For a glass surface energy of 1 J/m and a brittle rupture limit of 1 GPa, one obtains a radius of 1 nanometer. This is considerably smaller than what is achieved experimentally, indicating increased instability, predominantly due to fluctuations in local heating and cooling rates, under practical pulling conditions. Generally, one may minimize the apex radius by applying large heating powers (to lower surface tension) and sizeable pulling tensions until fiber rupture occurs, then quickly cooling the fiber to prevent distortions due to viscous flow[46].

Fiber pulling has a number of advantages. The melting process produces very smooth taper surfaces which are well suited for subsequent coating. The heating power and tension force can be controlled to produce a flat facet at the apex which improves the formation of well-defined apertures. Finally, the pipette puller is fast and easy to use. Of course, there are some disadvantages as well. Only a single tip can be formed at a time (usually just one of the two tapers is good enough for SNOM use). The pipette puller has five independent control settings (heating power, pulling strength, pull delay setting, cooling power and cooling time) which makes finding the right parameters in phase space

rather daunting. The aspect ratio of the taper tends to be quite high resulting in a long, narrow probe which has a small spring constant, a low transmission coefficient, and is quite fragile.

For this work, we used 3M fiber model number FS-SN-3224 which has a single mode operating wavelength of 630nm and a cutoff wavelength of 620nm. It is a single mode fiber with a core diameter of 3.3 microns, a cladding diameter of 125 microns and an acrylate jacket diameter of 250 microns. Typical attenuation at the operating wavelength is 10 dB/km (about 0.12% loss of intensity per meter) and the numerical aperture of the fiber is 0.12. Although the operating wavelength is far from the two wavelengths used in the SNOM, this fiber was chosen for a number of reasons (size, availability, cost). Few single mode fibers are available, especially within a university-size budget, for transmission in the ultraviolet and these generally have jacket diameters of 125 microns which are incompatible with our fiber coupler. Of course, transmission losses are a concern. Up to 80% of the optical intensity losses present in our system occur at the fiber coupler. Efficient coupling is exceptionally sensitive to the proper alignment of the fiber face to the focused beam along 5 axes. Also, a perfectly flat fiber cleave is difficult to achieve (we use an inexpensive manual cleaver from Siecor, model number FBC-001). The transmission losses are negligible over the 1 meter length of fiber. We measured a loss of 75 dB/km (0.86% loss per meter) at 442nm and 140 dB/km (1.60% loss per meter) at 325 nm. All this, together with the propagation losses due to the fiber probe taper and the absorption due to the aluminum coating, means that typically only a few picowatts of the laser's original intensity is available at the apex.

Considerable work was done to optimize the fiber probe design. The simplest method to obtain a tapered fiber was the heating and pulling method. Pulled tips were created using a micropipette puller (Sutter Instruments Co. model number P-87). The puller is fully customizable; the user may control the filament current, the pulling strength, the fiber velocity at which the pull is applied, and the duration and pressure of the jet of air applied to cool the fiber once pulling is complete. The fiber profile is most sensitive to the heating filament current and pulling strength so this narrows the parameter space

considerably. The heating filaments used were created by hand from Platinum-Iridium wire (Goodfellow 80% Pt, 20% Ir 0.25 millimeter diameter wire).

Pulled fibers are characterized by two separate taper regions (see figure 2-7). This "S"-like profile is detrimental to both the mechanical stability of the fiber tip and to the light transmission properties of the probe. The long primary taper region is weak under lateral oscillation of the fiber during shear-force feedback mode and results in a small heat capacity and poor thermal conductivity. Also, the long taper region means that the fiber diameter where propagating modes are no longer supported occurs far away from the apex of the tip, resulting in significantly decreased light intensity emerging from the aperture. This loss in intensity cannot be compensated for by an increase in input power since the mechanical characteristics result in tips that melt easily under such power.

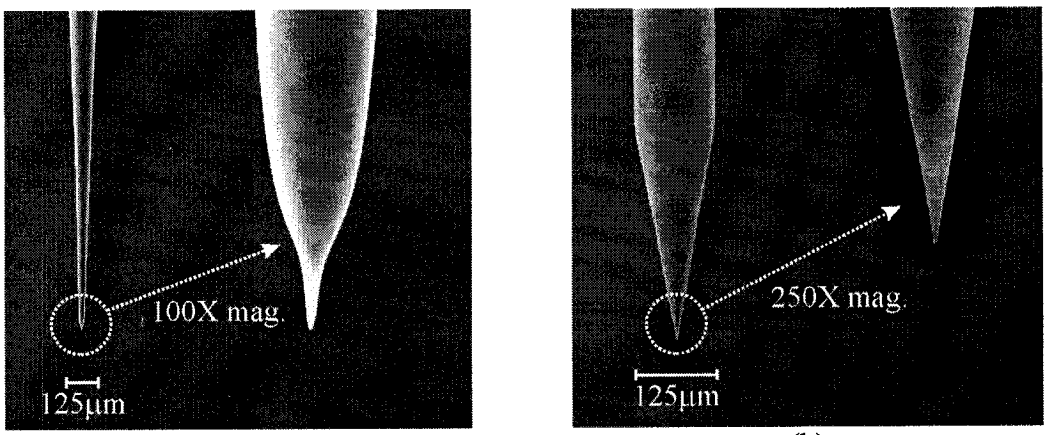

(a) (b)

Figure 2-7. (a), (b) SEM images of pulled and etched tip, respectively. Notice the long taper length and narrow necking in the pulled probes which results in lower optical transmission ratios. Note that (b) exhibits greater magnification and greater zoom.

The drawbacks of fiber pulling (poor reproducibility, long taper lengths, serial fabrication) were the motivations to move to a more effective method for producing SNOM probes – fiber etching.

Acid etching of fiber probes requires more care (since it uses a dangerous acid) but produces higher quality tips than fiber pulling. The fibers are lowered into a 40%

hydrofluoric acid solution* covered by a layer of organic buffer[47,48]. The interface between the acid and the organic overlayer creates controllably large taper angles as well as small apertures (see Figure 2-8). Tapers are short (a few hundred microns) and straight compared to the pulled probes. By varying the acid concentration, etching temperature and type of buffer, the taper can be shaped to some extent.

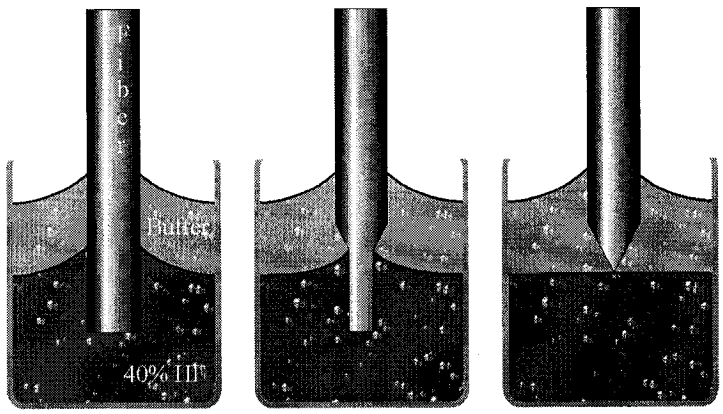

Figure 2-8. The fiber etching procedure is self-terminating.

Dynamic etching, where the fiber is moved into, or out of, the solution by a few μm/sec during etching can also be used to tailor probe shapes[49]. Extreme geometries, such as sub-micron taper lengths, can be created by mixing the acid with ammonium fluoride[50,51] and by multi-step etching procedures[52] but these are highly dependent upon fiber doping profiles[50,53]. The exceptionally short taper lengths can also cause scanning problems due to the cladding striking the sample, so they are not used extensively. Arrays consisting of a few to a few thousand individual imaging tips on a single optical fiber have been developed[54] but consistent tip shapes and throughputs across each tip in the array are difficult to achieve which has made optical image analysis too complex for wide use.

For conventional SNOM probes, acid etching is a batch procedure where many fibers can be shaped in a single stage, each having very similar characteristics. Other advantages include the production of short tapers and low aspect ratios so these fibers have exceptional vibration and optical transmission characteristics. Unfortunately, their high

* Use hydrofluoric acid with extreme caution. Any suspected contact must be immediately reported to paramedic personnel. Always keep a fresh tube of antidote (calcium glutonate gel) on site.

sensitivity to the etching environment (temperature changes, vibrations, fiber drifting, etc.) can result in taper surfaces with considerable roughness and non-symmetric apexes. This frequently causes coating pinholes and ill-defined apertures. Theoretical models of tip formation are emerging[55] but have yet to exhibit all properties of actual fiber probes.

Our initial fiber etching tests were done using 100 mL of a 40% HF solution in a petri dish[†] covered by about 50 mL of 1-octanethiol. The fibers were stripped of their protective jackets by first softening the plastic covering in dichloromethane for 15 seconds and then gently pulling the jacket off. The bare fibers were immersed in the solution for 45 minutes then tenderly removed and rinsed using ethanol.

This method was much more successful than by heating and pulling, but the fiber taper length and angle still varied slightly between batches and the taper region itself was usually slightly rough – a feature not present in the pulled probes. By carefully observing the etching through a microscope, we noticed two factors that needed to be resolved in order to produce better fiber tips. First there were vibrations in the fume hood where the etching was done, caused by fan noise and air currents. Second, the buffer level varied slightly during the procedure due to its gradual evaporation. Both effects resulted in ripples of the meniscus height of the interface between the acid and the organic buffer solution which created the observed taper roughness. Irregularities of this sort on the fiber taper can lead to pinholes in the metal coating and so improvements to the etching procedure were necessary.

The first step was to build a vibration isolation stage for the fiber etching. The etching stage consists of a 37.5 kg circular steel plate with a 2 mm depression in the center which fits the petri dish and prevents it from being accidentally knocked over. An aluminum arm overhangs above the petri dish and is fitted with a one dimensional translation stage. The spool carousel housing the fibers (see figure 2-9) is mounted onto the translational stage and can be positioned using a fine micrometer screw.

[†] We used PMP (polymethylpentene) petri dishes which resist corrosion by hydrofluoric acid.

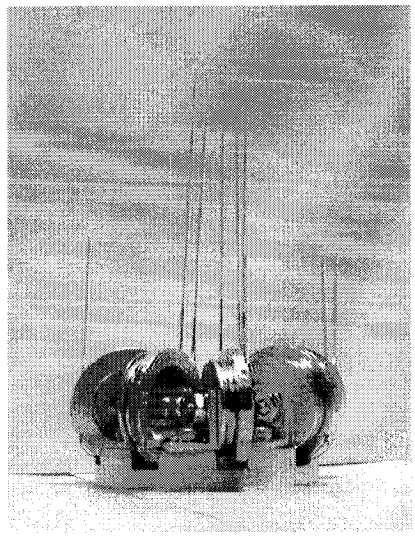

Figure 2-9. Spool carousel for batch etching and evaporation of fiber probes. Each spool (five are mounted here) is 3 cm in diameter.

The steel plate rests on a partially inflated rubber inner tube providing effective vibration damping (see figure 2-10a).

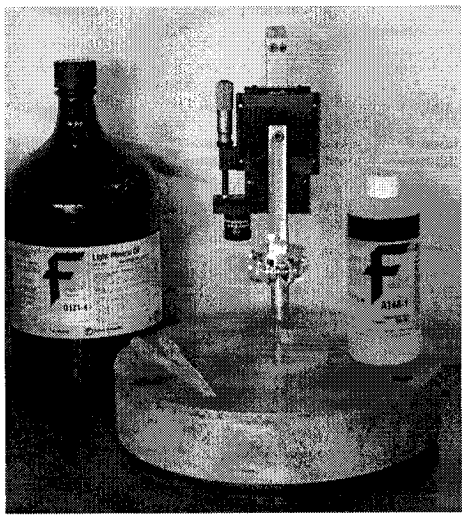

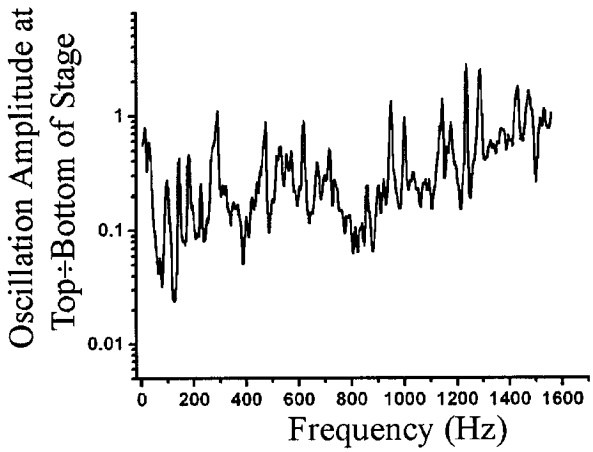

(a) (b)

Figure 2-10. (a) Vibration isolation stage for fiber etching process. (b) Transfer function for vibration isolation of etching stage.

The entire stage is placed in a fume hood and surrounded by an aluminum sheet, preventing air currents inside the fume hood from causing ripples in the etchant (see figure 2-10b).

Based on results from Lambelet *et al.*[56] and Stöckle *et al.*[57], we developed an improved etching procedure where the plastic jacket is actually left on the fiber during the etching process. The optimized procedure is described below.

A 1.15 meter length of optical fiber is wound onto the aluminum coating spool, about 6 cm of which extends past the needle tubing. Ethanol is used to clean the protruding length before the spool is mounted onto the etching stage. Using the proper safety equipment, the 40% HF solution is deposited into the petri dish and then covered with a thin layer of paraffin oil. The fiber is then lowered until it touches the bottom of the petri dish and then raised by 1-2 mm where it is etched for 60 minutes. This is done at room temperature.

The acid slowly diffuses through the jacket and gradually etches the fiber, forming a sharp apex. The paraffin oil (mineral oil may also be used) does not diffuse through the fiber jacket, and so the taper shape is governed solely by the etching of the glass by the acid. The oil acts merely to stop the evaporation of the acid which would alter the interface level and adversely effect tip shape. A much less reproducible effect occurs when using an organic buffer since the acid not only etches the glass fiber, but also slowly attacks the organic solution. The process is not exactly self-terminating and tip shapes vary greatly according to the choice of organic buffer[48]. Fibers etched using the oil buffer procedure are found to have much smoother tapers than those etched using an organic buffer (see figure 2-11). This improved shape leads to a better aluminum coating and fewer pinholes (see section 2.5).

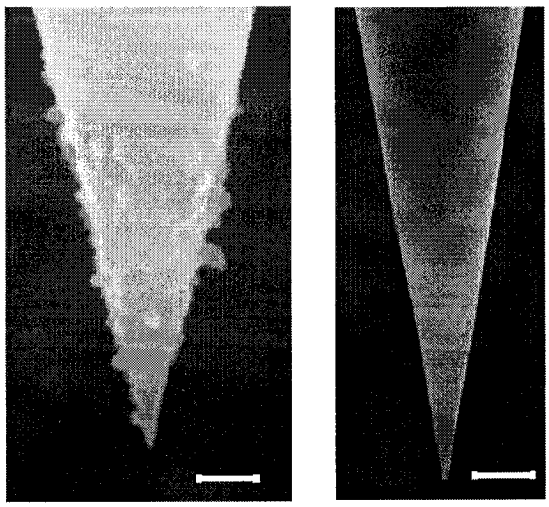

(a) (b)

Figure 2-11. SEM images of (a) normal (Turner) fiber etching and (b) tube-etching methods. The scale bar represents 500 nanometers in both cases.

The final verdict on taper formation is expressed in figure 2-12. Although pulled tips can be created with narrow apexes, their poor reproducibility and long tapers (small taper angles) make them the poorer choice. The etched tips show much better reproducibility (little variation in parameters) together with short tapers (large taper angles), making them superior.

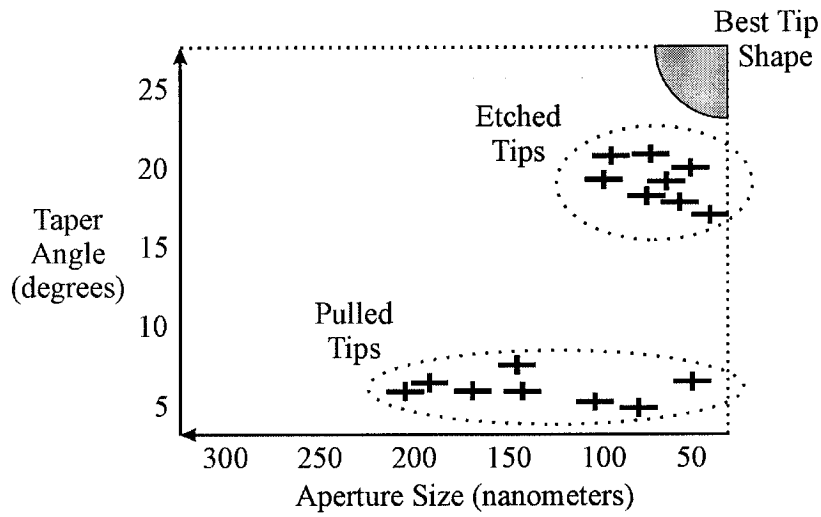

Figure 2-12. Comparison of pulled and etched tip parameters as observed by SEM. Note that to better highlight the trend, the horizontal axis decreases to the right.

Once the etching phase is complete, the fibers are gently removed from the acid and washed in ethanol to rinse off the oil. The fiber tips are then dipped into dichloromethane in order to partially dissolve the plastic jacket. Once softened, a fiber stripper (a pliers-like tool with a fixed clamping diameter) is used to cut the jacket at a point 2 cm up the length of the fiber from the tip. The very end of the jacket is then held with tweezers and gently pulled, leaving the fiber tip exposed. The end of the fiber is then rinsed again in dichloromethane to remove any residue. The fibers are then ready for coating.

In order to batch fabricate the fiber probes, each fiber is wound onto a spool and placed into a carousel (see figure 2-9). The carousel can hold 8 spools and is easily mounted in the fiber etching stage. Once etching is complete and the fiber jackets removed, the carousel is quickly transferred to the evaporator where the newly formed tips are coated with aluminum. The carousel stores the fiber probes until use and each spool may be placed in the SEM for quick imaging of the fibers with very little manipulation. It is crucial to place the tips into the evaporator as quickly as possible since dust begins to gather immediately on the bare fibers. Any such contamination of the fiber surface can lead to the development of pinholes in the aluminum coating. In our case, we manage to place the fibers under vacuum in less than 2 minutes from the removal of the plastic jackets.

Etched probes are generally preferred over pulled probes due to their increased optical transmission and mechanical properties (see figure 2-7).

Although almost all applications use straight fiber probes, bent probes, which are more suitable for use in existing commercial SPMs, are also being developed[58-61]. The added difficulty of bending the fiber results in considerable effort for each probe (see Figure 2-13).

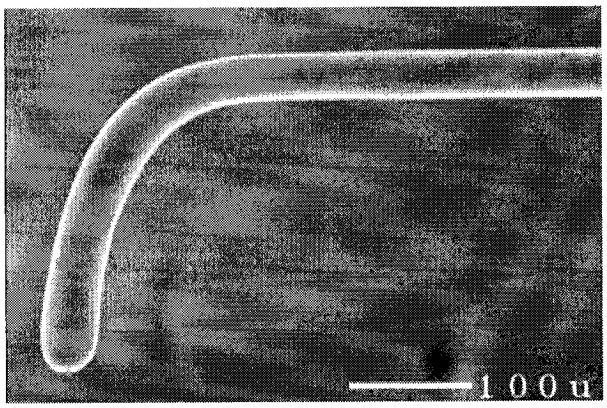

Figure 2-13. SEM image of a bent optical probe tailored for beam-deflection-based microscopes. (From R. S. Taylor and K. E. Leopold, *The Americas Microscopy and Analysis*, p. 11, May 1999 – reprinted with permission)

Optical fibers are the probe of choice for most aperture SNOMs today, however these are usually home-made with considerable effort and often low yields. The field has seen the recent emergence of microfabricated silicon and quartz-based cantilever probes with integrated apertures for illumination SNOM (see Figure 2-14), sub-micron polymer tips for apertureless SNOM and even a single fluorescent molecule used as a light source[38]. Micromachined multipurpose tips for SNOM and AFM use are also being developed[62,63] and hold the great promise of both local excitation and collection through an integrated hollow aperture[64].

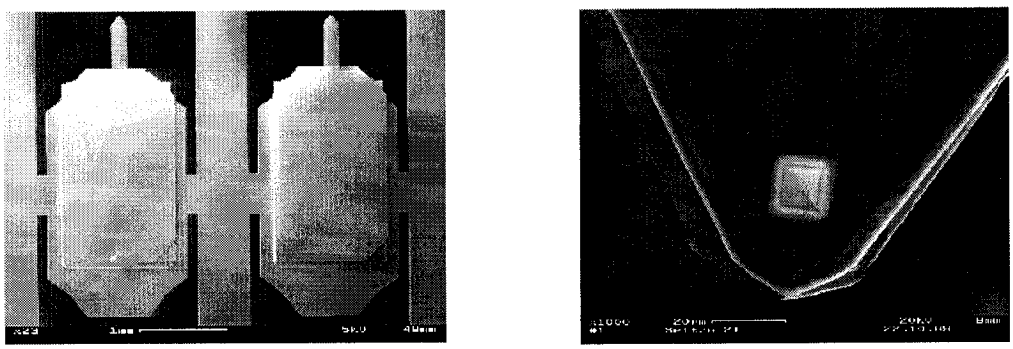

(a) (b)

Figure 2-14. Microfabricated SNOM probes. (a) Silicon sensor probes with mount. (b) Integrated hollow aluminum pyramid with 100 nanometer aperture. (From Wissenschaftliche Instrumente und Techologie GmbH catalog)

Our microscope generates a few hundred picowatts of intensity at the apex, well within the sensitivity of the PMTs. We usually attenuate the laser by 90%, using the neutral density filters, prior to coupling into the fiber. The aluminum coating of the fiber taper can heat up considerably and cause the tip to melt given a high enough incident power. The presence of coating pinholes becomes more evident at high intensities as a bright background (which is often non-uniform) on the optical images, decreasing the contrast of subtle surface features.

2.5 Defining the Aperture

Once tapered, the fiber probes must undergo a further step to properly define their optical imaging aperture. Light traveling down the fiber will reach a point in the taper region where the fiber diameter can no longer contain any propagating modes. Light then leaks out of the fiber, creating an effective aperture which is much greater than the true aperture further down the taper. To restrict the effective aperture size to the apex diameter, a metal coating is added to the taper region which absorbs the light leaking out the sides of the taper. This is almost exclusively done by the physical vapor deposition (PVD) of aluminum. PVD (or vacuum evaporation) is used primarily because it is directional – under high vacuum conditions, evaporated material follows a line-of-sight path which, since the fiber is tilted with respect to the direction of evaporation, covers the fiber taper but not the apex (see Figure 2-15). The fiber is rotated at around 200 revolutions per minute to ensure an even coating on the entire taper. The mean-free path of aluminum in the vacuum chamber can be approximated by[65] $\lambda \approx 3.75\times10^{-5}/P$ where the pressure P is measured in Pascals and λ is in meters. At typical vacuum pressures of $1x10^{-4}$ Pa, we find the mean-free path to be about 40 centimeters whereas the fibers are normally 10 centimeters from the aluminum source. This ensures that the coating process is directional, and that aluminum won't cover the aperture during evaporation.

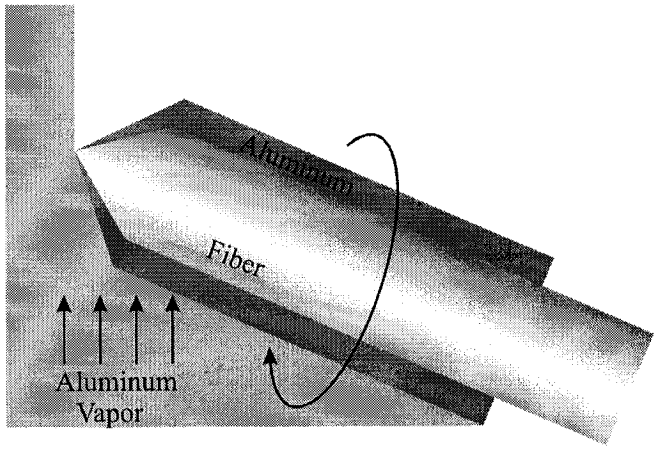

Figure 2-15. Physical vapor deposition of 100 nanometers of aluminum onto fiber probe. The fibers are typically inclined by 15° to the horizontal.

Aluminum is used as the coating because it has the shortest skin depth in the visible spectrum (see Figure 2-2). A coating of 100 nanometers is usually applied to the fiber, corresponding to at least 10 decay lengths (0.0000454% transmission). Thicker coatings tend to produce poorly defined apertures and imaging artifacts (rough coatings create multiple topographical imaging sites – see figure 4-15) since surface roughness increases with thickness[66].

The aluminum coating is applied under the best possible vacuum (typically below $1\times10^{-4}\,Pa$) and at the highest deposition rate possible (typically greater than 50 nm/s) to achieve a smooth covering on the fiber taper. Vapor deposition of aluminum tends to form large grains which cluster together to form crevices (see Figure 2-16a). These crevices act as pinholes, secondary light sources, during imaging which may generate far-field contrast on the optical images. A high evaporation rate creates many nucleation sites on the taper which in turn lead to smaller grain sizes and fewer pinholes[67]. Evaporation rates are limited, however, by the condensation of aluminum on the fiber tip. The phase change can release enough latent heat to melt the fiber. A clean and cool substrate is thus important for smooth coatings[67]. Evaporation filaments which emit as little radiation as possible are used and accordingly, coils are preferred to boats.

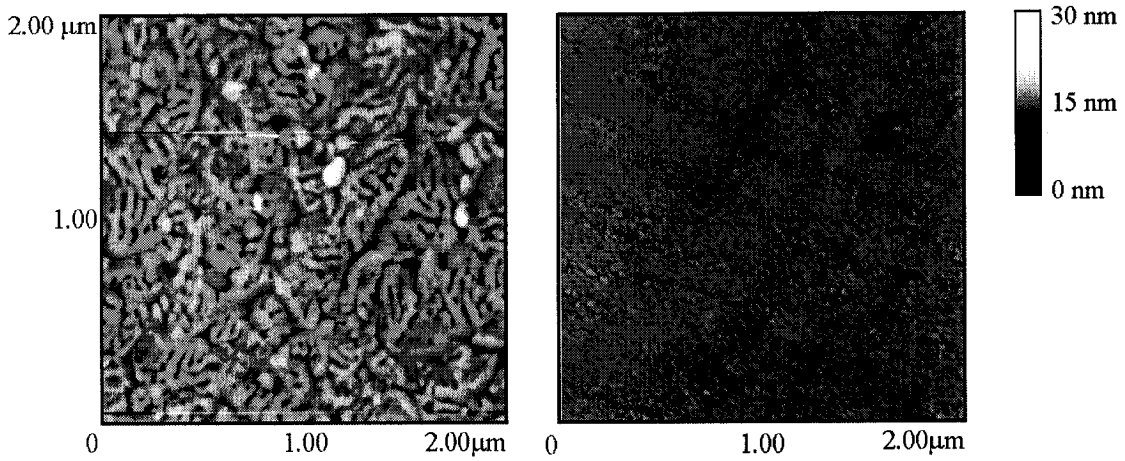

Figure 2-16. (a) AFM image of 100 nanometer thick aluminum film on glass substrate under typical evaporation conditions. Fissure sites are plentiful and may lead to imaging artifacts when scanning. The rms roughness of the film is 5.4 +/- 0.5 nm. The average grain size is (1.2 +/- 0.2)x10^4 nm^2 (b) Investigations are underway by Kaifeng Liang at McGill University to develop an aluminum alloy (here, a 10% copper alloy) which can be deposited as a smoother, or even amorphous, film onto fiber probes. The rms roughness for this film is 0.86 +/- 0.05 nm while the average grain size is 810 +/- 50 nm^2. Both images were acquired in Tapping Mode[‡] at a scanning rate of 1 Hz. The right image courtesy of Dr. Liang.

Once etching of our fiber probes was complete, the fibers were then transferred to a home-built evaporator (see figure 2-17). The choice of a home-built system was based on the requirement of customized hardware in the system. The evaporator focuses on rapid mounting of the fibers (necessary to prevent fiber contamination, and thus the possibility of coating pinholes) as well as a flexible mounting, turning and shuttering setup to maximize fiber probe repeatability. The system consists of a 50.8 cm (20") diameter 304 stainless steel base plate which is 1.59 cm (5/8") thick and has 11 utility ports. The chamber consists of a 43.7 cm (18") diameter 304 stainless steel bell jar which is 76.2 cm (30") tall and has a Pyrex[§] viewport and a Viton[**] gasket seal. Two of the utility ports lead to vacuum pumps – a roughing pump (Edwards model number E2M5) and an ion pump (Ultek refurbished 100L/s). The roughing pump is prefaced by a

[‡] Tapping Mode is a trademark of Digital Instruments, USA. The technique involves oscillating an AFM tip normal to the surface and gently making intermittent contact with the sample.
[§] Pyrex is a trademark of Corning Inc.
[**] Viton is a trademark of Dupont Dow Elastomers

molecular sieve (MDC reference number KMST-100-2) to prevent oil backflow into the pump, and can evacuate the chamber to $6x10^{-2}$ Pa. The ion pump can evacuate the chamber to $1x10^{-4}$Pa. This pressure is limited by the large surface area of our bell jar (more than 2.1 square meters) which adsorbs water vapor. All but two of the remaining ports are occupied. One houses the vacuum gauges (a Pirani gauge Balzers model number TPR 010 and a cold cathode gauge Balzers model number IKR 050), another the crystal deposition and rate monitor (Inficon model number XTM/2). Two ports have high current feedthroughs (MDC reference number K150-MC-2), one has two K-type thermocouples. The final two ports contain the shutter (MDC reference number K100-BRM) and the electrical feedthroughs (two connections each for the DC motor, the baking lamps and a sample heating element).

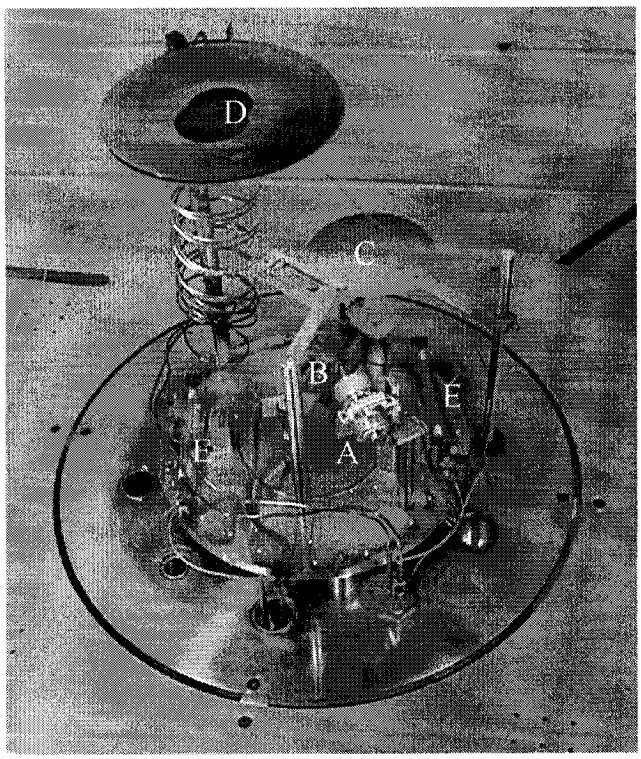

Figure 2-17. Metal evaporator used to coat the fiber probes. (A) Fiber carousel motor (B) Evaporation coil (C) Shutter (D) Rate/Deposition monitor – top view (E) Bakeout lamps.

The inside of the evaporator consists of the water-cooled rate monitor, the sample shutter and the rotating motor. High vacuum motors usually run in the many thousands of

dollars, prohibitive in our case, so an alternative was found in an automobile windshield-wiper motor. The gear box, magnets, armature and commutators were degreased and restored using vacuum compatible glue where necessary. A few holes were drilled to ensure proper venting and the motor, although squeaky, has proved remarkably effective.

The heating filament power supply (Lambda model number LES-F-01-0V C S) provides up to 120 Amperes at 7.5 V_{dc} to the evaporation filament. The best coils for our use (Kurt J. Lesker Company model number EVF93040W) consist of three tungsten wires wound together and formed into 8 loops forming a 12.7 cm (5") long, 0.79 cm (5/16") inner diameter filament. Tungsten filaments are best for coating SNOM probes because of their high molecular-to-radiant flux ratios[68], that is they can achieve high evaporation rates (since the aluminum wets the thin coils) without needing a large surface area (which heats the sample).

During evaporation, the filament is filled with around 2.5 cm^3 of 99.999% pure aluminum and slowly heated. The aluminum heats up, increasing its vapor pressure until it reaches 660 °C at which point it melts, wetting the tungsten coil and increasing the deposition rate dramatically. The fibers, mounted on the carousel, are held about 10 cm from the filament and rotated at about 200 turns/minute. A deposition rate of around 100 nanometers/second or more is desired in order to reduce the grain size of the aluminum of the fiber taper and eliminate optical pinholes[43]. High evaporation rates also limit the formation of Al_2O_3 which, since it forms a transparent thin film, would compromise the effectiveness of the fiber coating. Once the evaporation is complete, the fiber probes are removed from the evaporator and stored in a dust-free container until they are unwound from the spools and mounted into the SNOM. The development of our own evaporator not only maximized our coating flexibility but also ended up costing one-tenth the cost of a commercial system.

Alternate coating methods have been developed with varying success. Sputtering and chemical vapor deposition (CVD) techniques have produced smooth aluminum coatings but these methods also coat the tip apex. To create the optical aperture, groups have

turned to carefully rubbing or grinding the tip[4,69], electrical arcing between the tip and sample[70], focused ion beam (FIB) milling[71] and solid electrolytic erosion[72].

When using coated SNOM probes at high input powers (above a few tens of milliwatts of laser power coupled into the fiber) the aluminum coating can absorb too much intensity and begin to melt the glass fiber tip. This effectively limits the output power from the fiber probes to the microwatt or nanowatt regime[73,74].

2.6 Shear-Force Distance Control

Precise control of the distance between the sample and the tip is crucial for two main reasons. First, theoretical[75,76] and experimental[77] studies demonstrate that the sample's highest spatial frequencies decay most rapidly with distance. Substantial information is lost even at a probe-sample spacing of 5 nanometers and so exceptional care must be taken to maintain the tip within this distance to the sample. Second, since light intensity from the tip decays exponentially, a constant optical signal (and so the proper interpretation of SNOM images) is only achieved under careful distance control. Early microscopes used electron tunneling as the primary distance control[4,78] then contact repulsion forces looked promising[79,80], but most SNOMs today use a form of non-contact interaction called "shear-force"[38,81,82]. The fiber is fixed onto a displacement sensor (often a quartz tuning fork) and is oscillated, by less than a nanometer, parallel to the surface at its resonant frequency. As the fiber interacts with the surface, the oscillation amplitude, frequency and phase change sharply with distance providing a sensitive feedback mechanism.

The exact nature of the shear-force interaction is poorly understood. There is evidence to suggest viscous damping due to a thin water layer on the surface plays a large part[83,84], as does friction between the tip and sample[85]. Frictional effects result in chemical sensitivity of the interaction as these also depend on the compositional heterogeneity of the surface, not merely on the topography[86]. Intermittent contact, or "knocking", with the

surface may also contribute significantly[87] as shear-forces are still present at ultrahigh vacuum and liquid helium temperatures[88,89]. Additionally, shear-forces are still present when imaging while immersed in liquid[90] and though contrast is poorly understood, it clearly depends on the chemical composition of the sample. Thus, by using feedback to keep the shear-forces constant, one is not necessarily keeping the tip-sample separation constant.

Using tuning forks as shear-force sensors is not without its intricacies. The fiber probes can apply a significant torque to the fork prongs and the mechanics of glueing the fiber affects the properties of the sensor dramatically. Both the resonant frequency and the Q-factor of the shear-force probe may increase or decrease once the fiber is attached. Often, a low Q-factor arises, severely limiting the sensitivity of the instrument. Nevertheless, shear-force is by far the most popular implementation of distance control in SNOM.

An alternate distance control method, similar to an intermittent contact oscillation mode used in AFM, has made a small impact on SNOM. In this mode, the fiber is glued onto the end of the tuning fork and the sensor is oscillated normal to the sample, touching the surface lightly at the end of each stroke. The oscillation amplitude is used as a feedback setpoint in order to generate the sample topography. Though the contrast obtained in this mode is more straightforward than in shear-force, it has been used with limited success since the fiber has a large spring constant in this oscillation mode and the sharp aperture is prone to wear. No near-field contrast images have been obtained yet using this distance control method.

2.7 Imaging Contrast and Cross-Talk

Several types of microscopy yield resolutions beyond the ~50 nanometers routinely achievable by SNOM, notably the SEM, AFM and STM. None, however, can draw as effectively upon the wealth of features of optical microscopy. Changes in absorption,

reflection, polarization, index of refraction, luminescence and fluorescence can be detected in the near-field, making SNOM a high-resolution optical microscope[91,92].

SNOM image, both the shear-force and wavelength channels, are generally rich in detail. Relative distance and optical contrast of the sample features can be determined with high precision. However, a fundamental understanding of the contrast, including the wavelength-dependence is still not available. SNOM models such as those in section 2.2 don't take into account the scanning process itself. Actual SNOM scans, which rely on the rapidly-decaying evanescent waves and the intricate set of boundary conditions of the sample-probe system[93], are a challenge to model properly. Heterogeneous compositions and complex topographies make for real-world samples which are beyond the scope of today's models. For example, the force-feedback mechanism for distance control relies on a different coupling between the probe and the sample than that which governs the intensity emanating from the tip. Over a rough surface, the sample can interact with different locations on the probe tip resulting in subtle height changes across features which may generate a distinct optical contrast (see figure 2-18). Some of the shear-force mechanisms, such as friction, may also simulate a change in topography while scanning a flat but heterogeneous sample. Additionally, the feature on the tip providing the force feedback has a non-negligible shape as does the optical aperture itself. The corresponding SNOM images may be convolutions of the sample shape and tip geometries, including a possible offset between the topography and optical images (see figure 4-15). SNOM still generates a wealth of knowledge beyond the diffraction limit and similar modeling challenges are present in all Scanning Probe Microscopy fields.

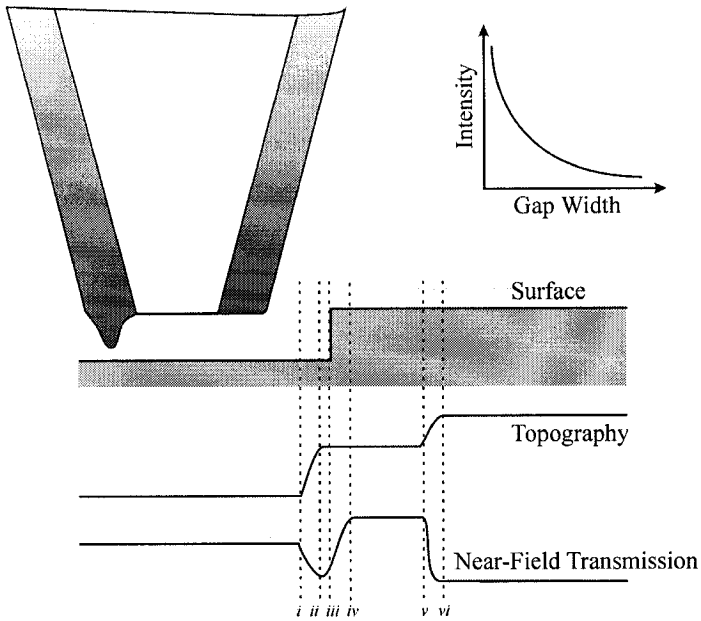

Figure 2-18. Optical and topographical cross-talk with a rough tip. A simple step feature on the sample results in a complicated near-field signal due to the nature of SNOM contrast. During imaging of the flat surface, the protrusion at the left interacts most strongly with the surface and determines the tip-sample spacing. At point *(i)*, the right side of the tip begins to interact with the step edge and causes an increase in separation. Since the optical aperture is now further from the surface, the transmitted intensity drops. At *(iv)*, the aperture has moved over the step surface and transmission increases due to the decrease in gap width. At *(v)*, the tip protrusion encounters the step and the tip-sample spacing increases again, resulting in a lower near-field transmission due to the increase in sample thickness.

The presence of cross-talk may actually be a major source of purported SNOM contrast, even in published articles[32,94]. Credible near-field images, taken under constant force mode, should therefore exhibit one of the following distinctions (adapted from reference 32):

i) That the resolution of the shear-force and optical images be different.

ii) That the shear-force and optical images be uncorrelated

iii) That any correlated features be offset by a constant amount

To this list, we add a fourth condition which is relevant to our studies:

iv) That optical contrast be different for separate wavelengths

The presence of a second wavelength in SNOM imaging has advantages other than the identification of cross-talk and other scanning artifacts. Almost all optical contrast mechanisms are sensitive to wavelength. Having two optical images of the sample thus permits the contrasting of features in order to obtain more information about the sample. For example, comparing transmission ratios of specific features at different wavelengths allows the discrimination of various chemical species in the sample. Contrasting wavelengths also allows the investigation of the shear-force mechanism. A distinction can now be made between a change in topographical signal caused by a surface feature (where the increase in thickness of the sample causes both intensities to decrease) and one caused by a change in friction (where a different surface chemistry would change the relative intensities of both optical channels).

Samples suitable for transmission SNOM are typically very thin, a few tens of nanometers at most. The evanescent nature of the light intensity, combined with the emission's sensitive dependence on probe-surface boundary conditions, make for an optical signal which is most sensitive to the very surface of the sample. Naturally, optical absorption and scattering do occur deeper into the sample, however since these effects occur in the far-field, they will exhibit poor spatial resolution.

An alternate operational mode is to scan at a constant *height* rather than at a constant *force interaction*. In this mode, no positional feedback is given to the tip/sample so that the aperture moves within a plane parallel to the mean sample surface. In cases where the tip size is sufficiently small compared to sample feature size, this mode results in optical contrast dependent predominantly on the sample topography, not on tip shape or surface chemistry which contribute to shear-forces. Though dependent on topography, the contrast is optical in nature and thus is not an artifact. Scanning without feedback, though, increases the risk of the tip crashing into the surface and so samples with low topography are preferred. Topographical cross-talk is not completely eliminated in this mode since the near-field intensity is still sensitive to the exact boundary conditions between the tip and sample.

To summarize, Scanning Near-Field Optical Microscopy uses tapered optical fibers as sub-wavelength sources of light to perform optical imaging on an unprecedented scale. SPM techniques are used to control the probe's position over the sample and sensitive detectors are used to generate the optical images. Image analysis can be challenging due to the complexities of shear-force scanning and the non-trivial boundary conditions involved between the probe and the sample. The inclusion of a second wavelength can shed some light on these processes as well as provide chemical contrast beyond the optical diffraction limit.

Chapter 3

Microscope and Probe Tip Design

3.1 Instrumentation

We developed a transmission-mode, aperture-based SNOM which operates at two wavelengths simultaneously – one at 442 nanometers (blue), the other at 325 nanometers (ultraviolet). The choice of using ultraviolet light was motivated by our desire to probe organic samples which show strong absorption or fluorescence in the ultraviolet. We chose to implement shear-force feedback using a quartz tuning fork as our detector[95]. The simple SNOM construction is modular and versatile, including mostly off-the-shelf components. We investigated both pulled and etched tips and have developed a modified etching procedure which routinely produces smooth narrow apertures with large taper angles.

3.1.1 General Microscope Design

The design of our microscope is inspired in part on an instrument developed at the University of Basel, Switzerland[96]. All components are fastened to a vibration isolation workstation (Newport Instruments model number M-VW-3660-OPT-02-10) which provides damping at frequencies below 100 Hz (typical building vibration frequencies – see figure 3-1).

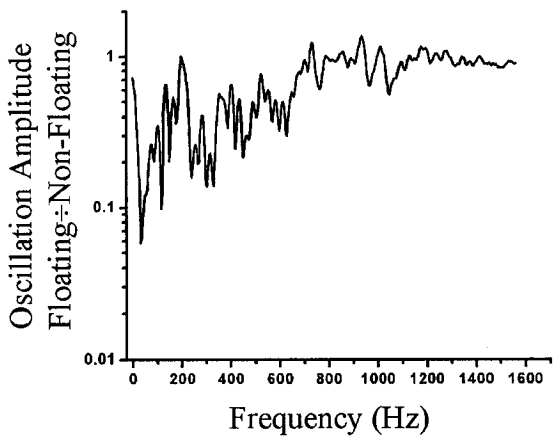

Figure 3-1. Transfer function of the passively-damped optical table shows building vibrations are reduced considerably, especially at low frequencies.

The light source is a Helium-Cadmium laser (Kimmon model number IK5451R-E) which can provide 300 mW at 442 nanometers and 200 mW at 325 nanometers simultaneously. Neutral density filters (Omega Optical model numbers 550ND.3 550ND.5 and 550ND1.0) can rotate into the path of the beam and attenuate it by as much as 97%. The laser light is channeled into the fiber probe using a 5-axis fiber aligner (New Focus model number 9091) and a 20X objective lens (Optics for Research model number LMU-20X-NUV). The fiber coupler allows drift-free alignment to better than 100 nanometers.

The tapered end of the fiber probe is fixed to the end of the force-feedback detector (see figure 3-2). It is bonded, using a cyanoacrylate glue, to one of the tines of a quartz tuning fork (Raltron model number R26-32.768KHZ). The tuning fork is glued to a removable holder which is secured, using a set screw, to a 2.5 cm long dither piezo (Staveley Sensors). The dither piezo is fixed, using 5 minute epoxy, to a 10 cm long aluminum shaft. This shaft is held tightly to the frame of a second 5 axis fiber aligner.

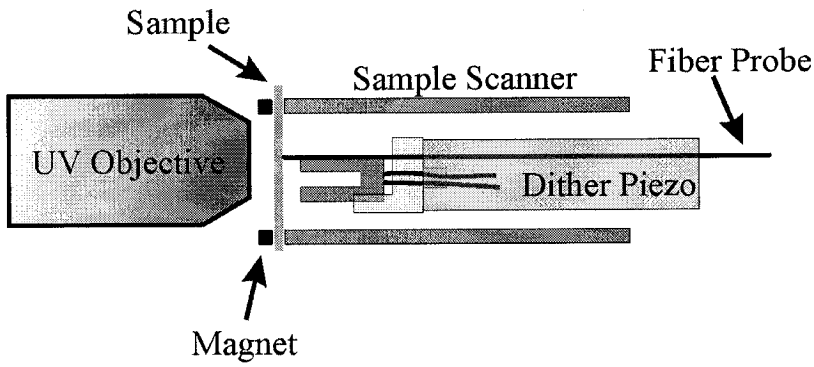

Figure 3-2. Diagram of sample scanning geometry.

On the adjustable platform of the fiber aligner, and concentric with the force-feedback assembly, sits the sample scanner – a 6.35 cm (2.5 inch) long, 1.27 cm (0.5 inch) outer diameter and 0.05 cm (0.02 inch) thick walled piezoelectric tube (Staveley Sensors ELB#3 PZT) with an inner and four outer nickel electrode quadrants. While acquiring data, the outer tube is scanned with respect to the fixed dither piezo. For transmission mode measurements, the samples are mounted onto thin (0.17 mm) glass coverslips which are then held firmly, by Samarium-Cobalt magnets, to a steel ring glued to the end of the scanner tube. The fiber aligner is used to make adjustments to the position and alignment of the scanner tube relative to the fiber tip along three orthogonal axes and 2 rotational axes. It can be used to select an appropriate location on the sample for imaging.

When the scanner tube is perfectly concentric with the inner tube and the sample is approached to within a few microns of the fiber tip, a computer-controlled stepper motor provides fine adjustment (in 20 nanometer steps) of the tip-sample distance. Note that the fiber probe tip and scanner tube describe essentially an AFM which acquires topographical images by measuring shear-forces (see figure 3-3).

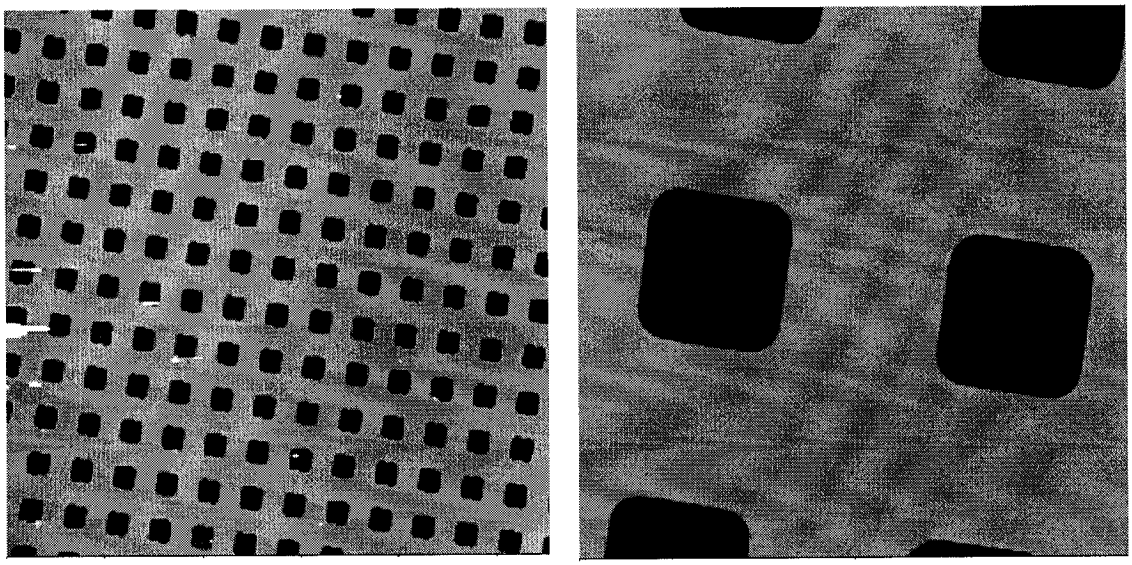

Figure 3-3. Topography of microfabricated silicon calibration grid (Digital Instruments – the 180 nanometer deep holes are 5 micron long squares and are separated by 5 microns) using shear-force feedback. (a) Large range of 2½ inch long sample scanner. (b) High-resolution scan of center of grid. The 512x512 pixel images were acquired at a scan rate of 0.1 Hz.

To implement the optical half of the SNOM, it is necessary to align the fiber probe tip with an optical collection system – essentially a simple confocal microscope. The second fiber coupler is fixed onto an X-Y-Z translational stage (Newport Instruments model number 462-XYZ-M with ultrafine screws model number AJS-1) which provides precise alignment of the scanning components with the optical axis of the microscope (see Figure 3-4). The optics consist of a microscope objective (40X magnification, 0.28 N.A., Optics for Research model number LMU-40X-NUV), a dichroic mirror (Acton Research fused silica mirror with coating number 308-353-BBFR45) and two photomultiplier tubes (PMT) (Hamatsu model number H5920-01 integrated photon counting head). Each PMT can be positioned in 3 dimensions using an X-Y-Z translational stage (New Focus model number 902062-01).

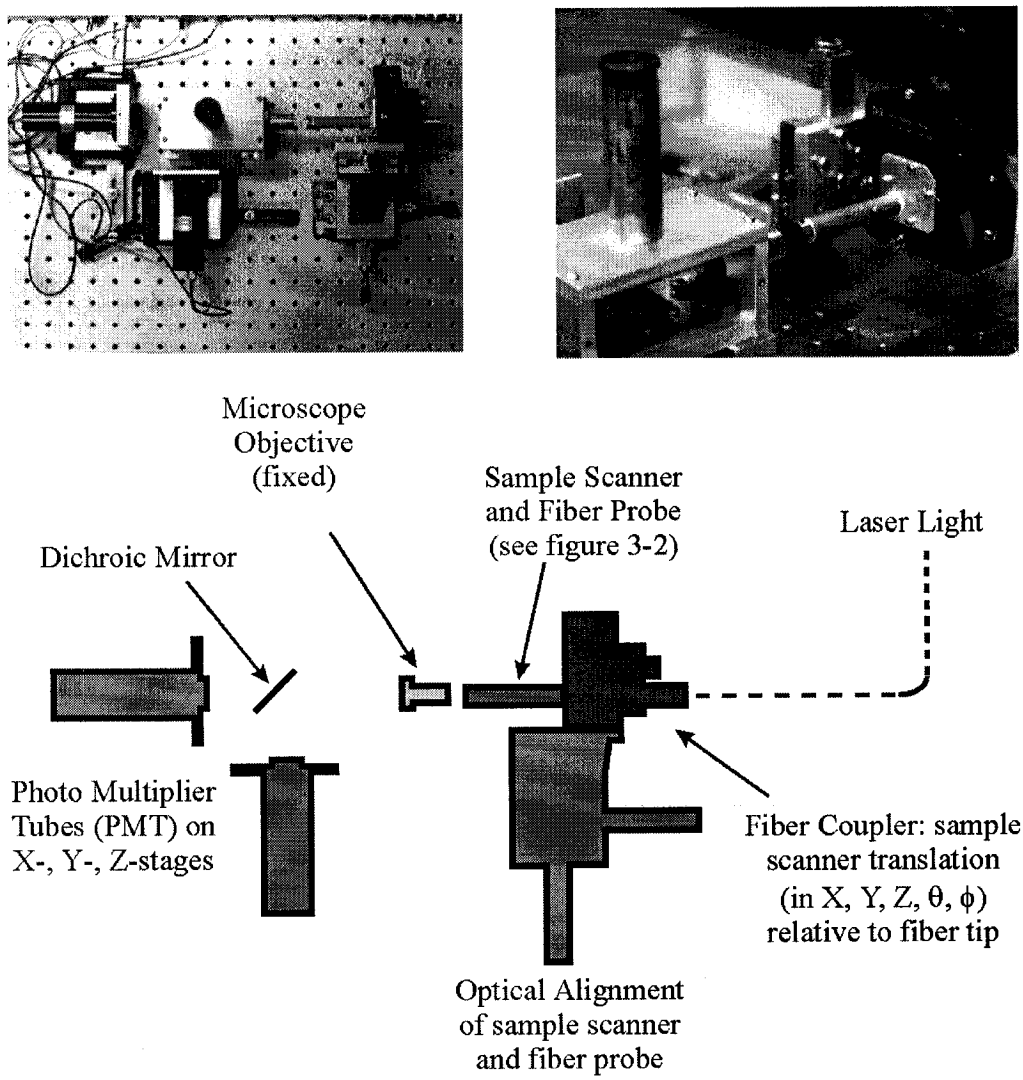

Figure 3-4. Optical axis of microscope.

The coating on the mirror reflects 95% of incident light at 325 nanometers but is transparent to light at 442 nanometers. The PMT along the axis of the scanner is used to detect the "blue" light and is equipped with a 50 micron pinhole (Newport Instruments model number PNH-50) and a bandpass filter (Ealing Electro-Optics model number 35-8142) which has a peak transmission of 30% at 441.5 nanometers and a transmission width of 0.9 nanometers. The PMT at right angles to the scanner detects "UV" light and is equipped with a 100 micron pinhole (Newport Instruments model number PHN-100) and a 1 millimeter thick piece of UG-11 glass (Esco model number S284011). UG-11 glass has a peak transmission of 70% at 325 nanometers and an optical density of greater

than 8 for wavelengths between 400 and 675 nanometers. The role of the pinholes is to ensure that the light incident on the detectors is collected solely from the probe tip volume, a confocal arrangement. The filters' function is to further reduce stray light as well as eliminate wavelength cross-talk between optical channels.

The microscope is located in its own room and is operated in the dark. With all light sources off, we measure a background count of 10 counts per second (cps), corresponding to the dark count rate of the PMT. The computer screens face the PMTs but contribute only slightly to the background. Even so, these are normally turned off during the scan. It is even possible to operate the SNOM with the door open and the lights on (see table 3-1), as only a small offset in the optical images results.

	325 nanometers (cps)	442 nanometers (cps)
Dark Count	12	10
Computer Screens	120	30
Room Lights On	2,250	4,800
Typical Operating Count Rate	> 10,000	> 600,000

Table 3-1. Count rates for operation of SNOM. Numbers represent the combined effect of PMT filters and wavelength response.

The data acquisition is done simultaneously for both the shear-force and optical channels. The voltage signal from the tuning fork is sent to a Lock-In Amplifier (Stanford Research Systems SR830). The output signal from the Lock-In is added to a setpoint voltage (see figure 3-5) and then sent to our main control unit, a Nanoscope IIIA controller from Digital Instruments. The IIIA provides feedback for the tip-sample separation (by means of the signal applied to the Z-piezo), controls the scan parameters (by means of signals to the X- and Y-piezos), and acquires and processes all SNOM signals. The controller features a 20MHz Digital Signal Processor (DSP) and three 16-bit digital-to-analog converters (DAC) for each of the X, Y, and Z axes. It has a host of calibration features and a number of off-line analysis routines as well as a reasonably user-friendly interface. The optical channels of the controller feature 8-bit, 16 MHz pulse counters which are

sampled at 62.5 kHz ($16x10^6/62.5x10^3 = 256 = 2^8$) and averaged depending on the scan rate and resolution. The count rates are then scaled, as are the Z-piezo voltage values, to 16-bit resolution (see Appendix). In order to maximize flexibility, we have implemented an input/output signal box between the microscope and the controller (Signal Access Module from Digital Instruments).

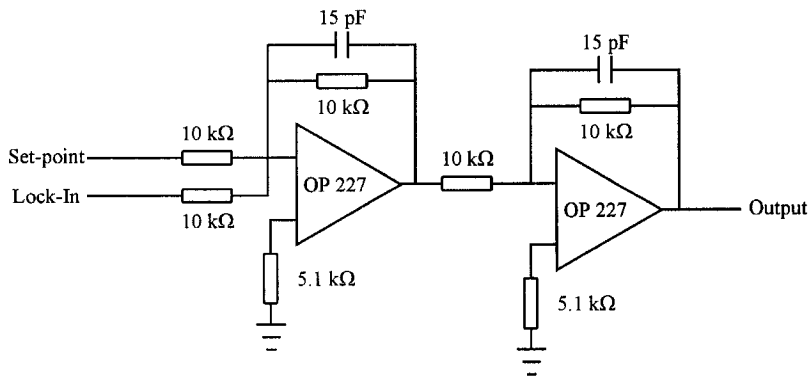

Figure 3-5. The tuning fork signal is combined with the set-point voltage from the feedback controller. The result is inverted in order to behave properly with the Nanoscope software which adjusts the voltage to the Z-piezo to maintain an "output" level of zero volts. When the tuning fork oscillation decreases, the "output" becomes negative (a negative set-point is used) and the tube is extended (moved away from the tip). When the tuning fork signal increases, the "output" becomes positive and the tube is retracted (moved towards the tip).

The feedback controller allows the independent adjustment of proportional, integral and look-ahead gains. These regulate the position of the tip over the sample by monitoring the error signal ***E*** (that is, the setpoint value minus the detector signal) and modifying the voltage applied to the Z-piezo. The look-ahead gain works by anticipating large changes in surface features, based on previous scan lines, and applying a simple offset to compensate, positioning the scanner in the range where the proportional and integral gains can operate effectively. It is used to weight the integral gain as follows: $G_{LA,Int}=z_x+L_A*(z_{(x),(y-1)}-z_{(x+1),(y-1)})$, where L_A is a user-controlled variable and $z_{(x,y)}$ is the height value of the $(x,y)^{th}$ pixel on the image. Look-ahead gain works well in samples with regular features but is a hindrance otherwise. In our SNOM studies, look-ahead gain was turned off. The integral gain corrects for cumulative error by integrating the total error $\bar{z} = I\int E\,dt$, where I is a user-controlled variable, and is used to calculate a running

average of error as follows: $\bar{z}_{new} = G_{LA,Int} * E + \bar{z}_{old}$. Finally, the proportional error is determined and the final correction voltage is sent to the Z-piezo:

Z-voltage = $\bar{z}_{new} + P*E$, where P is a user-controlled variable.

3.2 Force sensor

One of the most effective oscillation detectors used in SNOMs today is a single crystal quartz tuning fork. These are made by the millions for use as precise time standards in watches. The tuning fork is held at its base and the two tines are oscillated in their asymmetric mode. Dissipation is minimal in this mode and Q-factors are large (over 10^5 in vacuum and over 10^4 in air). In SNOM, the optical fiber probe is fixed to one of the tines, protruding less than 1 millimeter (see figure 3-6), and the probe-tuning fork assembly is oscillated at its resonant frequency, around 32.768 kHz, with a Q-factor of between a few hundred and a few thousand. The Q-factor of the probe assembly varies greatly depending on the efficiency of holding the tuning fork and of fixing the fiber to one of the tines. In this scheme, the probe assembly has a sensitivity of greater than 1 nN[97].

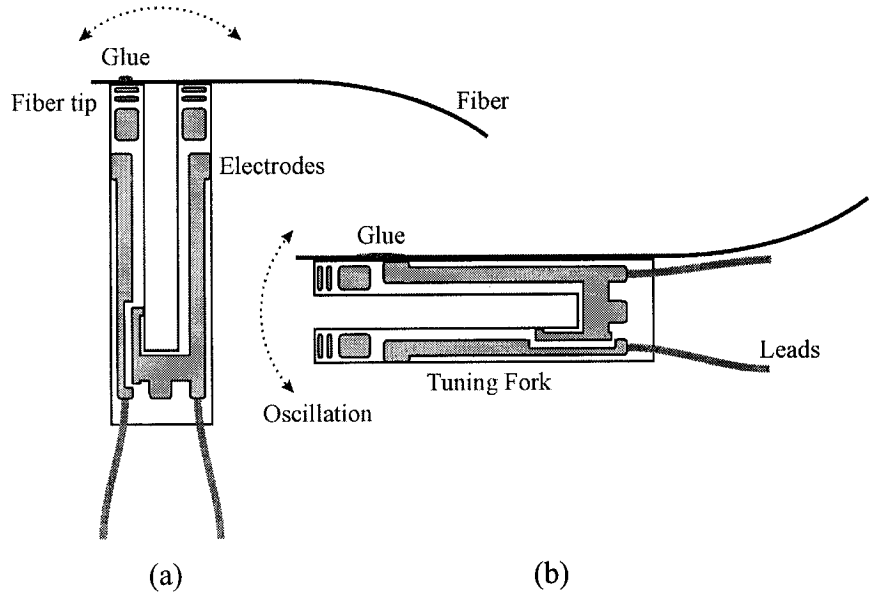

Figure 3-6. Two alternate setups for fixing the fiber probe onto the tuning fork detector. (a) Contact or intermittent contact mode (b) Shear-force mode. In both cases, the sample is normal to the axis of the fiber.

To ensure the proper tracking of the aperture over the surface, the force between the probe and the surface is monitored and kept at some constant setpoint. This is done by oscillating the probe at its resonant frequency and measuring changes in the oscillation amplitude, phase or frequency of the tuning fork as the probe interacts with the surface. Lock-In detection is most common and, with a proportional-integral based feedback system, one can observe probe deflections well below 1 nm[98]. Amplitude response times are characterized by a time constant of $\tau = 2Q\sqrt{3}/\omega_0$ where ω_0 is the resonant frequency. Though faster responses can be used, our best results have used a settling time of 5τ (to 1% of original amplitude) resulting in a scan time of 85 milliseconds per data point. For a scan of 256 by 256 points, this results in a scan time of 90 minutes per image.

The fiber probe is implemented as a force sensor much like a standard cantilever arrangement in AFM (see figure 3-7).

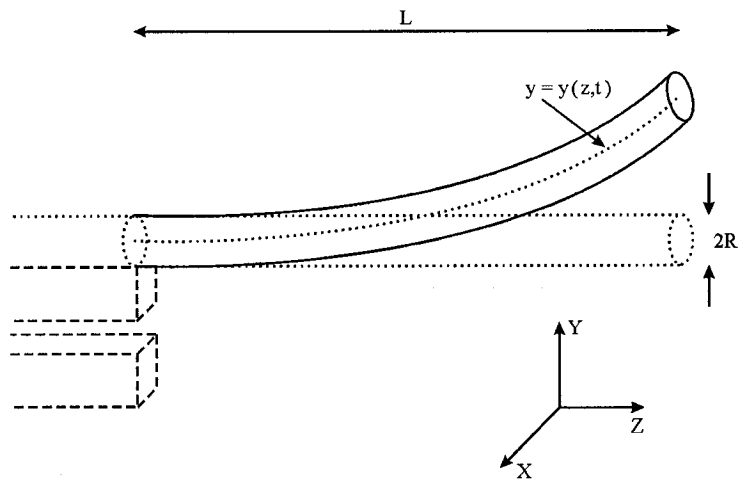

Figure 3-7. The fiber probe of radius R, is fixed at one end (to the tuning fork) and extends out a length L.

The equation of motion for such a system is given by[99]

$$EI\frac{\partial^4 y}{\partial z^4} = -\left(\mu\frac{\partial^2 y}{\partial t^2} + \alpha\frac{\partial y}{\partial t}\right) \tag{3.1}$$

where E is Young's modulus (about 79 GPa for quartz[100]), I is the area moment of inertia[††] about the fiber axis ($\pi R^4/4$ for this geometry), μ is the mass per unit length and α is a damping parameter. The assumption that damping is proportional to velocity is implied in the viscous behavior of shear-force interactions. These interactions being beyond the scope of this thesis, we shall limit ourselves to the undamped behavior of the fiber probe where $\alpha = 0$.

In this case, the spatial and temporal components of equation 3.1 may be separated by assuming a solution of the form $y(z,t) = y(z)e^{i\omega t}$ for which we obtain

$$\frac{\partial^4 y(z)}{\partial z^4} = \kappa^4 y(z) \tag{3.2}$$

where $\kappa^4 = \omega^2\mu/EI$. This has a general solution of the form

$$y(z) = a_1\cos(\kappa z) + a_2\cosh(\kappa z) + a_3\sin(\kappa z) + a_4\sinh(\kappa z) \tag{3.3}$$

[††] Also called geometric moment of inertia and polar moment of inertia, this is the second moment of area.

whose free parameters a_i are given by the initial conditions, in our case:

$$y(0) = y'(0) = y''(L) = y'''(L) = 0$$

This leads to a transcendental equation for determining the product κL,

$$\cos(\kappa L)\cosh(\kappa L) + 1 = 0 \tag{3.4}$$

which may be solved numerically. The first three solutions are shown in table 3-2.

	κL	ν (kHz)
Fundamental	1.875	37.184
1st Harmonic	4.694	58.835
2nd Harmonic	7.855	76.109

Table 3-2. First three resonant frequencies for fiber probe assuming an extension, L of 1 millimeter and a density for fused silica of 2650 kg/m^3.

Assuming this geometry, we may also write down an expression for the spring constant of the fiber. Based on a generalized form for the spring constant of a cantilevered beam[101,102], the spring constant of our fiber becomes

$$k_{\text{fiber}} = \frac{3\pi E R^4}{4L^3} \tag{3.5}$$

which is about 2,800 N/m for our fused silica fibers. Using a similar expression for the tine of the tuning fork, we obtain a spring constant of 26,600 N/m. At almost 10 times the stiffness of the fiber, the tuning fork may be considered as infinitely stiff in our model. A more detailed model including the effects of damping, internal friction and the taper shape of the fiber has been developed[103] but must be solved numerically. Comprehensive models which include the effects of both the fiber and the tuning fork rely on numerous fitting parameters and so far have revealed little insight into the observed behavior of SNOM probes.

A fiber probe is incorporated into the SNOM by first threading the non-tapered end through the inner (imaging) tube then fixing it to one of the tines of the tuning fork using

cyanoacrylate glue or a UV-curable acrylic (Electro-Lite Corporation ELC type 4481). The glueing process requires a few hours (see figure 3-8).

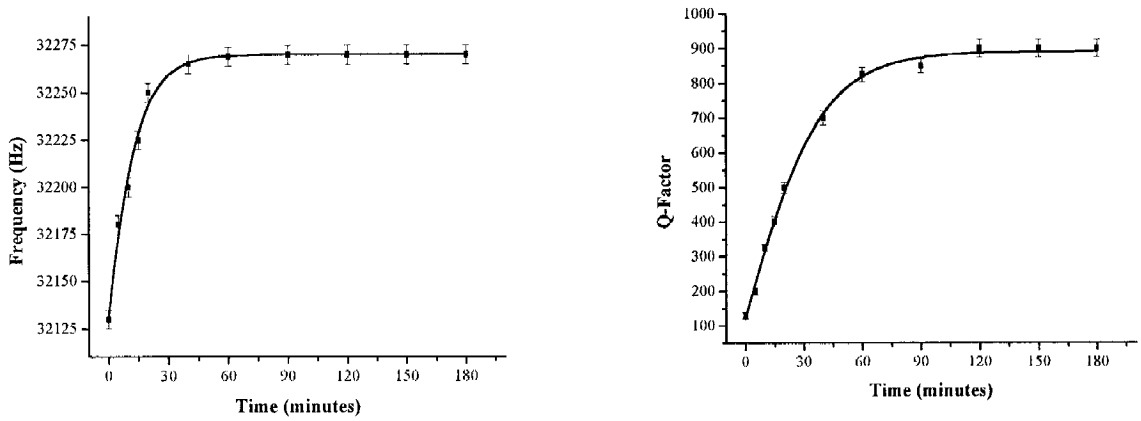

Figure 3-8. The process of glueing the fiber onto the tuning fork takes a few hours. Both (a) the resonant frequency and (b) the Q-factor of the fiber and tuning fork system typically increase as the glue dries.

One would expect a decrease in resonant frequency once the fiber, which has some weight, is coupled to the tuning fork. The use of cyanoacrylate glue, which has a small surface tension and so tends to cover the length of the tuning fork tine, instead stresses the quartz leg, increasing the resonant frequency. The data in the two plots of figure 3-8 are best fit to a sigmoid function of the form $f(t) = \frac{A_1 - A_2}{1 + e^{\alpha(t-\tau)}} + A_2$. The resonant frequency approaches an asymptotic value, A_2, of 32,270 +/- 2 Hz and has a width, $1/\alpha$, of 11 +/- 3 minutes. The Q-factor has an asymptotic value of 890 +/- 10 and a width of 20 +/- 3 minutes.

The tip extends out horizontally less than a millimeter from the edge of the tuning fork. The dither piezo oscillates the tuning fork/fiber probe assembly at its resonant frequency (see figure 3-9) with a fiber tip amplitude of about 0.3 nm, as measured by a home-built interferometer[104].

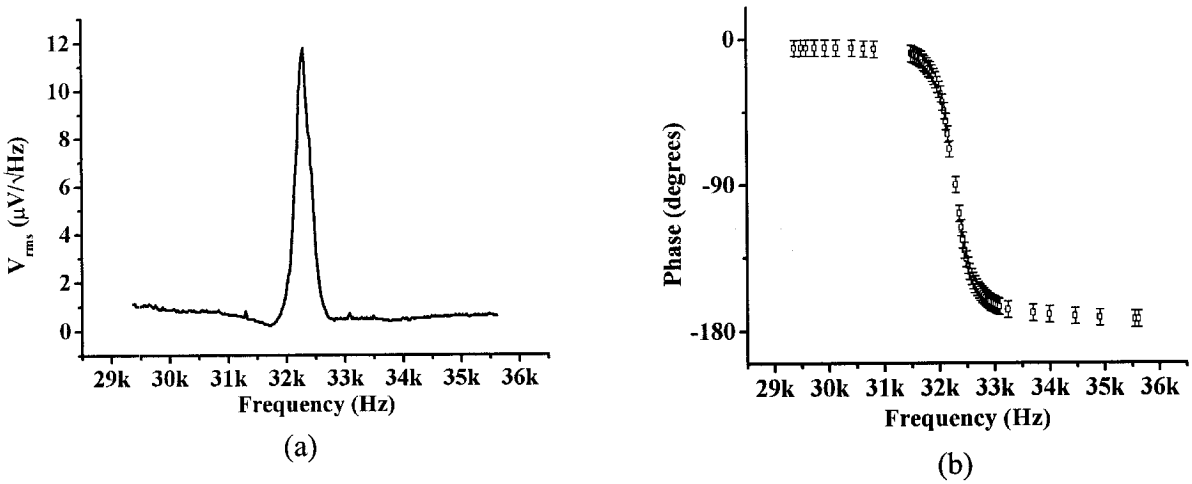

Figure 3-9. Oscillation spectrum for fiber probe mounted onto tuning fork. (a) Power spectral density of oscillation amplitude. The Q-factor here is as low as is generally usable, at about 220. (b) Phase relationship between the drive and response signals. Damped harmonic oscillator behavior is evident in both curves.

3.3 Sensitivity and Stability

As the sample is brought close to the tip of the fiber, forces between the tip and the sample act to dampen the oscillation. The tuning fork signal is sent to a Lock-In detector whose output is fed into a feedback controller. By setting a constant amplitude setpoint during scanning, the tip maintains an interaction with the sample, which generally translates to a constant separation distance between tip and sample. This distance is usually set at around 5 nm. Tip-sample interactions are short range (see figure 3-10).

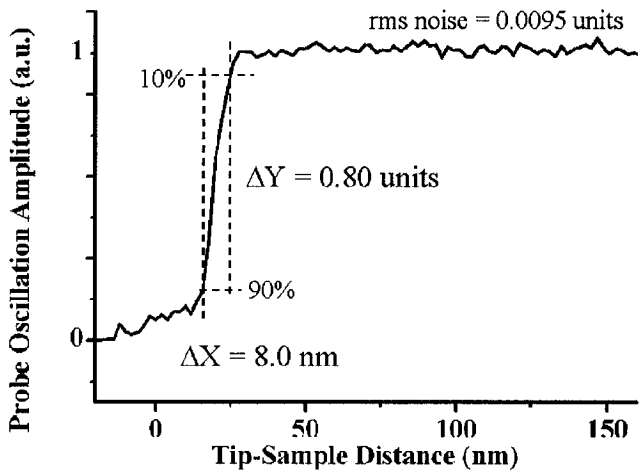

Figure 3-10. The oscillation amplitude of the fiber tip decays from its free-oscillation value to zero (when in contact with the surface) in 20 nm. The data was acquired at a tip approach velocity of 5 nm/second.

The signal to noise ratio (SNR) and resolution in the Z-direction can be calculated using the difference between the 10% and 90% approach curve values[105,106]. The values are SNR = 84.2 (calculated as $\Delta Y / \text{rms noise}$) and the resolution, δZ = 0.095 nanometers (calculated as $\Delta X/SNR$). Indeed, we have clearly observed structures as small as 0.5 nm in height (see figure 4-8b).

By scanning the same region of a calibration sample for a number of hours and measuring offsets between subsequent scans, we obtain a limit of the lateral drift of the microscope of 200 nanometers per hour in the Y-direction (slow scan axis) and 50 nanometers per hour in the X-direction (fast scan axis). The greater drift in the Y-direction is difficult to explain. One would expect piezoelectric effects, such as creep, to effect both axes equally. However, some symmetry breaking does occur. Since the drift is invariably in the direction of gravity, a stick-slip effect along the fast-scan direction is a likely cause. This motion is due to the rapid acceleration experienced at the end of each scan line as the tip returns to the start of the scan border. The sample may be jostled during this motion and gradually shift from under the sample holder. This situation does not occur in instruments where the scanning tube and sample are mounted vertically.

The Na-K type photomultiplier tube used in this work has an integrated photon counting head and is designed to measure single-photon events with a very low dark count (see table 3-1). The assembly consists of a head-on PMT, a low-noise preamplifier, a dual-level discriminator, and a pulse shaper together with a TTL output. The discriminator is set to eliminate events due to both thermionic emission of electrons as well as radioactive and cosmic ray events. The pulse shaper shortens pulse fall-time and eliminates ringing. In order to confirm the behavior of the optical channels in the SNOM, an experiment was simulated by approaching the tip to a clean glass coverslip and performing a scan of size 0.0 nanometers. The topography image was discarded but the count rate data was collected in the usual manner as a series of values for every pixel in the image. The two 256x256 pixel images (one for each wavelength) containing the count rate data were exported and a histogram of the rates was plotted. Both plots were fit to a Gaussian curve and the standard deviations were determined from the fit (see figure 3-11). The ultraviolet channel had a mean rate of 50,014 cps and a standard deviation, σ, of 223 +/- 2. The blue channel had a mean rate of 949,550 cps and a σ of 971 +/- 6. Noise due to the statistical incidence of photons into the PMT should approximate a Gaussian for a large number, N, of photons and the standard deviation of the count rate should scale as $\sqrt{N}$. The square root of the means are 225.9 and 974.4 for the ultraviolet and blue channels respectively, which correspond well to the fit values. This indicates that the optical channels of the instrument are limited to the counting statistics of the measurement.

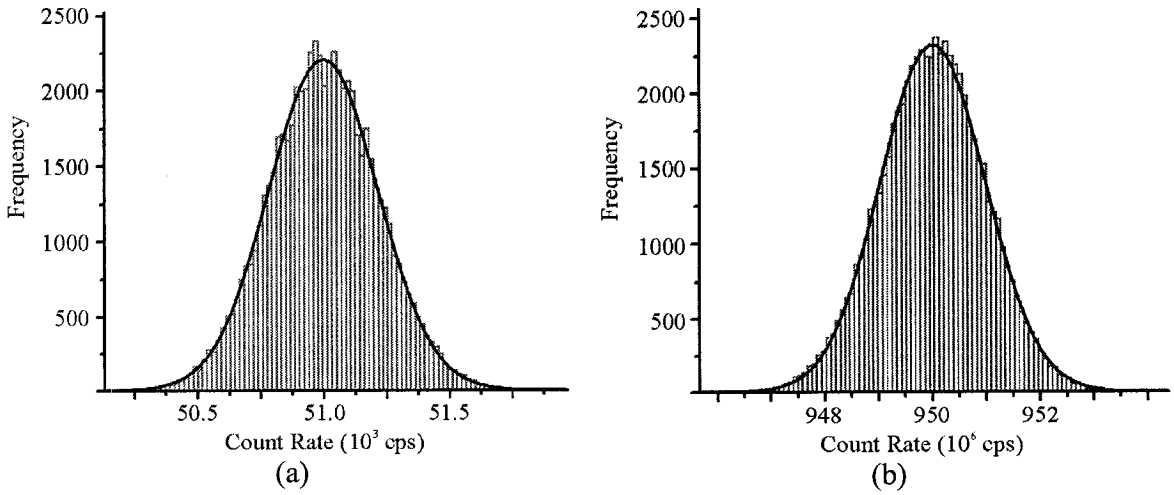

Figure 3-11. Distribution of count rates during simulated experiment (red) as well as Gaussian fit (black). The vertical axis represents the frequency (or population) of each of the 80 bins. (a) Ultraviolet channel – the mean count rate is 51,014 cps and σ = 223 +/- 2 cps. (b) Blue channel – the mean count rate is 949,550 cps and σ = 971 +/- 6 cps.

3.4 Summary

In conclusion, we have developed a Scanning Near-Field Optical Microscope which operates at two wavelengths, 442 nanometers and 325 nanometers, simultaneously. Our optimized tip preparation, based on etching the fibers through their protective jacket, routinely produces narrow aperture probes (below 100 nanometers) with large taper angles (greater than 15°). An evaporator was built to coat the fiber probes with 100 nanometers of aluminum at rates of greater than 50 nm/sec. Our SNOM uses a quartz tuning fork as a detector for shear-force interactions between the tip and the sample. The instrument has a vertical resolution of 0.095 nanometers and the optical detection is shot noise limited to the statistics of the laser source.

Chapter 4

Experimental Results

As the microscope design progressed and the fabrication of probe tips was optimized, we were able to calibrate the instrument and acquire dual-wavelength images. We patterned a calibration sample which was used to quantify our shear-force response and evaluate the performance of our aperture probes. We demonstrated the potential of the instrument by imaging wood cell samples.

4.1 Instrument Resolution

The very purpose of venturing into the near-field is to maximize the resolution of the instrument. Although the notion of resolution is not straightforward (see section 2.2), we are tasked with demonstrating the ability of the microscope to probe beyond the diffraction limit of conventional optics.

A calibration sample based on micropatterned polymer microspheres was developed that accurately and precisely reveals the ultimate limits of our microscope, both in the optical and the topographical image channels. The effort in developing our own calibration standard was necessary in that few alternate methods are available for producing sub-wavelength features and fewer still can create these on a glass substrate. Photolithography methods, for example, are well developed yet have yielded such narrow linewidths only in Extreme UV experiments on silicon. An effort, in conjunction with the Université de Sherbrooke to use electron beam methods to produce a suitable test pattern of chromium on glass was unsuccessful. Neither the thickness nor the shape of the islands was consistent enough to produce a suitable standard. Advanced e-beam

techniques can generate 10 nm features, however, the few machines of this caliber are not easily available to independent researchers. In addition, little success has been shown in generating these patterns on glass substrates as was needed for this work. A more simple solution was necessary in order to have the flexibility of different substrates and feature sizes. By using a self-assembly process, large areas (up to 1 cm^2) were covered with nanometer level features, eliminating the waste of time (and tips) in searching for a particular sample location. Such coverage would have been prohibitive with a lithography-based method.

4.1.1 Calibration Sample

The calibration standard perfected consists of a regular array of sub-micron sized metal triangles deposited on a glass coverslip (see Figure 4-1a).

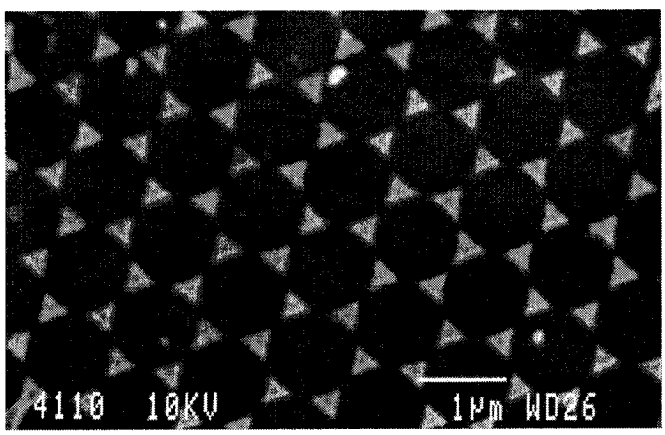

(a)

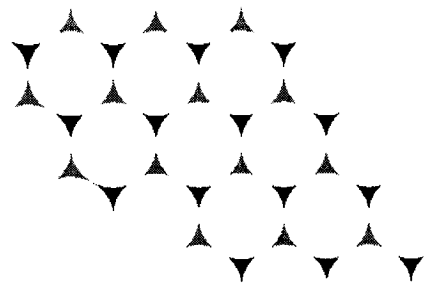

(b)

Figure 4-1. (a) SEM image of calibration sample. The spheres used here were 1 micron in diameter and the islands are a 50 nanometer thick film of aluminum. (b) Two symmetries arise in the pattern of triangular islands. All black triangles are equivalent as are all blue ones.

The calibration sample was prepared starting from an aqueous suspension of polystyrene latex microspheres. Piezo calibration is best done using standards of size comparable to those encountered during sample investigations and so four distinct size microspheres were used in order to address the range of scan sizes as well as to refine the procedure

(smaller arrays require increased deftness to prevent clumping of spheres). Microspheres of diameter 1.07 μm, 0.54 μm, 0.30 μm, and 0.25 μm were used (Polysciences Inc. catalog numbers 07310, 07307, 07306 and 07304 respectively), each suspension having a size variability with a standard deviation of 0.02 μm.

The general concept is simple: deposit the microspheres as a close-packed monolayer on a glass coverslip (transparent substrate required for transmission-mode SNOM) then coat the layer with a thin film of metal. The metal will cover the latex as well as the triangular crevasses where three spheres meet (see figure 4-2). Once the polystyrene is dissolved, a regular array consisting of triangular metal islands remains on the coverslip[107,108].

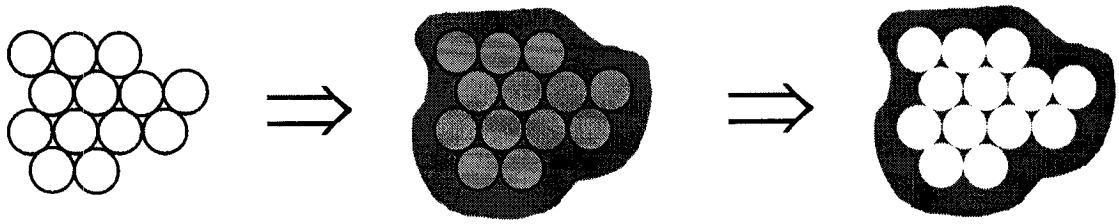

Figure 4-2. Calibration sample preparation. (a) A close-packed monolayer of polystyrene microspheres is deposited on a glass coverslip. (b) A metal film is deposited, coating the spheres as well as the spaces between them. (c) Once the latex is dissolved, bare glass is present on the areas covered by the spheres whereas a thin metal film remains where the spheres intersected, forming a regular array of triangular islands.

The implementation of this concept turned out not to be so simple. The first step in creating the calibration sample was to properly clean the glass coverslips. This is not only crucial for the formation of the monolayer but is essential to the proper dissolving of the microspheres (more on this later). Out of the box, commercial glass coverslips are not only dirty and dusty but are also coated with a thin layer of hydrophobic colloid to prevent them from sticking together in the package. The size and thickness requirements for the sample substrate made conventional coverslips the only commercially available solution. Had other alternatives existed, the same cleaning procedure would have been necessary to remove organics and dust accumulated from the air. The coverslips can be cleaned using "piranha solution", a 3:1 mixture of H_2SO_4 and H_2O_2 but since this tends to react violently with contaminants on the coverslips, we opted for an equally effective,

and slightly less explosive alternative. The glass coverslips were deposited into a 1:1 solution of ethanol and chloroform. The solution was brought to a slow boil then placed in an ultrasonic cleaner for 15 minutes. The coverslips were then removed, rinsed in ethanol and the process was repeated, using a fresh solution of ethanol and chloroform. After the second rinsing, the coverslips were dried with dry nitrogen and stored in a clean, dry container.

A drop of microsphere suspension deposited onto a hydrophilic substrate, like a clean glass coverslip, will result, once the water evaporates, in a randomly organized multilayer pattern. Several methods were investigated in order to produce large areas on the coverslips where the spheres would be arranged in a close-packed monolayer. These methods included spin coating[109], Langmuir-Blodgett (LB) through transfer[110,111], and inclined-substrate drying[108,112]. Each of these worked with varying degrees of success. The spin coating resulted in almost exclusive monolayer coverings; however, only very small clusters (under 50 spheres) were close-packed. The LB through transfer produced large close-packed areas; however, much of these were multi-layered and the method is serial and rather slow. Our best results were obtained using a simple method where the glass substrate is inclined during evaporation of the water (see figure 4-3).

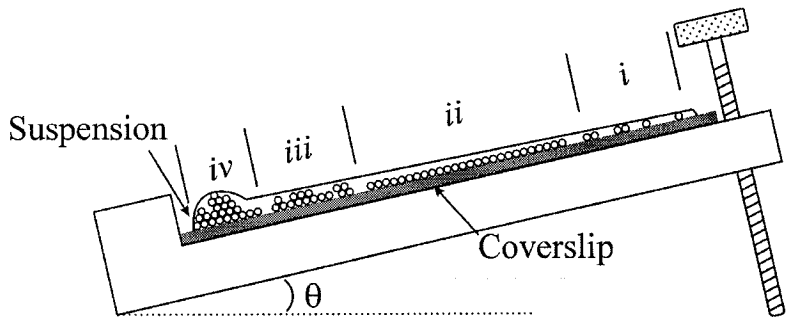

Figure 4-3. Drying stage used to prepare the close-packed microsphere calibration sample.

The stage is inclined at an angle of $\theta \approx 10^{\circ}$ and a few drops of the microsphere suspension are deposited along the top edge of a glass coverslip. The water is left to evaporate overnight, resulting in the arrangement of the microspheres into four distinct zones. Zone *(i)* consists of sparsely distributed small clusters of close-packed monolayered spheres.

Zone *(ii)* consists of large expanses of polycrystalline close-packed monolayered spheres and is most suitable for calibration use. Zones *(iii)* and *(iv)* consist of bilayered and multilayered, respectively, regions of close-packed spheres.

We found that neither the concentration of the polystyrene suspension nor the volume of the drop used influenced the formation of the close-packed domains to any great extent. Microsphere concentrations of 2% to 0.02% by volume were used, with a slightly larger region of monolayered domains achieved using 0.1% concentrations. Drop sizes of 2μl to 10μl were used, varying only the size of the multilayered rim around the bottom of the coverslip. Most important, however, was the proper cleaning of the coverslip and its angle of inclination during drying. Improperly cleaned coverslips feature the remains of the colloid layer which act as nucleation sites where domains begin to form before the microspheres have settled. These samples mostly exhibit regions containing multilayered domains. The angle of inclination was also found to be crucial. Only angles from 10° to 15° were successful in producing large regions of monolayered domains (see figure 4-4).

Care should be taken to use only recent shipments of the polystyrene solution. After only a few months, these age considerably and no longer produce well-characterized sample standards. An SEM picture of a close-packed monolayer of 18 month old 1 micron beads is shown in figure 4-4c. The spheres have begun to degrade and this appears as a furriness visible on the entire surface of the spheres. A consequence is that the beads no longer pack as hard spheres, with triangular spacings between them, but rather these compress together like sponges, leaving little space if any between them.

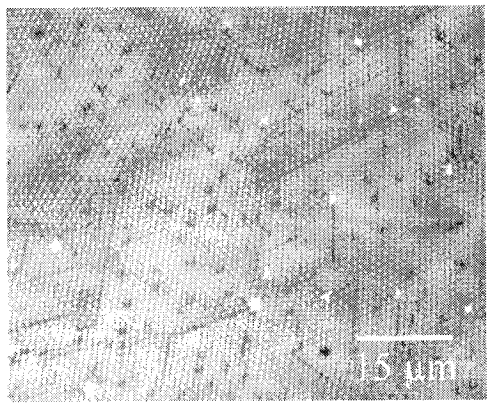

(a)

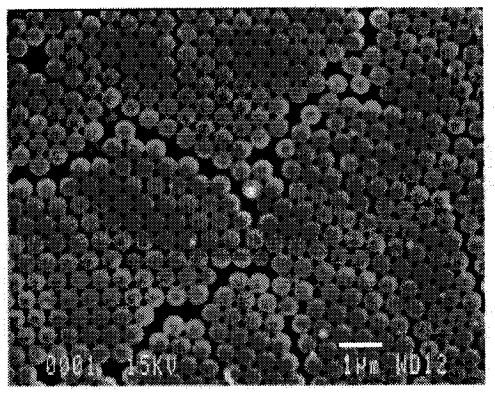

(b)

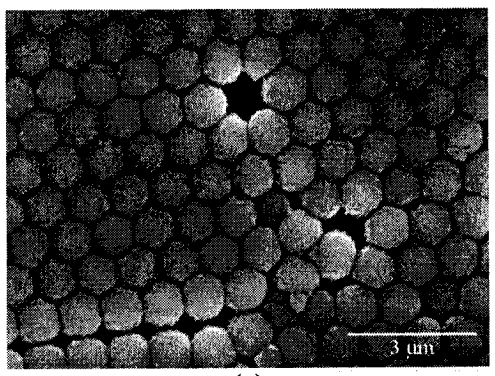

(c)

Figure 4-4. Close-packed monolayer of polystyrene microspheres. (a) Optical microscope image of polycrystalline arrangement prevalent in zone *(ii)*. The spheres here are 1 micron in diameter. (b) SEM close-up showing hexagonal symmetry in 540 nanometer diameter spheres sample. (c) Polystyrene sphere solutions degrade with time to where the spheres no longer resist compression.

Once the close-packed monolayer is assembled, a thin film, typically 20 to 50 nanometers, of aluminum is evaporated onto the coverslip. The evaporation conditions are similar to those present during the coating of fiber probes. The aluminum coats the spheres as well as the triangular spaces between them. Evaporation is used rather than sputtering since the former is directional and results in sharp edges to the triangles. The spheres are then dissolved by sonication in toluene, leaving the metal islands in a regular pattern on the surface. Due to the lack of a cleanroom environment and the 24 hour period where the sphere are left to coalesce into the close-packed monolayer, some contamination of the surface was inevitable. This contamination was resistant to the dissolution in toluene and a 10 nanometer residue was left on parts of the sample even after sonication. The presence of the residue was detectable in all three SNOM data channels. More rigorous cleaning methods removed the residue at the expense of also removing the metallic islands.

4.1.2 Contrast Beyond λ/10

Dual-wavelength SNOM images of the calibration sample were acquired and used to calibrate the microscope scanner and investigate the probe shape. The two transmission channels share similar features and exhibit similar resolutions but also reveal different structures, linked to chemical differences in the sample (discussed in section 4.2). Cross-sections of the images are most revealing and most readily comparable. Unless otherwise specified, the SNOM images in this thesis were obtained in shear-force feedback mode at a scan rate of 0.1 Hz and are comprised of 256x256 data points. The following three images were acquired simultaneously[‡‡].

[‡‡] For the reader unaccustomed to analyzing AFM images, squinting one's eyes slightly can filter some of the fine structure of the images and highlight overall patterns.

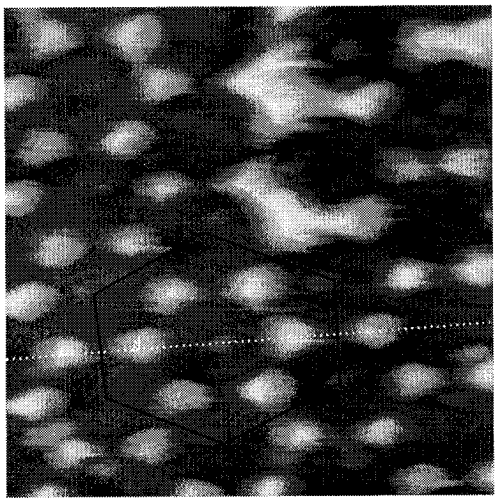
0μm
1.25 μm

(a)

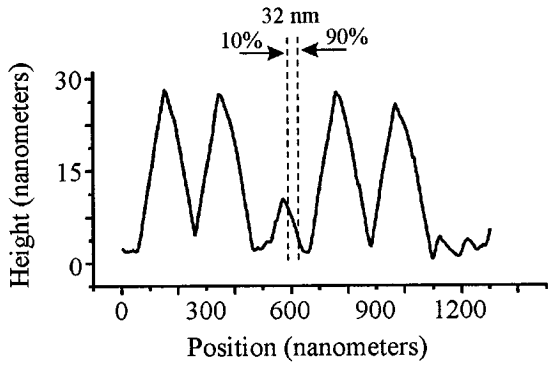
32 nm
10%
90%
Height (nanometers)
30
15
0
0
300
600
900
1200
Position (nanometers)

(b)

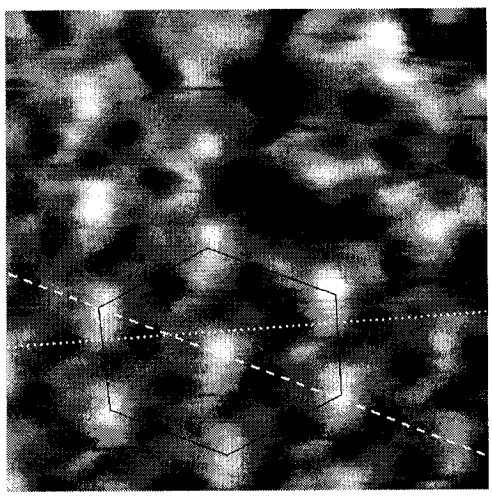
0μm
1.25 μm

(c)

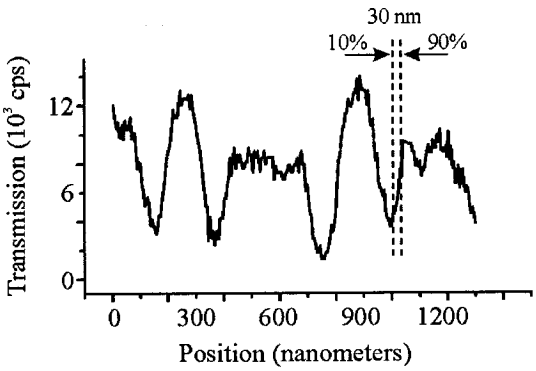
30 nm
10%
90%
Transmission (10^3 cps)
12
6
0
0
300
600
900
1200
Position (nanometers)

(d)

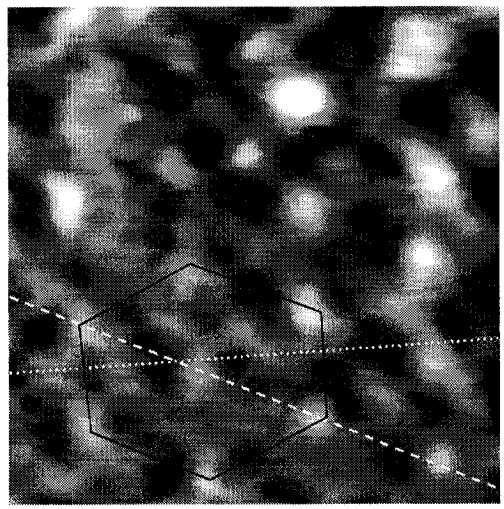

(e)

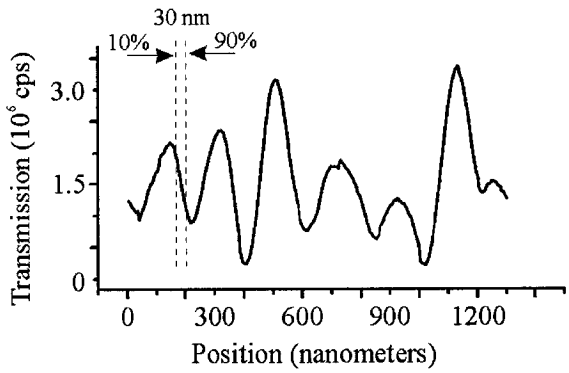

(f)

Figure 4-5. (a) Topography image of 300 nanometer calibration sample. The color scale spans 30 nanometers in height. The cross-section along the dotted white line is plotted in (b). The black hexagon highlights the symmetry present in the optical channel images. (c) Ultraviolet transmission image. The color scale spans 14,000 counts per second. The black hexagon highlights the symmetry of the transmission peaks. The cross-section along the dotted line (across the dark islands) is plotted in (d). (e) Blue wavelength transmission image. The color scale spans 3.5×10^6 counts per second. The black hexagon highlights the symmetry of the transmission peaks. The cross-section along the dotted line (across the dark islands) is plotted in (f).

The images in figure 4-5, like all SNOM images, are complex. Much of the rich detail is discussed below. The general features of figure 4-5a are readily identifiable with those of figure 4-1a. The bright triangular topography peaks are arranged in a hexagonal pattern, spaced by the diameter of the original polystyrene spheres. Similar to figure 4-6, the topography includes regions where the islands are connected. The regions not covered by the metallic islands are flat and absent of detail except for occasional much smaller features in the center of the islands. These are very significant to this work and are also discussed below.

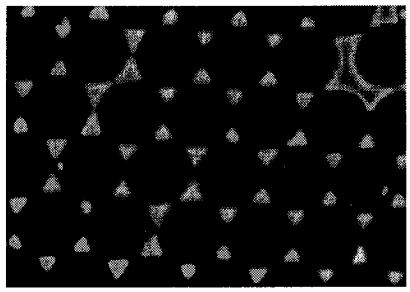

Figure 4-6. SEM image of the calibration sample studied in figure 4-5. Note that some of the aluminum islands are connected together due to alignment boundaries in the original polystyrene sphere monolayer.

The presence of aluminum on the glass substrate results in regions of low transmission, and so dark colors, in the two optical images, figure 4-5c and 4-5e. These dark islands preserve the spacing and symmetry found on the topography channel. The bare substrate at the center of these islands feature increased transmission exhibited by bright spots in the optical channel images. This absorption contrast pattern was precisely the goal of the effort in creating the calibration sample.

The credibility of these images in featuring true SNOM contrast is the first point of analysis. Referring to the criteria of section 2.7, we note that conditions *i*), *ii*) and most notably *iv*) for the presence of believable near-field contrast are fulfilled. Even a cursory comparison of the optical images, and certainly of the cross-sections in figure 4-5d and 4-5e, reveals distinct contrast for the two optical channels, satisfying point *iv*). The structure at the 600 nanometer mark on these cross-sections is flat in the UV but absorbs in the blue part of the spectrum. As we will see later, this contrast indicates the presence of distinct chemical species on the sample. The size and relative intensities of both the dark islands and the bright spots is also different, very noticeably so in the top center of the image where some of the metallic islands are connected.

Point *ii*) requires that the features be uncorrelated between the topography and optical channels. This can be shown to be the case using, for example, the black hexagon superimposed onto the images to highlight the data symmetry. In the case of the topography image, the corners of the hexagon lie on the flat portions of the sample. The

optical images, however, feature sharp peaks at these points. The peaks are restricted to the very centers of the metal island groups and so do not correspond merely to inverted contrast of the flat topography areas.

Finally, the first point requires that the resolution of the topography and optical channels be different. Resolution is discussed in detail below, however, each corresponding peak structure in the three image cross sections in figure 4-5 has a different aspect ratio. Higher aspect ratio features appear "sharper" as a measure of resolution. The distinct aspect ratios also contribute to point *ii*), the uncorrelation between images. The combination of these three credibility checks is as strong as possible evidence that cross-talk is absent in these images and that they represent true near-field contrast.

As mentioned before, the resolution of the three image channels is not straightforward to evaluate. The most common measure of resolution in the field of Scanning Probe Microscopy is to state that a feature's size is given as the lateral distance between 90% of its peak height and 10% of its peak height (see section 3.4). Other definitions may be used (this one is neither the most conservative nor the most generous) but we accept this definition as representing the relevant structure. As seen in section 2.2, attributing the notion of resolution to the near-field regime is awkward.

The resolution of the topography image was determined by taking five cross-sections, like the one in figure 4-5b across the island features, and measuring their sharpest 10-90% transition widths. The average value was 34 +/- 2 nanometers. The errors in the resolution figures are taken conservatively as the minimum and maximum of the cross-section resolution numbers. This is comparable to other SNOM studies. A higher resolution was obtained on other scans (see figure 4-8).

The most interesting element of this image is the presence of small features in the center of the islands, where the bottom of the polystyrene sphere originally rested on the glass coverslip. Given their location, they are residues left from incomplete dissolution of the polystyrene in the final preparation step of the calibration sample. The residue exhibited

different optical contrasts at the two optical channels and so demonstrated the chemical sensitivity of the SNOM (see section 4.2.1).

The hexagons featured in figures 4-5c and 4-5e are exactly the same one as in 4-5a and connects the centers of the bright transmission peaks where no aluminum is present. The resolution of the optical channels was obtained in a similar fashion to the topography. The cross-section along the metal islands of the ultraviolet channel shows the sharpest changes in transmission, with a resolution of 29 +/- 2 nanometers. This corresponds to almost $\lambda/11$. The resolution of the blue channel is very nearly the same at 31 +/- 2 nanometers – almost $\lambda/15$. Note that the transmission in this channel is 250 times greater than in the ultraviolet. We note that the resolution in the two optical channels is essentially the same. This was a result of section 2.2.2 and is a consequence of true Near-Field contrast. Also considered in the modeling section was the fact that although Near-Field resolution is wavelength *in*dependent, optical *contrast*, however, does rely on the wavelength. Appropriately, the two optical channels here and in subsequent figures of this work feature distinctive contrast. The 30 nanometers of aluminum on the islands correspond to more than four decay lengths and accordingly, the transmission minima in the cross-sections are very nearly zero. The increased intensity on the blue channel results in less statistical noise and a smoother curve than the ultraviolet image. The optical resolution of our instrument is very good as compared to other transmission mode SNOMs. Higher lateral resolutions can be obtained at a cost of increasing technical difficulty in manufacturing smaller aperture probes. A practical limit exists, however, in that the finite skin depth of the aluminum coating (see figure 2-2) establishes a minimum effective aperture size. Apertureless SNOM probes and emissive tips, such as those featuring fluorescent molecules, overcome this limit. Of course, these approaches feature their own set of limitations.

An alternative take on the spatial resolution of the instrument, based on a signal processing approach (see section 2.1), is to define resolution as the spatial frequency at which the image modulation falls to one-half its maximum value[113]. Such an analysis

was performed on the cross-section of figure 4-5d and 4-5f (see figure 4-7). The results are a 3 dB point at 0.031 +/- 0.002 nm^{-1} for the ultraviolet channel and at 0.033 +/- 0.002 nm^{-1} for the blue channel. This corresponds to a spatial resolution of 32 +/- 2 nm and 30 +/- 2 nm, respectively, in good agreement with the SNOM standard of 10-90% transmission widths.

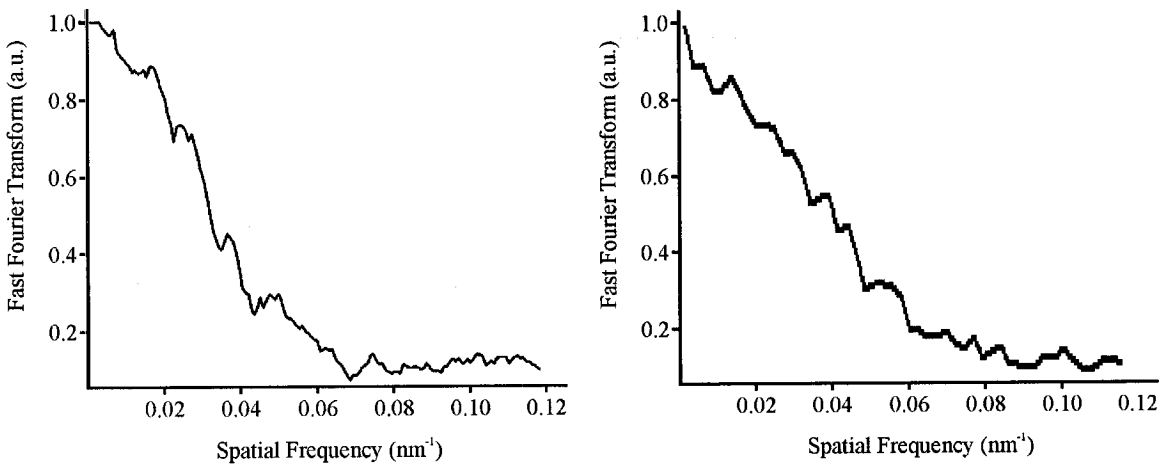

Figure 4-7. (a) FFT of cross-section of Figure 4-5d (ultraviolet channel). (b) FFT of cross-section of Figure 4-5f (blue channel).

As expected, both optical channels exhibit the same resolutions, a consequence of true near-field contrast. Though the resolutions are similar for the optical and topography channels in this example, the following case demonstrates the independence of the topography contrast.

In order to investigate the transmission differences between the two optical wavelengths, another calibration sample was made where only 5 nanometers of aluminum was deposited. The thinner coating calibration samples are more difficult to make, however, as the thin aluminum film peels off during the dissolving of the microspheres in an ultrasonic bath. Simply rinsing off the spheres (without the ultrasonic bath) leaves some polystyrene residue on the sample. A dual wavelength SNOM image of this sample is presented in figure 4-8.

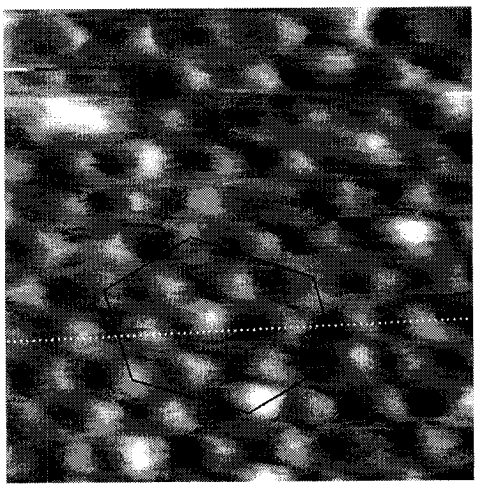
0μm
1.25 μm

(a)

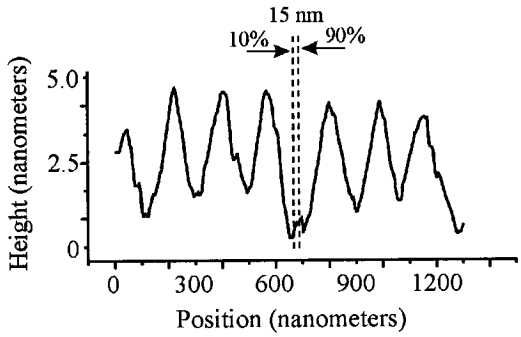
15 nm
10%
90%
Height (nanometers)
5.0
2.5
0
0
300
600
900
1200
Position (nanometers)

(b)

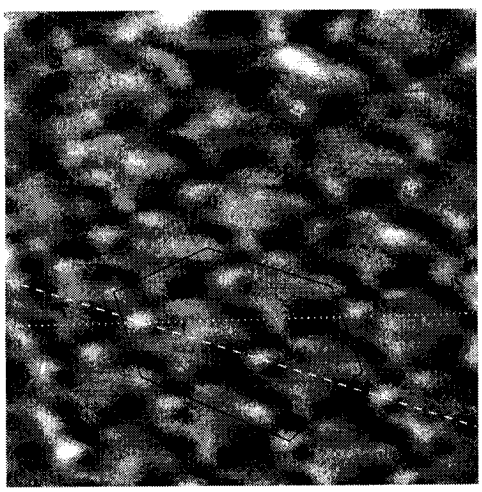
0μm
1.25 μm

(c)

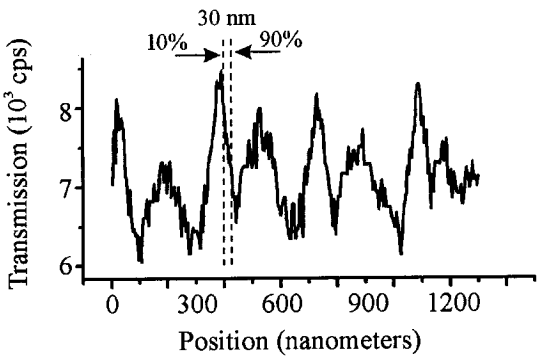
30 nm
10%
90%
Transmission (10³ cps)
8
7
6
0
300
600
900
1200
Position (nanometers)

(d)

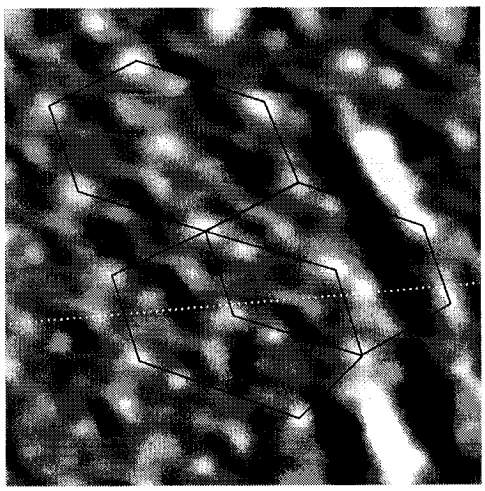

(e)

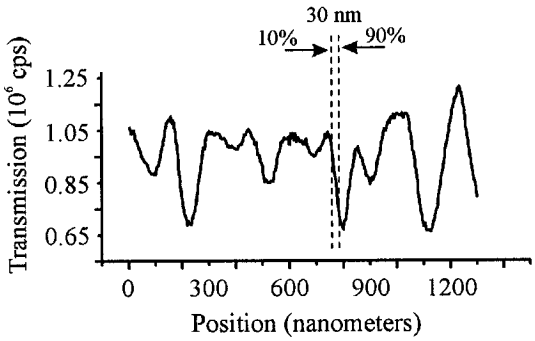

(f)

Figure 4-8. (a) Topography image of 300 nanometer calibration sample coated with only 5 nanometers of aluminum. The color scale spans 5 nanometers in height. The cross-section along the dotted white line is plotted in (b). The black hexagon highlights the symmetry present in the optical channels. (c) Ultraviolet transmission image. The color scale spans 12,000 counts per second. The black hexagon highlights the symmetry of the transmission peaks. The cross-section along the dotted line (across the dark islands) is plotted in (d). (e) Blue wavelength transmission image. The color scale spans $1.2x10^6$ counts per second. Additional hexagons are present to make up for increased complexity in this image. The cross-section along the dotted line (across the dark islands) is plotted in (f).

Again, due to the differing contrast between the two optical channels, we are assured of true SNOM contrast. The topography image, figure 4-8a, shows the island patterns with both symmetries of triangles (see figure 4-1) and a resolution of 15 +/- 1 nanometers. This resolution is very good for SNOM and compares favorably with AFM. As mentioned before, this sample was more difficult to prepare – polystyrene residue is present in almost all island centers, some of which is greater in height than the islands themselves. Soft polymers are known to be difficult to image in shear-force[114,115]. The vertical resolution demonstrated here is equally impressive. The central feature in figure 4-8b where the spatial resolution was determined has a height of 0.45 +/- 0.08 nm, corresponding to molecular-level sensitivity of polystyrene monomers.

The optical channels exhibit spatial resolutions equivalent to those in figure 4-5. The features in both optical channels are as expected, increased transmission in the island centers and dark elements at the islands themselves. One interesting result is that not all dark islands are visible – contrast in the blue transmission channel being especially complex.

4.2 Chemical Contrast at 30 nanometers

4.2.1 Calibration Sample

The polystyrene sphere sample highlights advantages of using two contrasting wavelengths simultaneously in that high resolution chemical information about the sample can be determined (see figure 4-9).

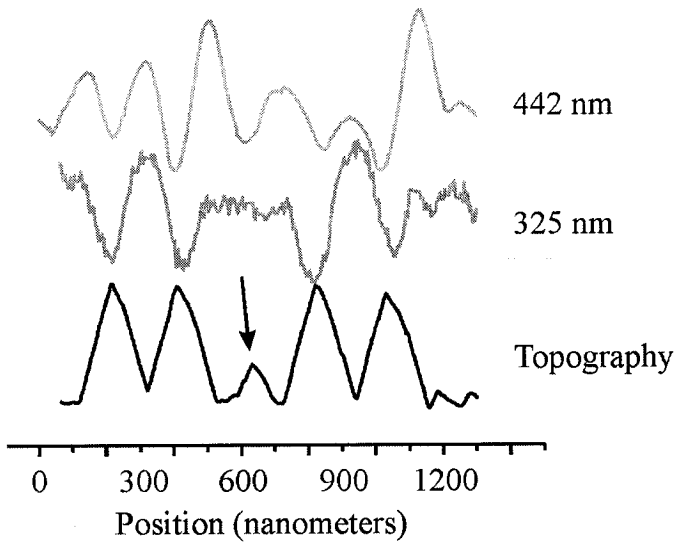

Figure 4-9. Cross-sections of figure 4-5 (taken along aluminum islands). The transmission troughs of both wavelength channels correspond to the location of aluminum islands on the sample. The arrow highlights the presence of polystyrene residue in the topography channel. A corresponding signature can be seen in the behavior of the optical channels.

The topographical peak in the center of the cross-section (highlighted by the arrow) has a different transmission value in the two optical channels. The decrease in transmission in the blue wavelength and the corresponding (relative) transparency in the ultraviolet agree qualitatively with spectroscopic studies of polystyrene[116] in that different absorption coefficients for the two wavelengths have been observed. Those analyses were performed on latex solutions, rather than a solid layer, limiting our comparison to a qualitative one. Nevertheless, the comparison of both SNOM wavelength channels demonstrates that *chemical contrast with 30 nanometer resolution* is possible using our microscope. The simultaneous acquisition of two wavelength transmission profiles enables a very high lateral resolution spectroscopic analysis of the sample.

A similar chemical analysis can be made on the sample featured in figure 4-8, where a 5 nm layer of aluminum was used in the preparation of a calibration sample. The decay lengths of 325 and 442 nanometer light in aluminum are approximately 7.5 and 8.75 nanometers respectively (see figure 2-2) which should allow some light to transmit through the metal islands at both wavelengths. In practice, if one knew the thickness of the sample, a determination of the decay lengths of the two channels would reveal its chemical nature.

The cross-section along the dark islands in the ultraviolet channel (see figure 4-8d) shows the decreased transmission at the islands where the count rate decreases to a minimum of about 6000 cps. This agrees well with the rate expected due to the exponential decrease in intensity through the 5 nanometers of aluminum, $I_{UV_{MIN}} = (12x10^3\,\text{cps})e^{-5\text{nm}/7.5\text{nm}} \approx 6150\,\text{cps}$ [§§]. Similarly, the blue transmission channel (figure 4-8f) shows a minimum count rate of about 65,000 cps, in good agreement with the rate expected from $I_{Blue_{MIN}} = (1.2x10^6\,\text{cps})e^{-5\text{nm}/8.75\text{nm}} \approx 67{,}800\,\text{cps}$. This confirms the presence of aluminum at these locations.

[§§] The maximum values used in these calculations are taken from the entire image, not the figure cross-sections.

Keeping with this model of absorption, we may determine the microscope's detection limit of chemical species in the sample. Once calibrated for a particular substance, the decay length τ serves as a measure of thickness or equivalently, concentration. Given that $\frac{dI}{dZ} = \left(I_0 e^{\frac{Z}{\tau}} \right) \cdot \frac{-1}{\tau}$, we may determine the concentration from $\tau = I \cdot \frac{\Delta Z}{\Delta I} = \sqrt{I} \cdot \Delta Z = SNR \cdot \Delta Z$, where ΔZ = 0.095 nanometers is the uncertainty on the height measurement and ΔI is the noise on the optical channel, which varies as $\sqrt{I}$. We see then that the chemical concentration detection limit becomes a signal-to-noise contrast issue. We may approximate the minimum detection limit as $\frac{\tau_{\text{minimum}}}{\tau_{\text{typical}}} = \sqrt{\frac{I_{\text{minimum}}}{I_{\text{typical}}}} = \sqrt{\frac{1000\,cps}{100{,}000\,cps}} \approx 3\%$. This process may also be inverted so that by extracting the decay lengths from the SNOM images, one may cross-reference these to absorption profiles of various substances and perform chemical identification with a lateral resolution of 30 nanometers. Since the light transmitted through the sample decays exponentially due to the near-field effect *and* the effect of absorption, the product of two exponentials means that we are also probing a very small volume of the surface chemistry. Compared to far-field investigations, the SNOM can probe approximately a 3000 times smaller volume of the sample (10x10x30 nm^3 – HWD). Finally, using two wavelengths simultaneously serves to more accurately determine the chemical species since two sets of decay lengths may be compared. Simultaneity is the key since serial scans of the sample are not performed under the same critical boundary conditions and so do not enable direct comparison of near-field images.

4.2.2 Wood Cells

A chemically heterogeneous real-world sample was chosen for this work in order to demonstrate the potential of the instrument to a pertinent research problem. Black Spruce wood cell sections were chosen as particularly relevant due to their long lifetime, their high optical transmission and chemically-selective UV contrast, and local expertise (in

conjunction with the on-campus branch of the Pulp and Paper Research Institute of Canada) in sample preparation. The heart of Canada's pulp and paper industry is in converting raw materials, mainly wood, into a slurry of fibers which can then be processed into the desired finished product. Typical softwood fibers are 30 μm wide and 3.5 mm long cells made up of 40-45% cellulose, a linear polymer of glucose, about 30% lignin, a complex cross-linked polymer, and a host of other carbohydrate polymers and extractives[117]. The flexible cells are tightly bonded together by a lignin network between the cells (see figure 4-10). A further description of the nature of wood is presented in Appendix A.2. Lignin removal, in order to isolate the individual wood fibers, is a major concern of the pulping industry. Lignin is also responsible for some of the ageing characteristics of paper, such as yellowing.

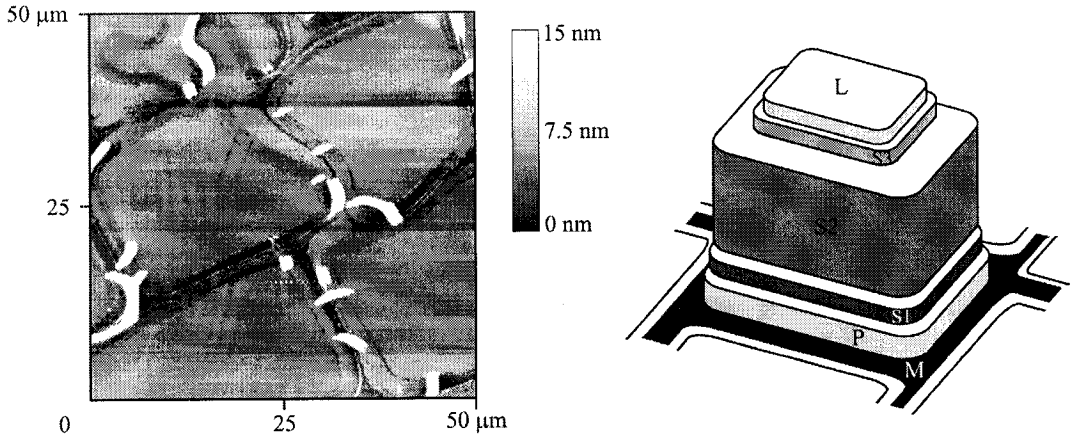

Figure 4-10. Wood cells arrange themselves into close-packed arrays. (a) AFM image of 80 nanometer thick transverse section of Black Spruce wood cells. The bright bands observed in the wood cell sections are a result of the sectioning process where ridges form due to shear pressure on the thin sections. This effect has been referred to as "butter curls" and has been observed in other studies[118]. (b) Diagram of cell components for softwood fiber (see text for details). (Diagram adapted from *Handbook for Pulp & Paper Technologists*, by G. A. Smook, 2nd ed., Angus Wilde Publications 1992)

Dual-Wavelength SNOM, where one wavelength is in the UV, is tailor-made for high resolution studies of lignin, due to its high resolution and chemical sensitivity – lignin absorbs strongly in the ultraviolet and is the only component of the cell to do so. Lignin is mostly present in the cell at the cell walls and middle lamella regions. Wood sections

for our SNOM studies were selected as 80 nanometer thick ultramicrotomed Black Spruce cells. The sectioning process involves taking a trunk sample about 5 centimeters long and embedding the cells in resin. Nanoplast® resin (a hydrophilic melamine/formaldehyde solution used in electron microscopy) works best when creating such thin slices. The role of the resin is to fill in the voids, primarily the lumen, of the cells so that sectioning will not crush them. The coverslip in our study contained eight ultramicrotomed slices, each featuring about two dozen cells.

A dual-wavelength SNOM study of the wood cell sections reveals rich details (see figure 4-11).

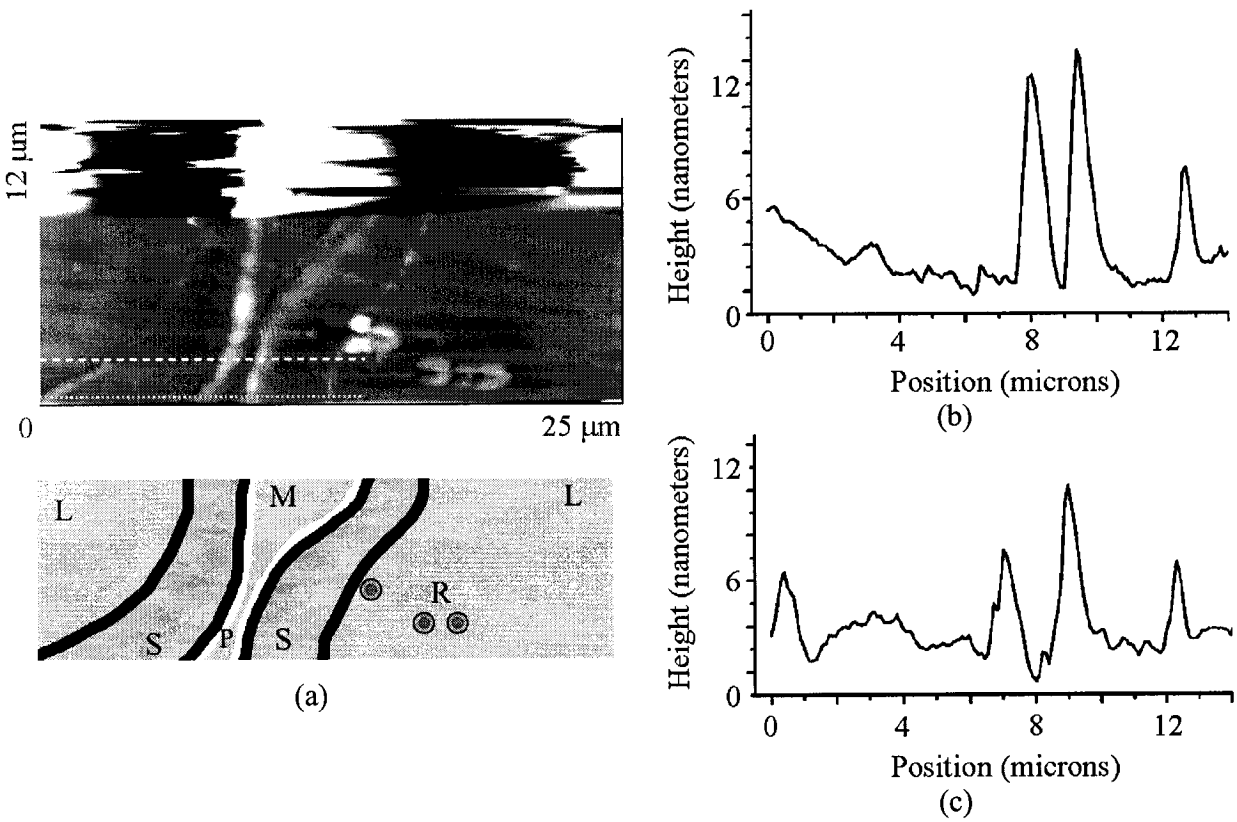

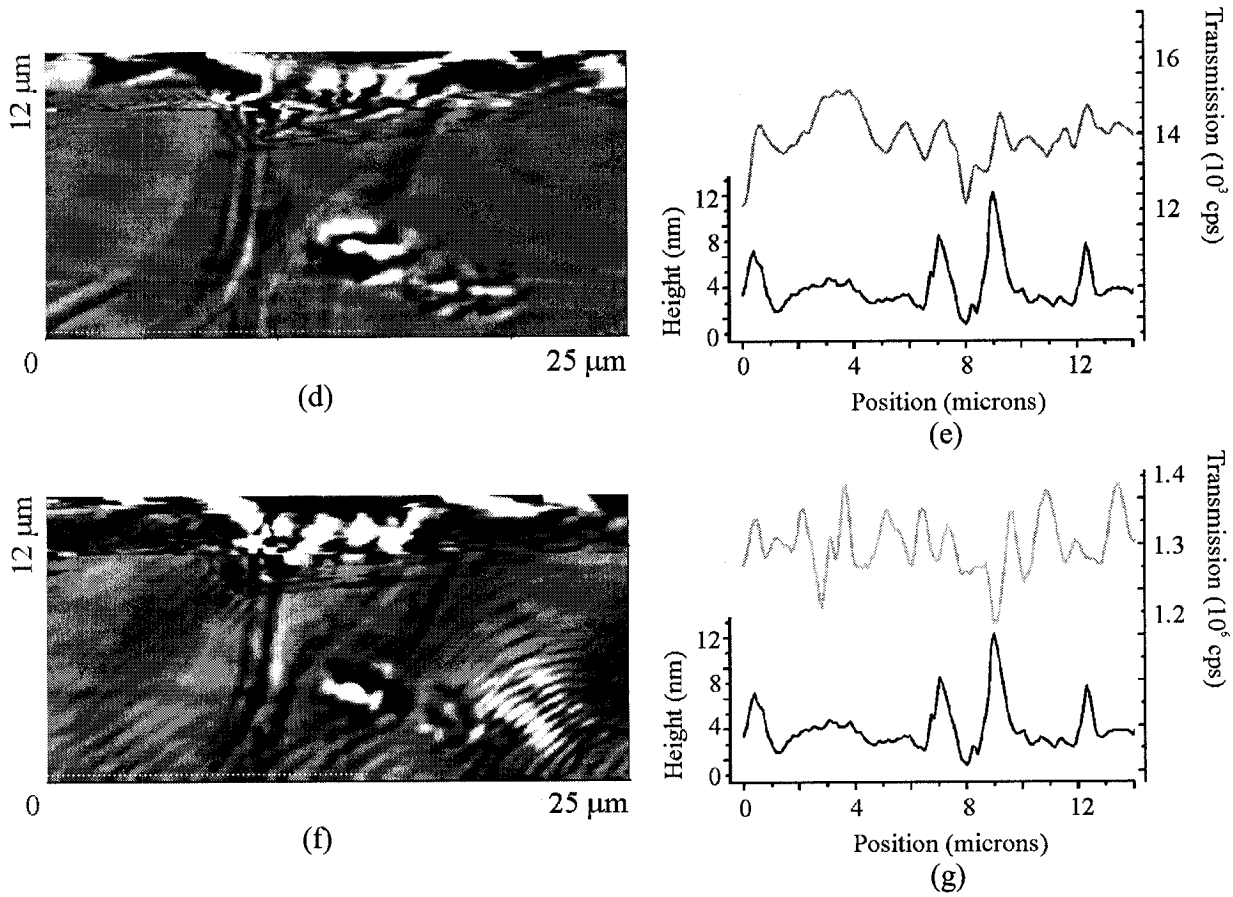

Figure 4-11. (a) Topography image of SNOM scan of transverse cross-section of wood cells. The color scale spans 14 nanometers in height. The insert below the image is included as a guide to help the reader identify the lumen (L), secondary (S) and primary (P) walls, the middle lamella (M) and the residue globules (R). The cross-section along the dotted line appears in (b). The cross-section along the dashed line appears in (c). (d) Ultraviolet transmission image. The color scale spans from 10,000 to 20,000 cps. The cross-section along the dotted line appears in (e) along with the topography. (f) Blue transmission image. The color scale spans from 1.0×10^6 to 1.6×10^6 cps. The cross-section along the dotted line appears in (g) along with the topography.

The top portion of the topography image is distorted due to a loss of shear-force feedback. This can occur when imaging soft samples and is most likely due to the tip either picking up or dragging along a particle on the sample surface or even a small piece of the sample itself.

These images present two adjoining wood cells. We recognize, from left to right, the flat lumen region, the inner cell wall, the outer wall and middle lamella, then the outer wall of

the next cell, its inner wall and lumen. The cross sections of the topography channel reveal swelling at both sets of cell walls and a middle lamella region unaffected by swelling (this swelling of the carbohydrate-rich structures, especially the secondary wall, has been previously observed[119-121]). The top cross-section, which extends further into the center of the cells, reveals that the lumen region slopes gently downwards to the cell wall. Two round features in the right cell were determined to be resin globules in an analysis in figure 4-13 below.

The ultraviolet image clearly shows the cell wall features of both cells as well as intricate patterns around the resin globules. The transmission cross-section begins at left with a sharp absorption corresponding to the start of the secondary cell wall. The increased transmission through the rest of this structure is most likely due to the decrease in density caused by swelling. The changes in transmission due to small variations in lignin concentration in the primary wall seem to be surpassed by the large changes due to swelling.

The cell features are also present in the blue image. The cell wall structure is visible in the blue channel. One would not expect cell walls to show contrast in the blue channel, however, those features correlate to the topography. One exception is that the middle lamella layer shows a transmission of about average intensity for the cross-section, whereas the surface dips considerably at this point. An interference pattern appears on this image which is discussed in more detail in another study (see figure 4-22).

The ratio of the two optical channels is presented in figure 4-12 and encapsulates the chemical contrast observed on this sample.

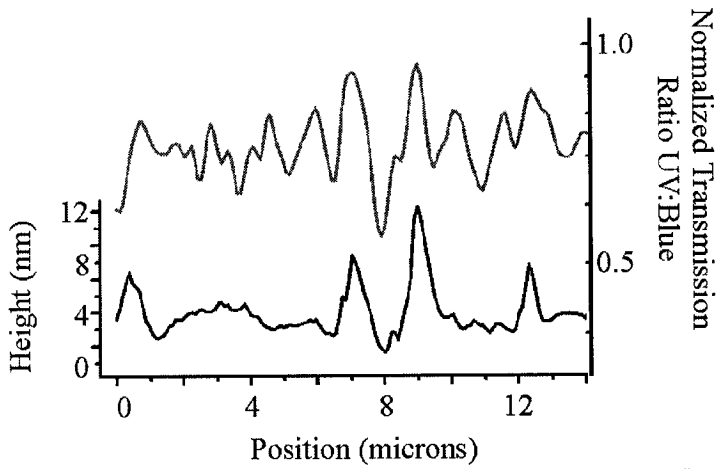

Figure 4-12. Normalized ratio of ultraviolet to blue transmission (red) together with the topography cross-section (black).

There is a significant contribution by the interference pattern in the blue wavelength. There is also a non-trivial effect due to topography. There is also, however, chemical contrast at the middle lamella region, at about the 8 micron position. Here, the ultraviolet signal decreases significantly while the blue transmission remains constant. A discussion of how to improve the contrast for wood cell samples is presented in the Conclusions and Outlook section of this work.

When imaging the supposedly flat lumen region, features were present which ranged in topography from very small bumps to quite large globules (see figure 4-13). The most interesting property of these features is that they exhibit different optical contrast at the two wavelengths. The location of these features suggests a compositional change in the embedding resin, most likely an impurity. Independent determination of the optical properties of the resin was not possible since these change during the curing process and are dependent on the embedding medium. This limits our analysis to a qualitative one.

A cell wall is visible at the top right of the topography image, placing the central blob in the lumen region of the cell, filled with the embedding resin. The blob is large but relatively featureless, as seen in the differentiated image in (b)[***]. To the left of the

[***] The differentiated image shows much detail not observable in the normal topography image due to the reduction of the large dynamic range of the z-scale.

central feature are seen more than a dozen smaller globules and two relatively large ones (black arrows). Each of these is also relatively flat. The optical channels reveal more.

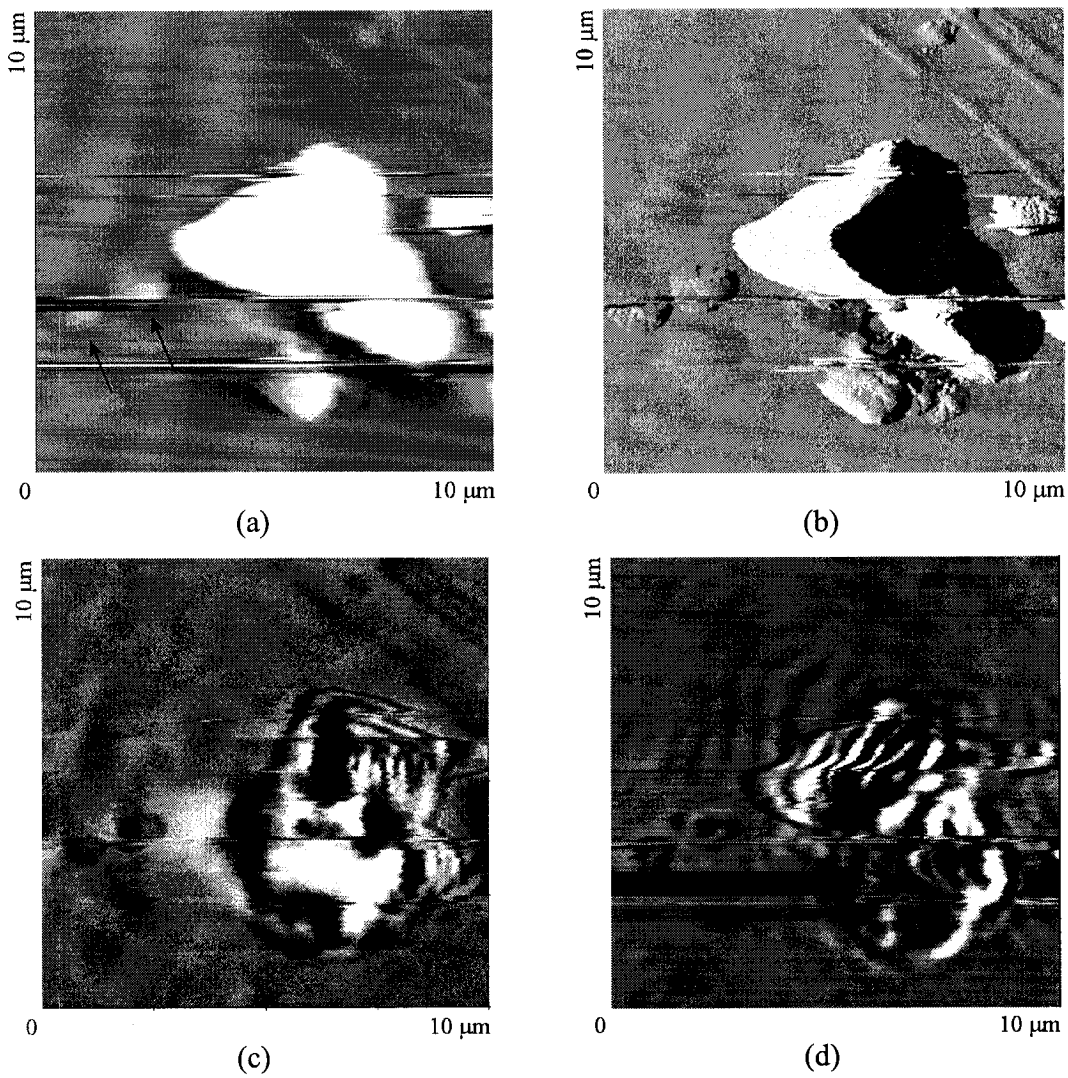

Figure 4-13. Dual-Wavelength SNOM image of transverse cross-section of wood cells. (a) Topography – the color scale spans 200 nanometers in height (b) Differentiated image of topography channel (c) Ultraviolet transmission – the color scale spans from 2,300 to 5,000 cps. (d) Blue Transmission – the color scale spans from 8,000 to 1.25×10^6 cps.

The ultraviolet image shows dark bands at the cell wall structure, indicating increased absorption as expected. The smaller globules are definitely visible in this wavelength as are the two larger ones. The central blob itself shows a great deal of structure, with portions transparent and opaque to ultraviolet light. The blue transmission channel also

shows a great deal of structure in the central blob but the features here are very much different than in the UV. This again highlights the complexity in interpreting SNOM optical contrast.

The two medium globules seem similar but the smaller ones show little contrast and so are not visible on this scale. Note also that the cell wall is all but invisible in this channel. Surface waves are also evident, only on the blue transmission channel though, and the source for these appears to be the central globule. Since the orientation of the wavefronts matches the outline of the central globule, light reflected from the globule and then scattered by the tip into the sample is the most likely candidate for this effect. The ultraviolet channel, featuring 250 times less intensity, exhibits much more subtle scattering.

4.3 SNOM Contrast and Image Cross-Talk

Dual-wavelength SNOM is a powerful tool to identify true SNOM contrast and to also investigate the complex optical images which result from near-field studies. It is best used in conjunction with other tools, such as autocorrelation and multiple-tip analysis, in studying SNOM images. This section continues the analysis of the calibration and wood cell samples and presents examples of the challenging interpretation of near-field studies.

Though collected together in this chapter, imaging artifacts and cross-talk are quite different effects and are different in origin. Artifacts, such as multiple-asperity tips, tip pinholes, and offsets between topographic and optical imaging centers are due to the great difficulty in making repeatable tips and imaging routinely under equal conditions. These inconsistencies could presumably be engineered away to result in perfectly repeatable scanning conditions. They highlight the need to perform simultaneous imaging of both optical channels, as in our instrument, as opposed to all other multi-wavelength instruments where optical images are acquired successively.

Image cross-talk, however, is an effect due to the physics of shear-force distance control and the sensitive dependence of the optical channels to tip-sample separation. Both of these behaviors are highly complex and intrinsic to the SNOM technique. Two optical channels are key to identifying the presence of cross-talk.

4.3.1 Calibration Sample

Given the highly non-trivial contrast present in the optical channels, we wish to compare them in a relevant manner, by observing their overall symmetry. For this we turn to autocorrelation analysis as a powerful tool in emphasizing translational symmetry in complex data (see figure 4-14). The algorithm used in this work measure the amount of overlap between two copies of an image offset by a 2D vector. This analysis has a number of advantages over simply taking a Fast Fourier Transform (FFT) of the image. Complex contrast may not reveal distinct FFT peaks since some of the symmetry is not highly periodic and all frequencies contribute to some degree (see figure 4-7). Also whereas autocorrelation analysis reveals how "well" each island feature overlaps with the others over the image, providing insight into the consistency of identical structures, this information is not easily extracted from an FFT analysis. In our application, the spatial autocorrelation function is a map of the probability of an image overlapping with itself as a function of displacement between the two copies.

The hexagonal symmetry is readily apparent in all autocorrelation maps. The overlap between the maps, figures 4-14d and 4-14h, is very good, demonstrating that the periodicity is the same for the three data channels and that the correlation remains significant even out at the edges of the image. Some fine structure is also present. In 4-14a, each correlation maxima, corresponding to an image shift of one microsphere diameter, has six smaller peaks surrounding it. These correspond to a weak auto-correlation along a displacement of one island spacing. The islands appear round instead of triangular, confirming the limited topographical resolution discussed in section 4.1.2. However, the effective "optical" tip shape, characterized by the resolution in the wavelength channels is independent of the shear-force interaction. In 4-14c fine structure

present in the optical channel data is revealed as elongations in the shape of the correlation maxima and in the presence of bands linking the various peaks.

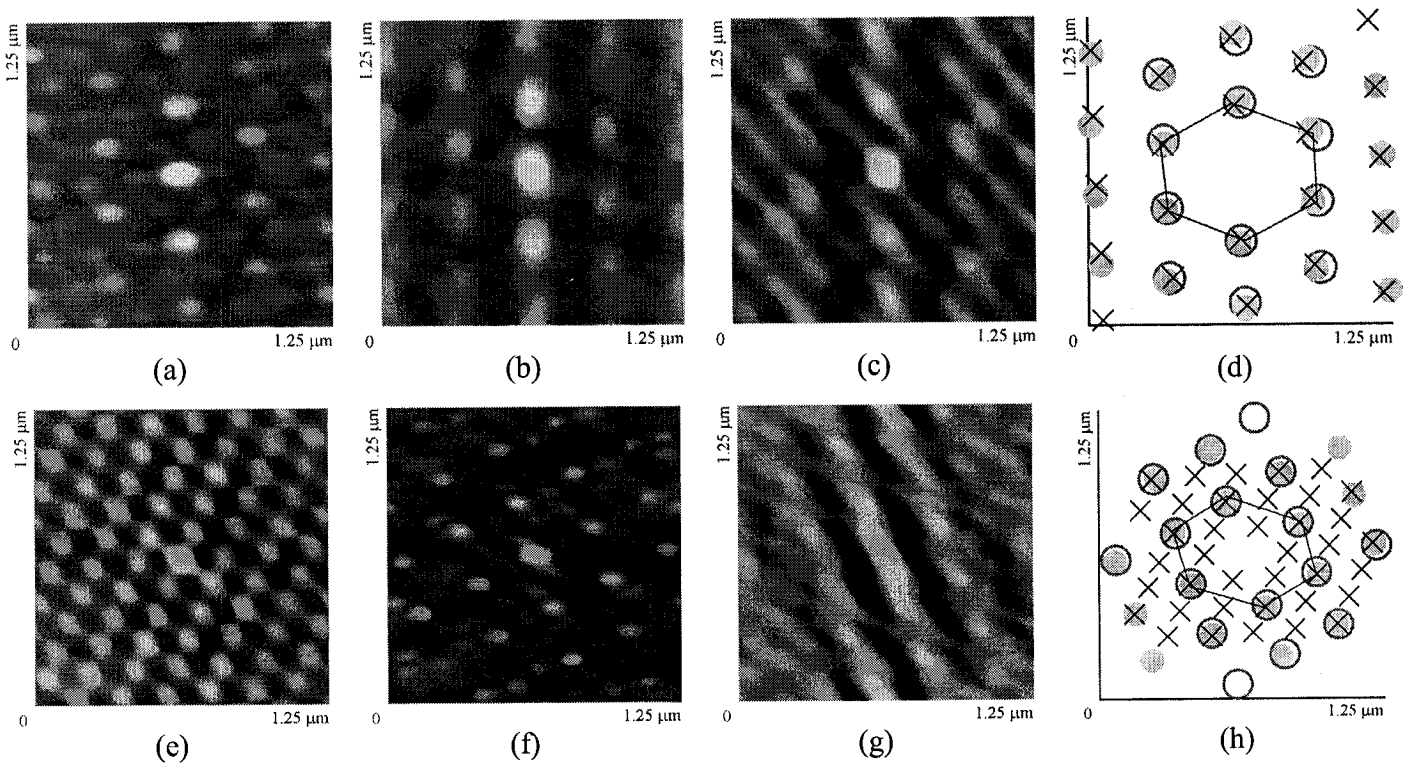

Figure 4-14. Autocorrelation maps of the topography (a), ultraviolet (b) and blue (c) transmission channels of figure 4-5. The positions of the overlap maxima from each image are compared in (d) where the black crosses, violet circles and blue circles represent the topography, ultraviolet and blue peaks respectively. The black hexagon is taken from figure 4-5 to highlight the appropriate length scales. A similar analysis is performed in (e) through (h) for figure 4-8. The central peak has been left out of the diagrams since it invariably shows a high autocorrelation value and so is redundant in this view.

In combination with more sophisticated tip-sample interaction models, advanced image reconstruction could potentially be used to extract the aperture shape from the SNOM images. Figure 4-14e looks much like a chessboard since the correlation is equally strong between an image shift over a microsphere diameter and one over the spacing between metal islands. The increased presence of residue in the island centers of this sample adds a degree of symmetry and makes for the very regular array of features observed. Sharp correlation peaks are present in (f), owing to the regularity of the ultraviolet channel

features, however, these are much less pronounced in (g), where the complexities of the contrast in figure 4-8e are present as broad peaks and short correlation lengths.

Due to the nature of the SNOM tip, that is the distinct topography and optical imaging elements, it is common for an offset to be present between the topography and optical images (see figure 2-18). Additionally, multiple asperities on the tip itself can result in multiple topography "ghost" features. Figure 4-15 exhibits both effects.

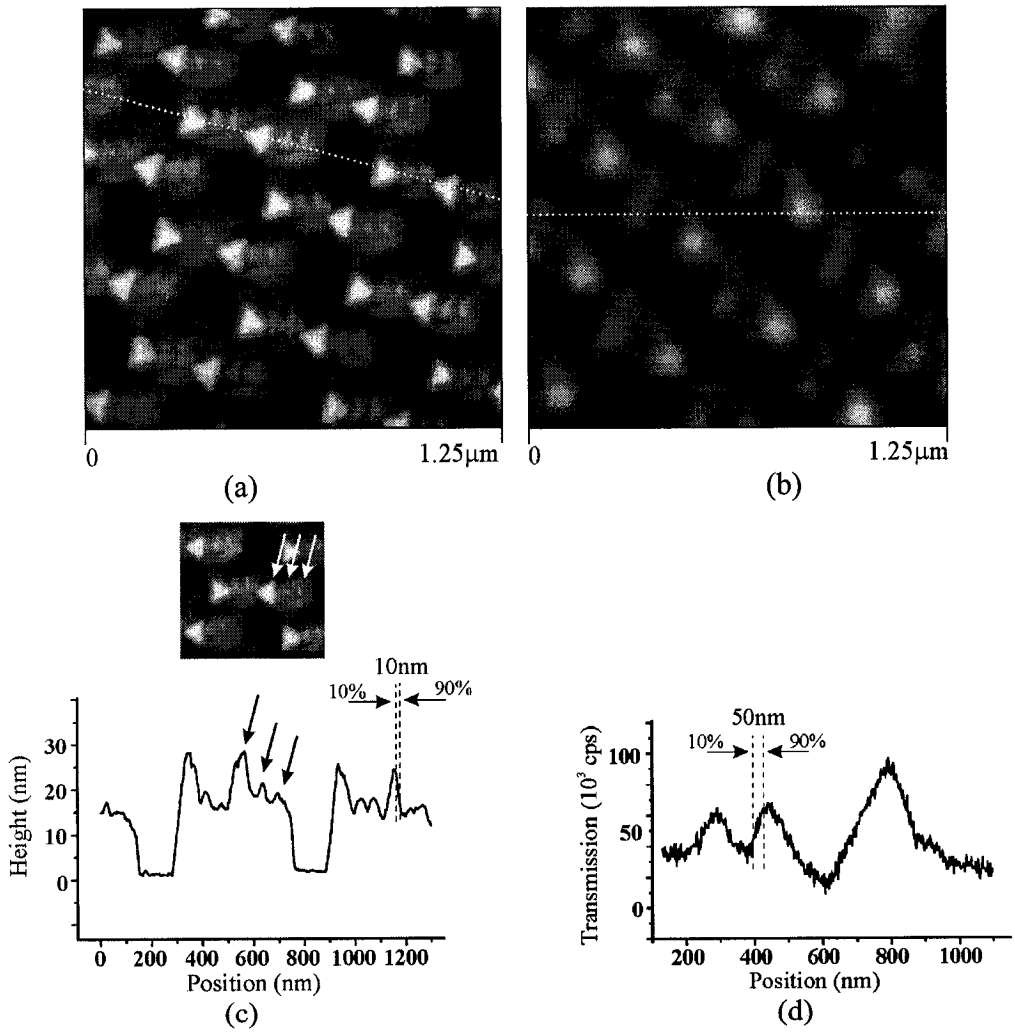

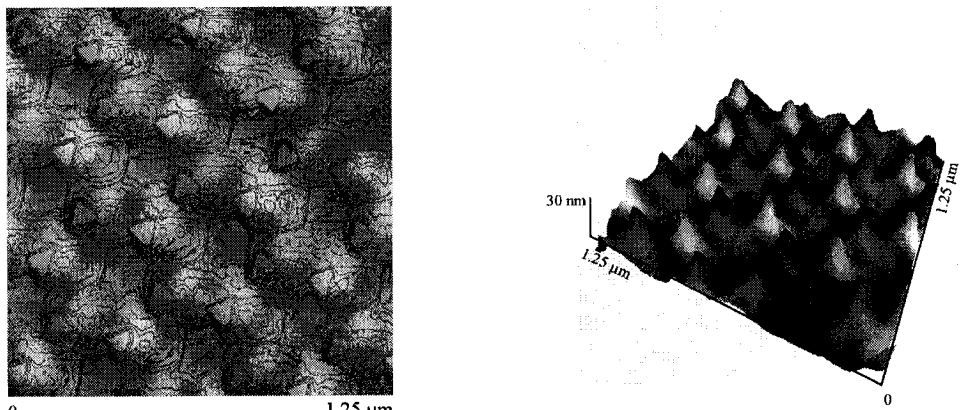

Figure 4-15. SNOM image of calibration sample using 300 nanometer beads and 30 nanometers of aluminum. (a) Topography channel. The color scale spans 30 nanometers in height. (b) Blue wavelength channel. The color scale spans 100,000 counts per second. (c) Topography cross-section along dotted line featuring inset showing multiple tip effect. (d) Transmission channel cross-section along dotted line. Two approaches at comparing the features from both channels. (e) Black lines representing a contour mapping of the topography channel are superimposed over the blue transmission channel. (f) A 3-dimensional overlay of the two channels – the topography in this image is taken from the topography channel whereas the color scheme is taken from the blue wavelength channel with lighter hues representing an increase in optical transmission.

The topography image in figure 4-15a presents the three-fold symmetry of the triangular islands – note that the two triangle orientations (see figure 4-1) are discernible. The optical transmission channel exhibits the hexagonal symmetry of the original polystyrene close-packed monolayer. The smallest topographical features measure 10 +/- 1 nanometers across, whereas the transmission channel exhibits a resolution of 50 +/- 2 nanometers. The different resolutions highlight the different imaging mechanisms. Looking closely at the triangular features in the topography channel, one can observe that each island seems duplicated twice again to the right, the result of multiple asperities on the probe tip.

The difference in symmetries is accentuated in figure 4-15e and 4-15f. In (e), a contour map of the topography channel is superimposed onto the blue transmission image. The metal islands are instantly recognizable as flat triangles. The bright features, representing the increased transmission in the center of the islands, appear to be offset by about one

half the distance between two flat valleys, corresponding to around 150 nanometers. The direction of the offset cannot be determined in this image due to the high degree of symmetry but could be established in a scan featuring a defect, such as two islands stuck together. The offset is equally visible in (f) – an overlay of the topography channel (representing the height of the features in this figure) and the transmission channel (representing the color of the features in this figure). In order to present the data more effectively, the fine detail of the topography channel has been filtered out. The flat terraces now appear (artificially) as sharp peaks, however, only their locations relative to the transmission maxima are relevant in this figure. If both sets of features lined up perfectly, the peaks on this figure would be dark (low transmission) and the valleys would be bright (high transmission). Instead, one notices that all bright features appear on the slopes, not in the valleys.

Tip-sample interactions are not only influenced by the number of "tips" on the probe apex but also on their size and shape. As long as sample surface features are larger than the tip asperities, they will be resolved accurately. During normal scanning, however, the tip shape is gradually blunted through interactions with the surface (see figure 4-16). The resulting topography image is then a convolution of the tip and sample feature shapes. For example, large aluminum grains in the probe coating can create a multiple tip effect. Convolution artifacts do, however, preserve the correct surface feature heights as long as the tip is small enough to reach the troughs between features. Eventually, the optical aperture of the tip is eroded as well and the near-field contrast is lost.

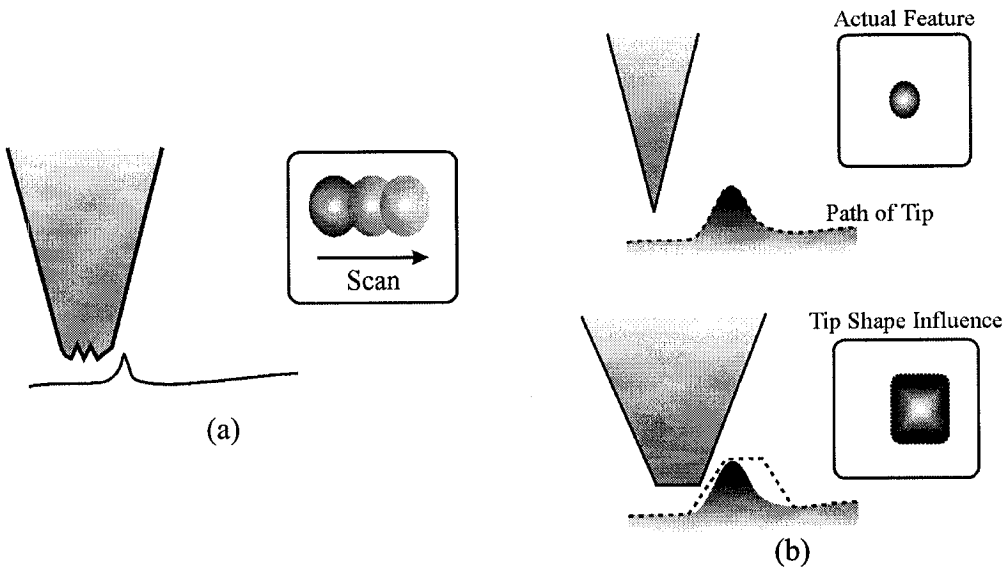

Figure 4-16. Two common AFM artifacts: (a) Multiple-tip effect (b) Tip-sample convolution. With a small, sharp tip, the sample features are reproduced accurately. In the bottom image, the dotted line refers to the path of the leading edge of the tip. Here, the blunt tip exerts a considerable influence on the final shape of the feature.

A tip-blunting effect is shown in figure 4-17. Tips generally last for approximately two to three days worth of imaging, corresponding to a tip travel distance of 3.5 to 5 millimeters, before wearing down. This effect can occur much more rapidly as a result of the apex rubbing against a pronounced surface feature (say, a large dust particle in the scan region). Even a smooth surface will show tip wear due to intermittent contact between the tip and the surface during the scan under shear-force feedback. Regardless of its origins, the blunting of the tip is readily observable as a smearing out of surface topographical features. Figure 4-17 represents a SNOM scan of the same location on the calibration sample as in figure 4-15 taken two days later with the same tip.

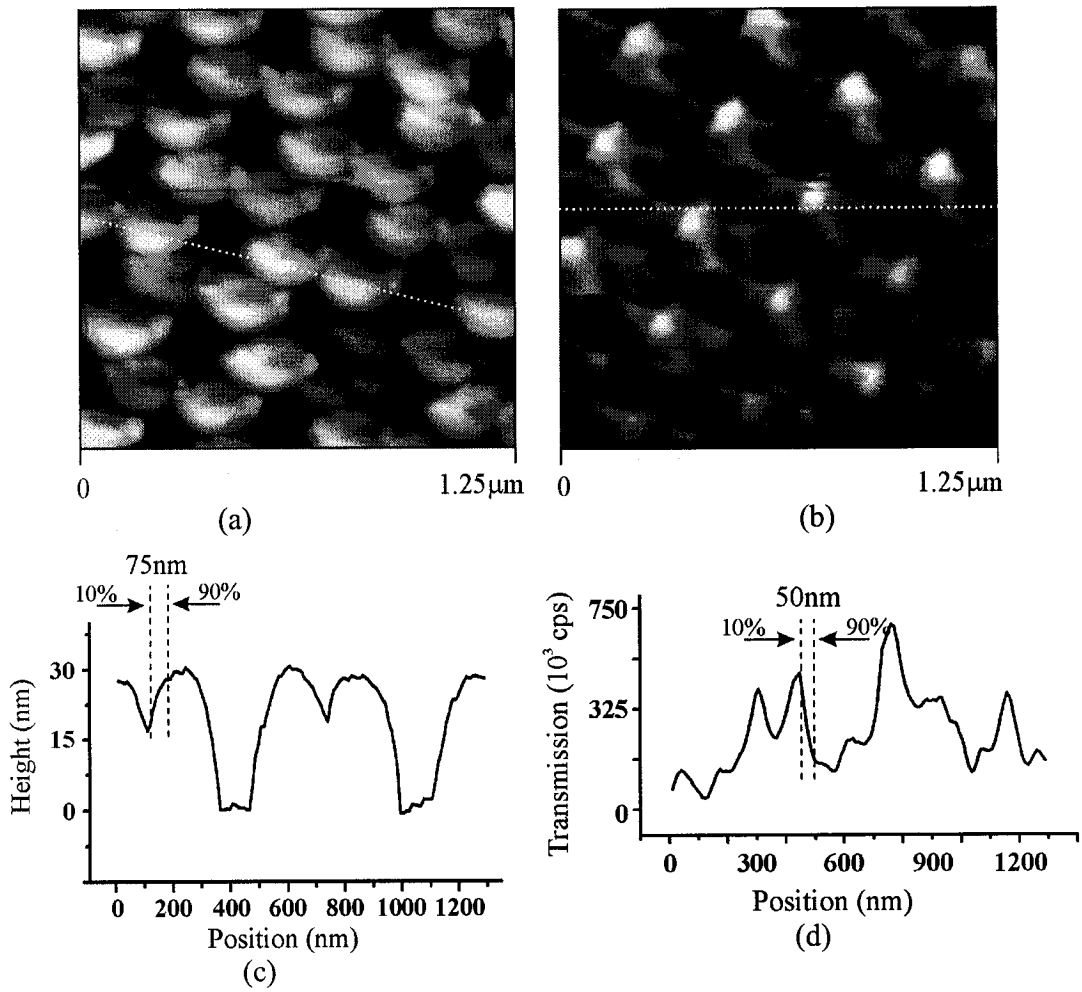

Figure 4-17. Calibration sample, as in Figure 4-15, after more than 20 hours of scanning. (a) Topography channel – the color scale spans 30 nanometers in height. (b) Transmission in the blue wavelength – the color scale spans 730,000 cps. (c) Topography cross-section along dotted line in (a). (d) Transmission cross-section along dotted line in (b).

The triangular island features are still recognizable and still display the same symmetry. However, the topographical resolution has degraded to no better than 75 nanometers and the multiple-tip artifact has disappeared. It is of interest that, whereas the shape of the islands has changed, their height has not – a clear sign of a convolution artifact. It is also interesting that the optical channel has not suffered from the same degradation in resolution as the topography. This is more impressive given that the count rate has

increased dramatically[†††]. Two hypotheses can reconcile both of these observations. The original tip may have been formed with a significant amount of aluminum outcropping over the apex, distancing the aperture from the surface and reducing transmission through increased signal loss. As the tip is worn down, intensity increases as the optical aperture nears the surface. This would require as little as a 5 nanometer outcropping ledge[122]. Such a ledge cannot been observed under SEM analysis of apertures due to limited resolution of the microscope available to us as well as the difficulty in localizing the exact location of the aperture. A second explanation is that the increase in transmission occurs due to strengthened coupling between the aperture and the surface due to some intermediary agent. An aluminum "particle" (from the tip itself or possibly the surface) may have shifted into the aperture and acted to change the boundary conditions between the aperture and the surface, actually increasing throughput from the tip[42]. Such mediated transmission has been observed before[123]. Further evidence of a re-organization of the tip shape is that the offset between the topography and optical channels has disappeared (see figure 4-18).

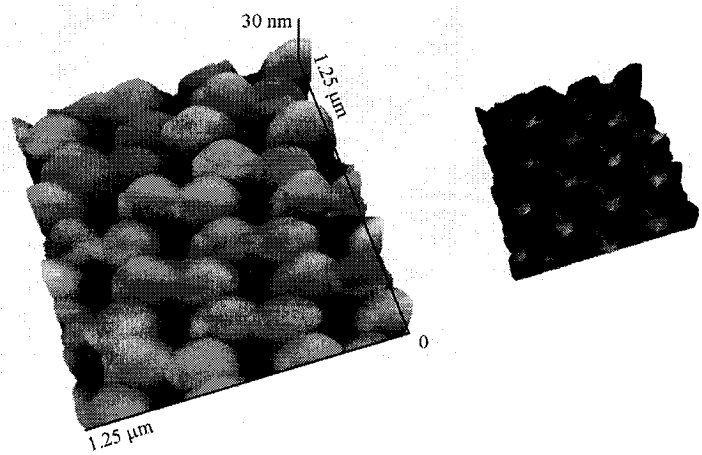

Figure 4-18. Left – A 3-dimensional overlay of the two images in figure 4-17 – the topography in this image is taken from the topography channel whereas the color scheme is taken from the blue wavelength channel with *darker* hues signifying an *increase* in optical transmission. Note that this color scheme is **inverted** from the one used in figure 4-15. The inset to the right shows that using the original color scheme, where light signifies increased transmission, creates too dark an image. The vertical scale here is slightly exaggerated so as to better present the view of the valleys.

[†††] This is not an instrumentation effect. Great care is taken to optimize the transmission signals before beginning a scan. Drifts in fiber coupler, microscope, or PMT alignment **reduce** the count rate.

Some SNOM contrast is exceptionally challenging to attribute to a single known effect or to model successfully. In subsequent scans to the one in figure 4-5, using the same fiber probe and location on the sample, the tip began to dull as expected. What was unexpected was that the two optical channels began to exhibit very different contrasts (see figure 4-19).

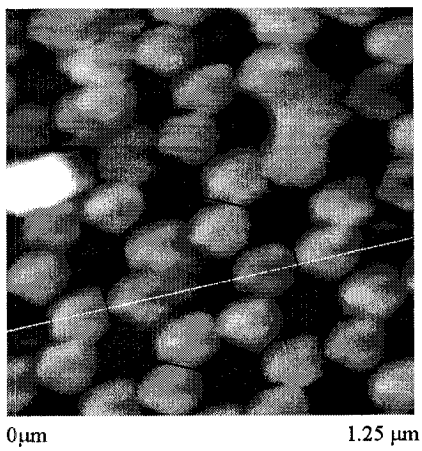

(a)

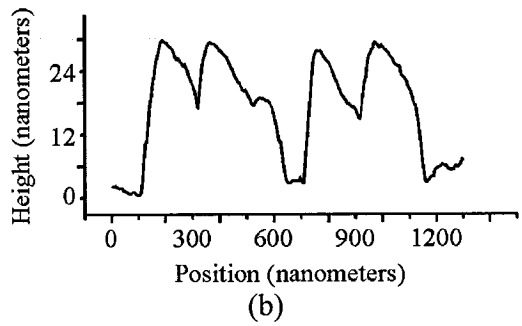

(b)

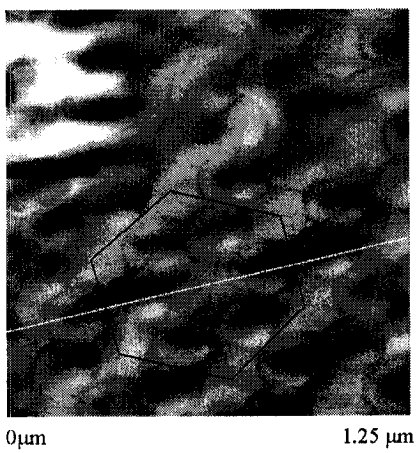

(c)

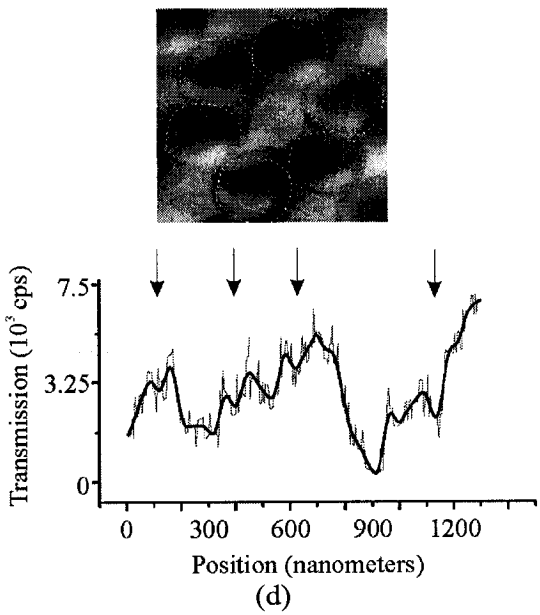

(d)

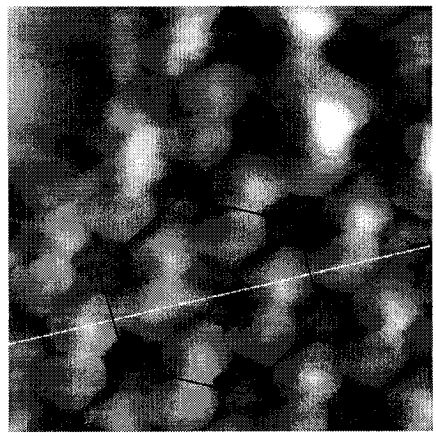

(e)

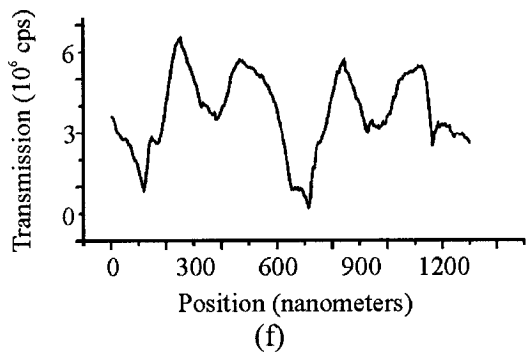

(f)

Figure 4-19. (a) Topography image of 300 nanometer calibration sample. The color scale spans 30 nanometers in height. The cross-section along the dotted white line is plotted in (b). The black hexagon highlights the symmetry present in the optical channels. (c) Ultraviolet transmission image. The color scale spans 7,500 counts per second. The black hexagon highlights the symmetry of the transmission peaks. The cross-section along the dashed line (across the dark islands) is plotted in (d) as the red line. A low-pass filter of this data is plotted as the black line. The arrows correspond to canal features described in text. (e) Blue wavelength transmission image. The color scale spans 6.5×10^6 counts per second. The black hexagon highlights the symmetry of the expected position of the transmission peaks. The cross-section along the dashed line (across the expected position of the dark islands) is plotted in (f).

The topography image presents the aluminum islands as rotund islands rather than sharp triangles. However, the location of the islands does exhibit the correct symmetry and all have the same shape, strong evidence that the tip is now blunt and that the rounded shapes are in actuality a scanning artifact. It is interesting to note, however, that the topography cross-section has sharp features (namely the dips between the peaks) which one would not expect to resolve using a blunt tip.

The two optical channels exhibit considerably different contrast. The ultraviolet channel features almost 50% less intensity than originally present days before (see figure 4-5c). The island features, while still discernible, are not well defined and each features a bright tip on the bottom edge. The transmission increases at the center of the islands but these features now cover the entire center, without a clear peak as was seen before. Furthermore, a series of darker lines, similar to channels, surround each of the islands.

These trenches (emphasized in the insert of figure 4-19d by dotted contours) correspond to the outlines of the island features on the topography channel. The plot in figure 4-19d includes four arrows where the trenches occur in this cross-section. The cross-section itself is graphed as the thin red line in this plot but includes much noise. The noise level is greater than can be accounted for by counting statistics and combined PMT/pulse counter errors. A low-pass filter was applied to the data which is graphed as the thicker black line on the plot.

The contrast in the blue transmission channel is also unexpected. The features in figure 4-19e are almost exactly equivalent to those in the topography channel (see figure 4-20).

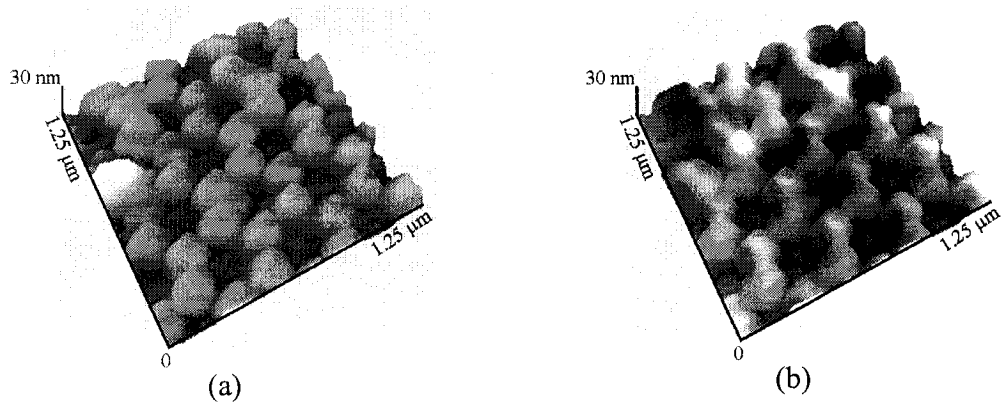

Figure 4-20. (a) Three-dimensional plot of topography channel in figure 4-19a. (b) three-dimensional overlay where the topography is taken from (a) and the color scheme taken from the blue transmission channel in (e).

The three-dimensional overlay of the topography and the blue transmission channels shows increased transmission at the aluminum islands and decreased transmission in the island centers. There are a few candidates to explain this phenomenon. The presence of an optical offset is doubtful since the symmetry of the islands is not the same as the symmetry of the centers. A convincing case can be made for a topographical cross-talk artifact until one considers that the contrast on the ultraviolet channel is precisely the inverse of the blue channel, with transmission peaks lining up perfectly with the island centers. One would certainly expect cross-talk to effect both optical channels equally. The final explanation must lie in a different coupling behavior between ultraviolet and blue wavelengths to the aluminum layer. Experiments are just beginning to probe the

intricacies of near-field transport[123,124,125]. Still, this represents wavelength-dependent contrast in the near-field and is only observable as a comparison of transmission signals between two SNOM wavelengths.

The fact that the coupling is different for the different wavelengths is seen again in another scan of the 5 nanometer calibration sample, this one at another location on the sample and with another tip (see figure 4-21). The topography image exhibits the same features as those in figure 4-8a, including the presence of polystyrene residue. The different contrast in the two optical channels is quite apparent.

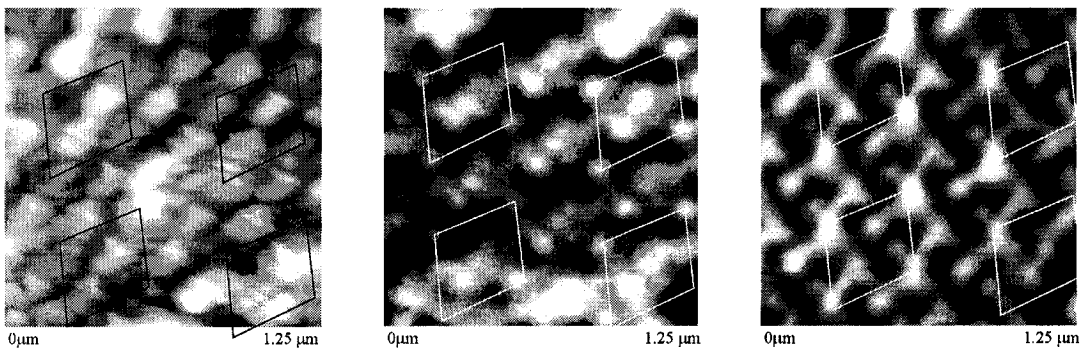

Figure 4-21. Dual-Wavelength SNOM image of 300 nanometer calibration sample with 5 nanometers of aluminum. (a) Topography image – gray scale spans 5 nanometers in height. (b) UV transmission image – gray scale spans 40,000 cps. (c) Blue transmission image – gray scale spans 1.25×10^6 cps. Each parallelogram links the centers of four neighboring sets of islands. Parallelograms are used instead of hexagons but the symmetry is the same as before.

We are unable to fully explain the intricate contrast present in figures 4-19 and 4-21. A comprehensive theory explaining near-field contrast is still many years away, yet the differences between the two wavelength channels is another clue, another step forward.

4.3.2 Wood Cells

As we saw with the calibration sample, the inclusion of a second wavelength enables a better interpretation of the SNOM images. In our Black Spruce studies, lignin in the wood cell walls and middle lamella created a significant contrast in the ultraviolet

channel. SNOM studies still present a challenge, though, in properly interpreting the complex images (see figure 4-22).

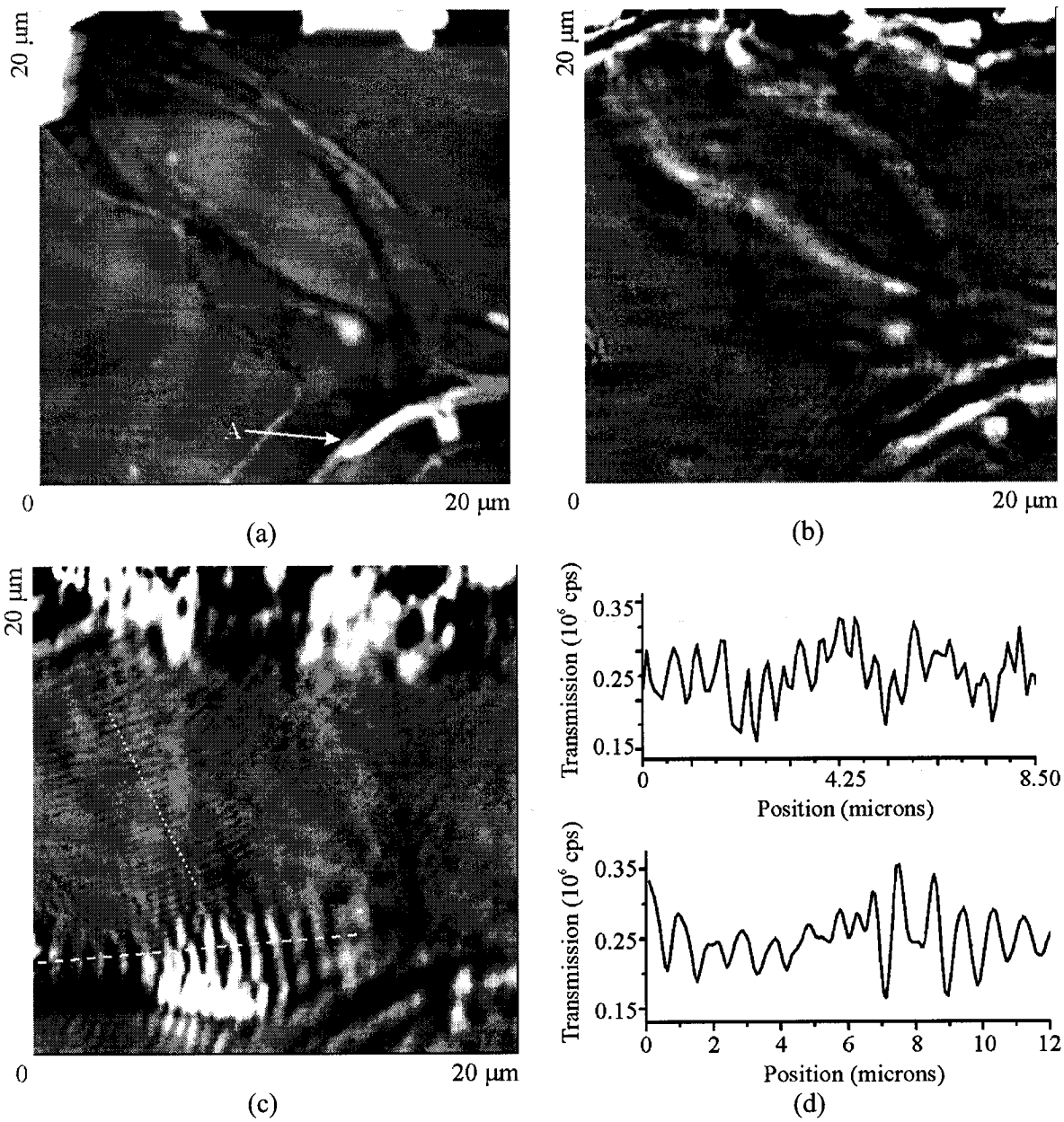

Figure 4-22. Dual-Wavelength SNOM image of transverse cross-section of wood cells. (a) Topography – the color scale spans 25 nanometers in height (b) Ultraviolet transmission – the color scale spans from 10,000 to 100,000 cps (c) Blue Transmission – the color scale spans from 150,000 to 400,000 cps (d) Top: cross-section of (c) along dotted line. Bottom: cross-section of (c) along dashed line.

The topography image, figure 4-22a, shows what is most likely the top portion of a wood fiber, sandwiched between three other, larger, fiber cross-sections. The cell wall structure is around 5 nanometers in height but does not seem intact for parts of this cell, especially on its left side where the thickness varies considerably. The fiber on the bottom right of the image seems better preserved as its cell walls are clearly distinguishable. Between these two fibers is a bright band defect (labeled A) similar to those seen in the previous topography images. The top portion of the image is distorted due to larger band structures, revealing the microscope's diminished ability to track the surface of soft samples (this was seen previously in figure 4-11).

The ultraviolet transmission image, figure 4-22b, reveals a number of interesting features. The band (A) between the middle cell and the one at the bottom right shows decreased transmission, as it does in the blue channel, confirming it is an actual sectioning feature and not a cell structure, which would be seen to show different optical contrast in the two wavelengths. This differentiation between a physical structure and a chemical composition is a critical feature of the dual-wavelength SNOM.

The central cell is surrounded by a broad increase in transmission which is awkward to attribute to any specific feature in the topography since the lack of recognizable features on that channel makes direct comparison difficult. However, a comparison with the blue transmission image reveals more. The broad feature encircling the cell seen in the ultraviolet channel is absent from the blue transmission channel, suggesting this is a chemical contrast effect.

A couple of features are present in the blue transmission channel that have no counterparts in the other optical channel. There appears to be two periodic effects on the surface. The small amplitude periodic structure of the feature in the center of the image is shown in cross-section as the top plot in figure 4-22d. Its wavelength is 450 +/- 10 nanometers, or about λ (442 nm) for this channel. The exact origin of this effect is not known but there is a likely candidate. Since the PMT filters out any light other than 442 nanometers and the intensity is greater than that encountered even with the room lights

on, the source of the light must be the fiber probe. Since the aperture illuminates too small an area to produce such large-scale features, light must emanate from a coating pinhole further up the taper. The oscillations seem like a circular wave pattern with a source, judging by the radius of the wavefronts, about 20 microns past the top left corner of the image. It is possible that light leaking from the pinhole is reflecting off of the surface feature back to the tip and is then being scattered by the tip into the sample and to the detector. As the tip scans the surface, a circular plot of the interference pattern is generated.

The larger amplitude wave at the bottom of the image is shown in cross-section as the bottom plot in figure 4-22d. Its wavelength is 900 +/- 10 nanometers, or 2λ. This effect is not likely attributable to interference as in the case above due to the large amplitude variations and the lack of an apparent single source. Given the absence of features in the topography and ultraviolet channels in this region, we are unable to explain this effect.

The absence of such periodic features in the ultraviolet channel suggests either a lack of sufficient intensity (which is more likely) or sensitivity (which is less likely) or the absence of scattering centers of the appropriate size for this wavelength. Scattering effects were also observed in figures 4-11 and 4-13.

As discussed in chapter 2, the slow adoption of SNOM has been due to its highly complex image contrast. The models covered in section 2.2 have had limited success in accounting for intricate tip geometries, non-linear distance control, and convoluted electromagnetic field interactions. The examples in this section highlight the wealth of data present in every SNOM image, the challenge in developing simple yet complete interaction models, and the importance of innovative techniques, such as dual optical channels, in interpreting the non-trivial contrast. Successful commercial implementation of SNOM will depend on reproducible probes with fully characterized optical geometries, imaging conditions which are stable over hours, and more advanced models for optical contrast.

4.4 Summary

Dual-wavelength SNOM is an important tool in the investigation of near-field images and a valuable instrument for the study of organic samples. By comparing and contrasting the topographical and both optical channels, one reveals the presence of true near-field contrast, permits the determination of sample chemical structure and can effectively recognize cross-talk effects.

To investigate these abilities, a calibration sample was patterned using a close-packed array of polystyrene microspheres. SNOM images of this sample reveal the resolution of the instrument to be better than 15 nanometers for the topography channel and 30 nanometers for the optical channels. Careful attention was paid to the symmetry of these images in order to discount the possibility of cross-talk. Chemical contrast was achieved, and the principle of chemical species identification was demonstrated, at this spatial resolution. Scanning cross-talk was demonstrated to influence the optical channels but was recognized as such by contrasting both wavelengths. Given the complex contrast mechanisms, there can be a significant challenge in interpretation of the SNOM images.

A biological application, highlighting the use of ultraviolet light in our instrument, was studied. Black Spruce sections revealed the various components of the wood cell, with the cell walls and middle lamella regions highlighted, through their increased concentrations of lignin, in the ultraviolet image channel. Chemical composition changes across the embedding resin were also observed.

Conclusions and Outlook

Scanning Near-Field Optical Microscopy is a powerful tool for the challenges ahead in science and technology. It is especially well suited to the fields of biology and biotechnology. SNOM combines the surface sensitivity of an Atomic Force Microscope with the contrast mechanisms of optical microscopy yet it features a resolution of more than an order of magnitude beyond conventional optical microscopes. The key to this impressive combination lies with the carefully constructed optical fiber probes and the sensitive scanning interactions.

For this work, a SNOM was constructed which operates at two wavelengths simultaneously. The microscope uses a geometry where the tip (and the associated optical axis) is held fixed while the sample is raster scanned. Shear-force interactions between the tip and the sample are measured as changes in oscillation amplitude of the quartz tuning fork to which the fiber probe is glued and used to maintain a tip-sample separation of a few nanometers. The light emerging from the tip is collected on the far side of the sample, and focused into two photomultiplier tubes, generating the optical images. A dichroic mirror separates the two wavelengths and filters are used to reduce background noise.

Different methods for preparing the fiber probes were investigated and an optimized procedure was developed. Short, smooth tapers are created by etching the fibers in a hydrofluoric acid solution without first removing the plastic jacket. Once the taper is formed, the aperture is created by metallizing the taper region with more than 10 optical decay lengths' worth of aluminum. A physical vapor deposition evaporator which rotates the fibers during coating was built for this task.

A topographical and optical calibration sample was made in order to reveal the resolution limits of the instrument. Polystyrene microspheres were assembled in a close-packed

monolayer on a clean glass coverslip substrate and served as a pattern mask for a thin film of aluminum. SNOM images of the triangular patterns left after dissolution of the spheres reveal the spatial resolution of the instrument to be 15 +/- 1 nanometers. Optical resolution was found to be 30 +/- 2 nanometers (independent of wavelength), corresponding to $\lambda/11$ for the ultraviolet wavelength channel and $\lambda/15$ for the blue wavelength channel. The presence of polymer residue was evident on these images as a relative change in the transmission of both wavelength channels. The identification of polystyrene as well as the different absorption through a thin aluminum film at each wavelength means that the instrument can achieve chemical contrast with very high resolution.

The choice of 325 nanometers, in the ultraviolet portion of the spectrum, as one of the wavelengths was motivated by the applications of this instrument to the study of biological samples. As an example of the relevance of this technique, a study was done on transverse wood cell sections in order to examine the chemical composition of the cell. The study found increased concentrations of lignin, a cross-linked polymer which absorbs ultraviolet light, in the cell walls and especially in the middle lamella region between cells.

In general, SNOM images are both more complicated and potentially contain more information than their far-field counterparts. Since the shear-force interactions are not well understood (many competing models exist) it is difficult to deconvolute the scanning process from the optical images. Intensity emitted from the probe aperture depends sensitively on the coupling between the tip and the surface. The coupling parameters are different for the two wavelengths, however the ratio of the two wavelengths may be used to extract chemical composition information about the sample. The ability to identify scanning artifacts, especially topographical cross-talk, and to provide chemical contrast to samples are the main advantages of dual-wavelength over standard SNOM covered in this work.

There are other current applications of multi-wavelength SNOM, most notably spectroscopic SNOM (s-SNOM)[126-128]. In contrast to the work presented here, the Near-Field probes in these instruments cover a range of wavelengths by emitting or collecting one wavelength at a time. Understanding of Near-Field fluorescence, often of single molecules, has benefited from such studies. Since the optical images are not acquired simultaneously, however, it is not possible to discount cross-talk effects as a source of contrast. Nor is it feasible to investigate chemical contrast since optical coupling between the probe and the sample is dominated by topography effects present in subsequent passes over the sample target. Finally, spectroscopic studies have primarily focused on near-infrared wavelengths whereas our microscope is unique in its ability to probe into the ultraviolet.

Critically, I must acknowledge that our microscope is not yet ready for in-depth studies of the chemical composition of samples. Successful scans on all three channels simultaneously are not yet routine and the images are often too complex to analyze effectively. Both the shear-force scanning mode and the metal coating on the fiber probes must be improved before a quantitative analysis of surfaces may be undertaken. These two issues are now being addressed by new members of our group and I wish them much success. It is of note that the instrument developed for this work is still state-of-the-art in the field of SNOM in terms of its resolution, two simultaneous optical channels and detection in the ultraviolet.

Challenging work lies ahead. Theoretical models explaining the shear-force contrast are needed which fully explain all the features of this interaction. Also, a more complete picture of the optical coupling between the tip and the sample surface is essential to the proper interpretation of SNOM images. These two hurdles lie in the way of fully quantitative analyses of topographical and optical SNOM studies.

Some instrumentation issues should also be considered:

- Although chemical contrast is possible using our present setup, further investigations will require a more delicate force feedback mechanism, especially

for soft samples, such as the wood cells. The most promising alternative has been to oscillate the fiber along its length (perpendicular to the sample surface) and to softly contact the sample intermittently[129] in a technique commonly known as "tapping mode". The sensitivity and limited sample contact of this method has made it very successful in AFM studies. The SNOM should be modified to scan in this mode.

- The coating procedure should be optimized in order to eliminate pinholes on the fiber probes.
- The two wavelengths are not filtered independently and so there is a trade-off between intensity in the ultraviolet channel (and corresponding decrease in noise) and the possible interference observed in the blue channel. One should develop an etching procedure for fibers which conduct ultraviolet light more effectively and consider separate filters for each optical channel.
- A phase locked loop (PLL) could be implemented in the SNOM[95,130,131] in order to measure the damping of the oscillating probe and further investigate the shear-force origins. This could also help speed up data acquisition.
- Since the tuning fork is piezoelectric, it could be made to self-oscillate and thus remove the need for an external dithering piezo[98]. This would allow the fiber probe to be placed on the scanner piezo and to be scanned over a stationary sample, a setup desirable for converting the SNOM to a collection mode geometry. Some progress was made by the author to modify the microscope in order to acquire collection mode SNOM images of Vertical Cavity Surface Emitting Lasers (VCSELs), however accurate feedback of the cavity surface was not possible.
- Polarization measurements should be possible using the microscope. A quick measurement using a linear polarizer found in camera filters reveals the extinction coefficients[‡‡‡] are 25 +/- 5 for the ultraviolet channel and 35 +/- 4 for the blue channel. Note that this type of polarizer is not well suited for measurements in

[‡‡‡] The polarization extinction coefficient is the ratio of the maximum intensity available through a polarizer divided by the intensity at 90° to the transmission axis. Higher numbers signify greater contrast between the two polarization modes.

the ultraviolet. Still, these coefficients are comparable to those used in previous SNOM studies[30,132]. Modulations of the polarizations could improve contrast between the two wavelengths and also be used to investigate the coupling differences as a function of wavelength.

Appendices

A.1 Data File Format

The SNOM images in this work were acquired using the Nanoscope software from Digital Instruments versions 4.22r2.pete and 4.32r4. Proper understanding of the data file format is crucial when exporting the raw data to be analyzed using third-party applications. Each scan, which may comprise one to three images, is stored in binary format including a header, containing the various parameters and settings used to acquire the images, and the image data itself, stored as two bytes (2^{16}) per pixel in two's complement form. A Ctrl-Z character signals the end of the header and a padding of random data is inserted prior to the image data in order to produce headers of the same length. The files do not end with a special character.

The header is divided into a first section, which describes the scanning parameters common to each image, such as the scan size and orientation, and then a separate section for each of the acquired images. The **\Data offset** parameter for each image is crucial since it denotes the N^{th} byte where the image data begins – for the first image, this is usually 8192, that is after the 8KB header. The **\Data length** parameter indicates the length of the data for each image – this is typically 131072 (128KB) in our studies. Simply add the **\Data offset** and **\Data length** together to determine the offset for the next image. The **\Z scale** parameter may be used to convert the data to the indicated units, eg. For **\Z scale: 20000 nm**, we have $\text{data (nm)} = \left(\frac{\text{pixel value}}{65{,}536} \right) \cdot 20{,}000$. The **\Z sensitivity** parameter, given in nanometers per volt, may be used to obtain the maximum Z-axis scanner travel by multiplying its value by 440 volts.

Once the image is acquired, the software scales the data to the full 16-bit range in order to provide maximum resolution along the Z-axis. Most data values, however, will be located in the center region of the +/-32,768 range with the extremes usually denoting noise spikes. This means that even inherently positive data, such as photon count rates, will be represented, at least in part, by negative numbers in the data file.

To convert the raw data into height values, locate the following parameters (here bolded and in parentheses) in the header for the height image and use the expression:

$$\text{data (nm)} = \left(\frac{\text{pixel value}}{65{,}536}\right) \cdot (\backslash\,\textbf{@2 : Z scale}) \cdot (\backslash\,\textbf{@Sens. Zscan})$$

Data from the pulse counters is stored and scaled similarly to the height values. To convert these into actual values, locate the following parameters (again bolded and in parentheses) in the header for the optical image and use the expression:

$$\text{data (MHz)} = \left(\frac{\text{pixel value} + 32{,}768}{65{,}536}\right) \cdot (\backslash\,\textbf{@ : Z magnify}) \cdot (\backslash\,\textbf{@2 : Z scale})$$

Note that to convert the data properly, the images should be acquired with the **Offline Planefit** settings set to **None**.

A.2 Wood Cells

The pulp and paper industry is one of Canada's most important economic forces. In 1999, it employed eighty thousand people and accounted for over twenty billion dollars worth of exports. The evergreen (or "softwood") forests of Canada's west coast are one of our most treasured resources. A brief description of the composition of the cells and previous ultraviolet microscopy studies follows.

The interior of the cell, called the lumen (L), is void, acting as a canal for fluid traveling along the length of the tree (see figure 4-10). It is surrounded by two layers of cell wall, the second layer having several components. The inner and outer layers of the secondary cell wall (S3 and S1) are about 0.1 μm thick. The middle section of the secondary wall

(S2) is the main component of the fiber and is between 2 μm and 10 μm thick. The different layers are characterized by different alignments of microfibrils (cellulose bundles) along the length of the cell. The cell is encased in a 0.05 μm thick, relatively impermeable, covering called the primary wall (P). The cells are bonded together by the middle lamella (M) region consisting mostly of lignin.

During the pulping process, the fibers are either mechanically separated (in large trunk graters) or chemical treatments are used to dissolve the middle lamella region, leaving the fibers (mostly) intact. Chemically separated fibers produce a much higher quality pulp and so much work has gone into the study of lignin in an effort to better understand the pulping process and increase yields without damaging the fibers themselves. In addition, lignin residues in wood pulp are the principle cause of paper yellowing with exposure to light.

Lignin acts as a binder inside and outside the cell to give wood its strength and rigidity. As an end-product of plant metabolism, the lignification of the cell usually corresponds to its death. A schematic representation is given in figure A-1.

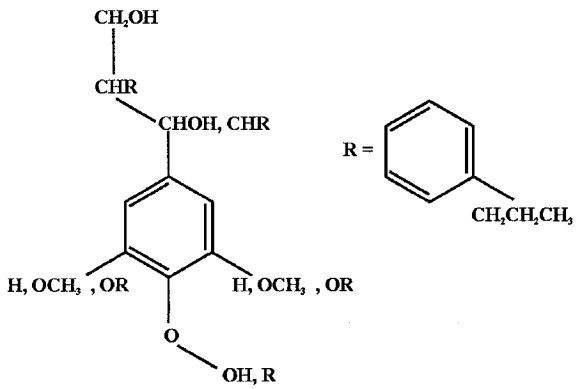

Figure A-1. Basic diagram of lignin as a complex cross-linked polymer network based mostly on phenylpropane (R) units bonded with ether linkages[133].

Studies of lignin usually involve chemically isolating it into an aqueous mixture. Since few contrast mechanisms exist for differentiating it from the carbohydrates in the fiber, few studies have involved intact cells. The most promising analysis was done using

lignin's preferential absorption of light in the ultraviolet spectrum. Absorption in the UV is dramatic for lignin, peaking at 280 nanometers, whereas carbohydrates do not exhibit any optical contrast in the UV. Studies done in 1969 (see Figure A-2) using an exceptionally elaborate ultraviolet microscope, reveal increased lignin concentrations in the secondary wall and a sharp increase in the middle lamella region between the cells. As with other conventional optical microscopy methods, the resolution of the microscope was limited by the wavelength of light – the studies were in fact not able to resolve features below 500 nanometers. Chemical contrast of lignin has only recently been achieved beyond that scale by using dual-wavelength SNOM.

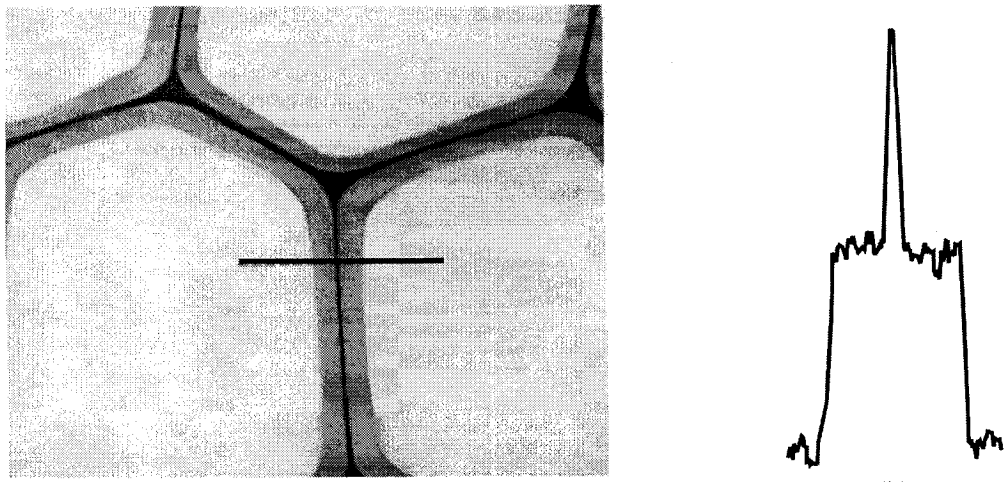

Figure A-2. (a) Photomicrograph of Black Spruce cell sample taken at 240 nanometers. The wood fibers were embedded in Epon resin then microtomed. The bar represents 10 μm. (b) Densitometer trace across the central 7.5 microns of the solid bar (From J. A. N. Scott, A. R. Procter, B. J. Fergus and D. A. I. Goring, *Wood Science and Technology*, **3**, 73 (1969))

Many questions still remain about lignin and its role in the cell: What is the lignin concentration and molecular structure in the various cell walls? How do these vary as a function of wood species? How can we better target the lignin in the pulping process while sparing the cellulose?

Figure A-3 highlights a number of features of the cells.

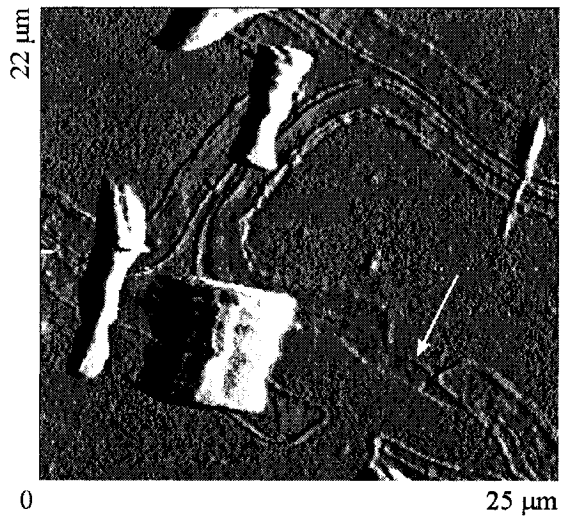

Figure A-3. Topography channel (shear-force) of the wood cells used in this study. The image is differentiated to highlight the cell features overshadowed in the normal image by the 4 tall bands between cells. Arrow in error signal image points to bordered pit torus.

The lumen, cell walls and middle lamella regions are visible in the image. As a bonus we can even see a bordered pit structure. A familiar site in wood studies, many of these pits are present on each fiber. They are cavities through the secondary wall which serve as channels for the passage of water and are controlled by a membrane of the middle lamella called a torus.

References

[1] E. Abbe, *Archiv f. Mikroskop. Anat.*, **9**, 413 (1873)
[2] E. Synge, *Phil. Mag.*, **6**, 356 (1928)
[3] G. Binning and H. Rohrer, *Helv. Phys. Acta*, **55**, 726 (1982)
[4] D. W. Pohl, W. Denk, and M. Lanz, *Appl. Phys. Lett.*, **44**, 651 (1984)
[5] S. Bourzeix, J. M. Moison, F. Mignard, F. Barthe, A. C. Boccarra, C. Licoppe, B. Mersali, M. Allovon, and A. Bruno, *Appl. Phys. Lett.*, **73**, 1035 (1998)
[6] C.E. Talley, M. A. Lee and R.C. Dunn, *Appl. Phys. Lett.*, **72**, 2954 (1998)
[7] S. Ducourtieux, V. A. Podolskiy, S. Gresillon, S. Buil, B. Berini, P. Gadenne, A. C. Boccara, J. C. Rivoal, W. D. Bragg, K. Banerjee, V. P. Safonov, V. P. Drachev, Z. C. Ying, A. K. Sarychev, and V. M. Shalaev, *Phys. Rev. B*, **64**, art. no. 165403 (2001)
[8] *Introduction to Optics*, by F. Pedrotti and L. Pedrotti, Prentice-Hall, 2nd ed., 1993
[9] For a derivation of the diffraction pattern see, for example, *Light*, by R. W. Ditchburn, Academic Press, 1976
[10] See [1] above for an elegant geometrical derivation. For a more modern insight, see *Optics*, by K. D. Möller, University Science Books, 1988
[11] G. A. Massey, *Appl. Opt.*, **23**, 658 (1984)
[12] *Optical Signal Processing*, by A. VanderLugt, Wiley-Interscience, 1993
[13] *Near-Field Optics: Theory, Instrumentation and Applications*, by M. A. Paesler and P. J. Moyer, Wiley-Interscience, 1996
[14] H. Bethe, *Phys. Rev.*, **66**, 163 (1944)
[15] C. J. Bouwkamp, *Philips Res. Rep.*, **5**, 321 (1950)
[16] A. Roberts, *J. Appl. Phys.*, **70**, 4045 (1991)
[17] A. Liu, A. Rahmani, G. W. Bryant, L. J. Richter, and S. J. Stranick, *J. Opt. Soc. Am. A*, **18**, 704 (2001)
[18] D. Van Labeke and D. Barchiesi, *J. Opt. Soc. Am. A.*, **9**, 732 (1992)
[19] D. Barchiesi and D. Van Labeke, *J. Mod Opt.*, **40**, 1239 (1993)
[20] *The 3rd Electromagnetif Wave Simulator*, by C. Hafner and L. H. Bomdoht, Wiley, 1993
[21] *Photons and Local Probes*, by L. Novotny and D. W. Pohl, Kluwer Press, O. Marti and R. Möller, eds., 1995
[22] O. Keller, *Phys. Rev. B.*, **38**, 8041 (1998)
[23] O. Keller, *Phys. Rev. B.*, **37**, 10588 (1998)
[24] A. Dereux and D. Pohl, "The 90 degree prism edge as a model SNOM probe: near-field, photon tunneling, and far-field properties" *Near-Field Optics* (NATO ASI Series E242) ed. by D. Pohl and D. Courjon, Kluwer press, 1993
[25] C. Girard, X. Bouju, and A. Dereux, "Optical near-field detection and local spectroscopy of a surface: a self-consistent theoretical study" *Near-Field Optics* (NATO ASI Series E242) ed. by D. Pohl and D. Courjon, Kluwer press, 1993
[26] O. J. F. Martin, C. Girard, and A. Dereux, *Phys. Rev. Lett.*, **74**, 526 (1995)
[27] E. Economu, *Green's Functions in Quantum Physics*, 2nd ed., Springer, 1983

[28] C. Girard, A. Dereux, O. Martin, and M. Devel, *Phys. Rev. B*, **52**, 2889 (1995)
[29] A. Dereux, C. Girard, and J.-C. Weeber, *J. Chem. Phys.*, **112**, 7775 (2000)
[30] B. Hecht, H. Bielefeldt, D. W. Pohl, L. Novotny, and H. Heinzelmann, *J. Appl. Phys.*, **84**, 5873 (1998)
[31] R. Carminati, A. Madrazo, M. Nieto-Vesperinas, and J.-J. Greffet, *J. Appl. Phys.*, **82**, 501 (1997)
[32] B. Hecht, J. Bielefeldt, Y. Inouye, and D. W. Pohl, *J. Appl. Phys.*, **81**, 2492 (1997)
[33] P. J. Valle, J.-J. Greffet, and R. Carminati, *J. Appl. Phys.*, **86**, 648 (1999)
[34] J. Schöfer, M. J. Gregor, P. G. Blome, and R. G. Ulbrich, *J. Appl. Phys.*, **81**, 5871 (1997)
[35] E. Betzig, J. K. Trautman, J. S. Weiner, T. D. Harris, and R. Wolfe, *Appl. Optics*, **31**, 4563 (1992)
[36] J-C. Weeber, E. Bourillot, A. Dereux, J.-P. Goudonnet, Y. Chen, and C. Girard, *Phys. Rev. Lett.*, **77**, 5332 (1996)
[37] M. Xiao and X. Chen, *Opt. Eng.*, **39**, 2495 (2000)
[38] E. Betzig, P. L. Finn and S. J. Weiner, *Appl. Phys. Lett.*, **60**, 2484 (1992)
[39] R. Toledo-Crow, P. C. Yang, Y. Chen, and M. Vaez-Iravani, *Appl. Phys. Lett.*, **60**, 2957 (1992)
[40] *Fiber Optics Devices and Systems*, by P. K. Cheo, Prentice-Hall, 1985
[41] L. Novotny and C. Hafner, *Phys. Rev. E*, **50**, 4094 (1994). The value of 160 nanometers was derived for $\lambda \approx 400$ nm, about the average of the two wavelengths used in the dual-wavelength SNOM.
[42] B. Hecht, B. Sick, U. P. Wild, V. Deckert, R. Zenobi, O. Martin and D. Pohl, *J. of Chem. Phys.*, **112**, 7761, (2000)
[43] G. A. Valaskovic, M. Holton, and G. H. Morrison, *Appl. Opt.*, **34**, 1215 (1995)
[44] B. I. Yakobson, P. J. Moyer, and M. A. Paesler, *J. Appl. Phys.*, **73**, 7984 (1993)
[45] *Hydrodynamic and Hydromagnetic Stability*, by S. Chandrasekhar, Oxford University Press, 1961
[46] R. L. Williamson and M. J. Miles, *J. Appl. Phys.*, **80**, 4804 (1996)
[47] D. R. Turner, C. Township, and M. County, US Patent number 4,469,554 (1983)
[48] P. Hoffman, B, Dutoit, and R. P. Salathé, *Ultramicroscopy*, **61**, 165 (1995)
[49] H. Muramatsu, K. Homma, N. Chiba, N. Yamamoto, and A. Egawa, *J. of Microscopy*, **194**, 383 (1999)
[50] T. Pangaribuan, K. Yamada, S. Jiang, H. Ohsawa, and M. Ohtsu, *Jpn. J. Appl. Phys.*, **31**, 1302 (1992)
[51] T. Saiki, S. Mononobe, M. Ohtsu, N. Saito, and J. Kusano, *Appl. Phys. Lett.*, **68**, 2612 (1996)
[52] H. M. Marchman, J. E. Griffith, and R. W. Filas, *Rev. Sci. Instrum.*, **65**, 2538 (1994)
[53] T. Pangaribuan, S. Jiang, and M. Ohtsu, *Scanning*, **16**, 362 (1994)
[54] P. Pantano and D. R. Walk, *Rev. Sci. Instrum.*, **68**, 1357 (1997)
[55] B. A. F. Puygranier and P. Dawson, *Ultramicroscopy*, **85**, 235 (2000)
[56] P. Lambelet, A. Sayah, M. Pfeffer, C. Philipona, and F. Marquis-Weible, *Appl. Opt.*, **37**, 7289 (1998)
[57] R. Stöckle, C. Fokas, V. Deckert, R. Zenobi, B. Sick, B. Hecht, and U. P. Wild, *Appl. Phys. Lett.*, **75**, 160 (1999)

[58] H. Muramatsu, N. Chiba, and M. Fujihira, *Appl. Phys. Lett.*, **71**, 2061 (1997)
[59] R. S. Taylor, K. E. Leopold and M. Wendman, *Rev. Sci. Instrum.*, **69**, 2981 (1998)
[60] R. S. Taylor and K. E. Leopold, *Microscopy and Analysis*, **71**, 15 (1999)
[61] J. F. Wolf, P. E. Hillner, R. Bilewicz, P. Kolsch, and J. P. Rabe, *Rev. Sci. Instrum.*, **70**, 2751, (1999)
[62] W. Noell, M. Abraham, K. Mayr, A. Ruf, J. Barenz, O. Hollricher, O. Marti, and P. Güthner, *Appl. Phys. Lett.*, **70**, 1236 (1997)
[63] H. Heinzelmann, J. M. Freyland, R. Eckert, T. Huser, G. Schürmann, W. Noell, U. Staufer, and N. F. de Rooij, *J. of Microscopy*, **194**, 365 (1999)
[64] H. Zhou, A. Midha, G. Mills, L. Donaldson, and J. M. R. Weaver, *Appl. Phys. Lett.*, **75**, 1824 (1999)
[65] *Scientific Foundations of Vacuum Technique*, by S. Dushman, Wiley (1962)
[66] J. E. Curran, J. S. Page, and U. Pick, *Thin Solid Films*, **97**, 259 (1982)
[67] C. W. Hollars and R. C. Dunn, *Rev. Sci. Instrum.*, **69**, 1747 (1998)
[68] *Procedures in Experimental Physics*, by J. Strong, H. V. Neher, A. E. Whitford, C. H. Cartwright, and R. Hayward, Prentice-Hall, 1938
[69] *Second Japan-France Congress on Mechatronics*, edited by D. Courjon, F. Baida, and C. Bainier, Japan Society for Precision Engineering, Institut des Microtechniques de Franche-Compté, vol. 1 (1994)
[70] K. Luo, Z. Shi, J. Lai, and A. Majumdar, *Appl. Phys. Lett.*, **68**, 325 (1996)
[71] T. Lacoste, T. Huser, R. Prioli, and H. Heinzelmann, *Ultramicroscopy*, **71**, 333 (1998)
[72] D. Mulin, D. Courjon, J-P. Malugani, and B. Gauthier-Manuel, *Appl. Phys. Lett.*, **71**, 437 (1997)
[73] A. H. La Rosa, B. I. Yakobson, and H. D. Hallen, *Appl. Phys. Lett.*, **67**, 2597 (1995)
[74] M. Stähelin, M. A. Bopp, G. Tarrach, A. J. Meixner, and I. Zschokke-Gränacher, *Appl. Phys. Lett.*, **68**, 2603 (1996)
[75] Y. Leviatan, *J. Appl. Phys.*, **60**, 1577 (1986)
[76] E. Marx and E. C. Teague, *Appl. Phys. Lett.*, **51**, 2073 (1987)
[77] E. Betzig and J. K. Trautman, *Science*, **257**, 189 (1992)
[78] U. Dürig, D. Pohl, and F. Rohner, *J. Appl. Phys.*, **59**, 3318 (1986)
[79] S. Shalom, K. Lieberman, and A. Lewis, *Rev. Sci. Instrum.*, **63**, 4061 (1992)
[80] N. F. van Hulst, M. H. P. Moers, O. F. J. Noordman, R. G. Tack, F. B. Segering, and B. Bölger, *Appl. Phys. Lett.*, **62**, 461 (1993)
[81] P. Yang, Y. Chen, and M. Vaez-Iravani, *J. Appl. Phys.*, **71**, 2499 (1992)
[82] R Toledo-Crow, P. Yang, Y. Chen, and M. Vaez-Iravani, *Appl. Phys. Lett.*, **60**, 2957 (1992)
[83] T. Okajima and S. Hirotsu, *Appl. Phys. Lett.*, **71**, 545 (1997)
[84] S. Davy, M. Spajer, and D. Courjon, *Appl. Phys. Lett.*, **73**, 2594 (1998)
[85] D. A. Lapshin, E. E. Kobylkin, V. S. Letokhov, *Ultramicroscopy*, **83**, 17 (2000)
[86] R. Brunner, O. Marti, and O. Hollricher, *J. Appl. Phys.*, **86**, 7100 (1999)
[87] K. Hsu and L. A. Gheber, *Rev. Sci. Instrum.*, **70**, 3609 (1999)
[88] R. D. Grober, T. D. Harris, J. K. Trautman, and E. Betzig, *Rev. Sci. Instrum.*, **65**, 626 (1994)
[89] M. Gregor, P. Blome, J. Schöfer, and R. Ulbrich, *Appl. Phys. Lett.*, **68**, 307 (1996)
[90] R. Brunner, A. Bietsch, O. Hollricher, and O. Marti, *Rev. Sci. Instrum.*, **68**, 1769

(1997)
[91] E. Betzig, J. K. Trautman, T. D. Harris, J. S. Weiner, and P. L. Kostelak, *Science*, **251**, 1468 (1991)
[92] J. K. Trautman, E. Betzig, J. S. Weiner, D. J. DiGiovanni, T. D. Harris, F. Hellman, and E. M. Gyorgy, *J. Appl. Phys.*, **71**, 4659 (1992)
[93] P. N. Moar, S. T. Huntington, J. Katsifolis, L. W. Cahill, A. Roberts and K. A. Nugent, *J. Appl. Phys.*, **85**, 3395 (1999)
[94] D. W. Pohl, H. Bach, M. A. Bopp, V. Deckert, P. Descouts, R. Eckert, H.-J. Güntherodt, C. Hafner, B. Hecht, H. Heinzelmann, T. Huser, M. Jobin, U. Keller, T. Lacoste, P. Lambelet, F. Marquis-Weible, O. Martin, A. J. Meixner, B. Nechay, L. Novotny, M. Pfeiffer, C. Philipona, T. Plakhotnik, A. Renn, A. Sayah, J.-M. Segura, B. Sick, U. Seigner, G. Tarrach, R. Vahldieck, U. P. Wilde, D. Zeisel, and R. Zenobi, *Chimia*, **51**, 760 (1997)
[95] G. T. Shubeita, S. K. Sekatskii, B. Reido, G. Dietler, and U. Dürig, *J. Appl. Phys.*, **88**, 2921 (2000)
[96] G. Tarrach, M. A. Bopp, D. Zeisel, and A. J. Meixner, *Rev. Sci. Instrum.*, **66**, 3569 (1995)
[97] K. Karrai and R. D. Grober, *Appl. Phys. Lett.*, **66**, 1842 (1995)
[98] R. D. Grober, J. Acimovic, J. Schuck, D. Hessman, P. J. Kindlemann, J. Hespanha, A. S. Morse, K. Karrai, I. Tiemann, and S. Manus, *Rev. Sci. Instrum.*, **71**, 2776 (2000)
[99] *Theory of Elasticity*, by L. D. Landau and E. M. Lifshitz, Pergamon Press, 3rd ed., 1986
[100] F. J. Giessibl, *Appl. Phys. Lett.*, **73**, 3956 (1998)
[101] J. E. Sader, *J. of Appl. Phys.*, **84**, 64 (1998)
[102] O. Marti and J. Colchero, *Physikalischen Blätter*, **12**, 1007 (1992)
[103] P. K. Wei, W. S. Fann, *J. Appl. Phys.*, **83**, 3461 (1998)
[104] *Design and Characteristics of a General Purpose Atomic Force Microscope*, P. LeBlanc, Master's Thesis, 1996
[105] J. Barenz, O. Hollricher, and O. Marti, *Rev. Sci. Instrum.*, **67**, 1912 (1996)
[106] J. Michealis, C. Hettich, J. Mlynek, and V. Sandoghdar, *Nature*, **405**, 325 (2000)
[107] U. C. Fischer, J. Koglin, and H. Fuchs, *J. Microscopy*, **176**, 231 (1994)
[108] D. Alliata, C. Cecconi, and C. Nicolini, *Rev. Sci. Instrum.*, **67**, 748 (1996)
[109] J. C. Hultenn, D. A. Treichel, M. T. Smith, M. L. Duval, T. R. Jensen and R. P. Van Duyne, *J. Phys. Chem. B*, **103**, 3854 (1999)
[110] F. Lenzmann, K. Li, A. H. Kitai, and H. D. H. Stöver, *Chem. Mater.*, **6**, 156 (1994)
[111] A. S. Dimitrov and K. Nagayama, *Langmuir*, **12**, 1303 (1996)
[112] A. S. Dimitrov and K. Nagayama, *Chem. Phys. Lett.*, **243**, 462 (1995)
[113] *Optical Signal Processing*, by A. VanderLught, Wiley-Interscience, 1993
[114] P. F. Barbara, D. M. Adams, and D. B. O'Connor, *Ann. Rev. Mater. Sci.*, **29**, 433 (1999)
[115] C. W. Hollars and R. C. Dunn, *J. Chem. Phys.*, **112**, 7822 (2000)
[116] *Styrene, its Polymers, Copolymers and Derivatives*, R. H. Boundy and R. F. Boyer (Eds.), Reinhold, 1952
[117] D. G. Gray, *La Physique au Canada*, March and April 1998, p.111
[118] *Application of Atomic Force Microscopy to Cellulose, Wood, Kraft Pulp Fibers and*

Paper, S. J. Hanley, Ph.D. thesis, 1995
[119] D. H. Page and P. A.Tydeman, *Nature*, **199**, 471 (1963)
[120] *Paper Structure and Properties*, J. Bristow and P. Kolseth (Eds.), Dekker, 1986
[121] S. J. Hanley and D. G. Gray, *J. Pulp Paper Sci.*, 25, 196 (1999)
[122] *Forbidden Light Scanning Near-Field Optical Microscopy*, B. Hecht, Ph.D. thesis, 1996
[123] R. Eckert, J. Moritz, H. Gersen, H. Heinzelmann, G. Schürmann, W. Noell, U. Staufer and N. F. de Rooij, *Appl. Phys. Lett.*, **77**, 3695 (2000) – the authors actually observed near-field transmission through a fully-coated aperture.
[124] J. R. Krenn, A. Dereux, J. C. Weeber, E. Bourillot, Y. Lacroute, J. P. Goudonnet, G. Schider, W. Gotschy, A. Leitner, F. R. Aussenegg, and C. Girard, *Phys. Rev. Lett.*, **82**, 2590 (1999)
[125] B. Dumay, N. Richard, T. David, E. Bourillot, F. Scheurer, E. Beaurepaire, A. Dereux and Y. Lacroute, *J. Appl. Phys.*, **89**, 1138 (2001)
[126] Richter, M. Sueptitz, Ch. Lienau, T. Elsaesser, M. Ramsteiner, R. Noetzel, and K. H. Ploog, *Surface and Interface Analysis*, **25**, 583 (1997)
[127] H. Ghaemi, C. Cates, and B. B. Goldberg, *Ultramicroscopy*, **57**, 165 (1995)
[128] J. Kerimo, D. M. Adams, P. F. Barbara, D. M. Kaschak, and T. E. Mallouk, *J. Phys. Chem. B*, **102**, 9451 (1998)
[129] D. Tsai and Y. Lu, *Appl. Phys. Lett.*, **73**, 2724 (1998)
[130] U. Dürig, H. R. Steinauer, N. Blanc, *J. Appl. Phys.*, **82**, 3641 (1997)
[131] W. A. Atia, and C. C. Davis, *Appl. Phys. Lett.*, **70**, 405 (1997)
[132] R. L. Williamson and M. J. Miles, *J. Vac. Sci. Technol. B*, **14**, 809 (1996)
[133] D. G. Gray, personal communication